University of Namur

DOCTOR OF SCIENCES

Experimental and theoretical study of a magnetron DC-PECVD acetylene discharge

Fauroux, Antoine

Award date:
2021

Awarding institution:
University of Namur

Link to publication

UNIVERSITÉ
DE NAMUR

Faculté des Sciences

Experimental and theoretical study of a magnetron DC-PECVD acetylene discharge

Rédaction présentée en vue de l'obtention du grade de docteur en Sciences

Antoine Fauroux
Namur, 2021

Acknowledgements

First and foremost, I would like to express my gratitude to Prof. Stephane Lucas for his guidance and for pushing me to better myself. I would also like to thank the members of my jury: Dr. Stefan Grosse, Prof. Erik Neyts, Prof. Yoann Olivier, and Dr. Andreas Pflug, who accepted to evaluate my work, and who gave me valuable insights from their respective domains of expertise. I would like to acknowledge here the importance for this work of the collaboration with Fraunhofer IST and Dr. Andreas Pflug, who provided the PIC-MC software and his precious help to understand and debug my simulations.

I would like to thank my colleagues from the university of Namur, they were always very friendly and willing to help me, and without them I could never have finished this PhD. I felt at home in Belgium for these 5 years, and I will look back with nostalgia to my life here. In particular, I would like to thank Martin for being always there for me throughout all the adventures and for his joyful attitude, Romain and Stella for their help with simulations and their friendship, Pavel and Jérôme for their fruitful collaboration and kindliness, Remy, Tijani and Julien for their help with experiments, Alexia for her considerate help with my disorganization, and all the others from the LARN and beyond.

I also need to mention my loving Madzia without whom my life, and for sure my thesis, would not be complete. I could never have reached this achievement without the constant support and affection of my family and friends and for that I would like to thank them.

Abstract

The deposition of DLC films from a low-pressure acetylene gas mixture in magnetron reactors has continuously driven the interest of scientists for decades. It is used widely by industrials in large batch coaters to produce high added value protective coatings, or by experimentalists to develop processes that include amorphous hydrogenated carbon as a key component in novel and exciting applications for e.g. in electronics, energy storage, or even medicine. It is still only possible to resolve analytically the complex equations of the dynamics of cold temperature reactive plasmas for very simple cases, and gaining insight on the reactions and particle behaviour usually requires the use of numerical simulations. For very low-pressure discharges (below 1 Pa), the individual particle trajectory must be resolved, which implies the use of statistical Monte-Carlo approaches like PIC-MC. The high computational cost of such simulation limits the attainable powers, the simulation size and length, and the number of considered species. The object of the present study is therefore to find out if a realistic PIC-MC simulation of a PECVD discharge in the case of the deposition of DLC from acetylene can be developed, and to see if it is possible to compare simulations' results in a constraining way with experiments.

We showed, that it is indeed possible to simulate this type of acetylenic discharge with a simple but self-coherent plasma chemistry model in a small 3D simulation box. With simulation times of up to 1.2 ms, an equilibrium could be attained for the densities and fluxes of all species. Even if ions are the main species created within the plasma, radicals accumulated to densities comparable to that of ions due to their slower diffusion speed. Differences in concentrations were observed across the simulation chamber between the thermally diffusing neutrals and the accelerated ions. Moreover, some species were created within the chamber from the reaction between species generated in the plasma bulk interacting with the background acetylene.

Those predictions were tested against mass spectrometric measurements in experiments with various acetylene ratios and discharge powers. The variations of species flux towards the substrate, with ratio were similar in both experiments and simulations. It was possible to match the linear evolution of the ions' flux with power between experiments and simulations. Moreover, the simulations showed a correlation between the electron density and all plasma products ones. This suggests that the power scaling of simulation's predictions should be possible until the point where the reactive species concentrations would become non-neglectable compared to the acetylene one.

Since the concentrations and fluxes varied throughout the chamber in this configuration, variation of the film characteristics and of the deposition rate were expected across the substrate. To test the simulations film deposition predictions, a dynamic surface chemistry model was set-up. It includes the creation of dangling bonds via the chemical sputtering due to the joint ion bombardment and hydrogen flux and the preferential deposition of radicals on dangling bonds. Since the equilibrium of the dangling bonds coverage was not obtained extrapolating the absorption of radicals was necessary. Despite this and the power extrapolation, simulations were able to give quantitatively accurate deposition rates and deposition profiles when compared to experiments. However, the hydrogen stoichiometry was higher in the simulations than the one measured with ERDA measurements. In order to improve the film deposition prediction several refining of the surface model would have to be included in future works. Some perspectives are given regarding the possible improvements of the current model, which could already be used for more complex configurations to reduce the need for the costly trial-and-error search for optimal deposition parameters.

Keywords

C_2H_2, a-CH, DLC,

Résumé

Le dépôt de films de carbone amorphe hydrogéné à partir de réacteurs magnétrons et d'un mélange d'acétylène et d'argon à basse pression intéresse les scientifiques et les industriels depuis des décennies. Ce type de film mince de carbone (DLC) possède un pourcentage important de liaisons tétraédrique analogue au diamant et est fréquemment utilisé par les industrielles comme film protecteur dans des applications mécaniques et tribologiques, ou utilisé également par les scientifiques qui incluent ce type de pulvérisation cathodique magnétron avec de l'acétylène dans des films plus complexes avec par exemple plusieurs couches ou un dopage métallique pour des applications novatrices en électronique, énergétique, ou même en médecine. Malgré nos connaissances étendues sur les plasmas froids, la complexité des équations de la dynamique d'un tel système constitué d'un nombre important de particules en quasi-équilibre, rend toujours difficile et peu fructueuse l'approche analytique, alors que les mesures in-situ donnent des informations indirectes et incomplètes. C'est pourquoi la simulation numérique est un outil indispensable à la compréhension de tel processus, et à très basse pression (au-dessous de 1 Pa), seul les modèles de type Monte-Carlo (DSMC ou PIC-MC), peuvent rendre compte des mouvement précis des molécules, ions et électrons qui constituent le plasma. Ces simulations ont un coût important en ressource numérique, requièrent l'usage de supercalculateurs, et sont limitées en puissance, nombre d'espèces et taille des simulations. Le but de cette étude est donc de déterminer si des simulations PIC-MC réalistes d'une décharge PECVD dans le cas du dépôt de films DLC avec un gaz réactif comme l'acétylène peuvent être réalisées et comparées de manière contraignante avec l'expérience.

Nous avons montré qu'il était en effet possible de simuler ce type de décharge avec un modèle simple mais complet de la chimie du plasma dans une chambre magnétron en 3D de petites dimensions de manière optimisée. Avec des temps de simulations avoisinant la milliseconde nous avons atteint l'équilibre pour toutes les espèces introduites, y compris les espèces neutres et réactives (ou radicaux). Même si les ions sont les espèces les plus importantes, les radicaux se sont accumulés dans la chambre à des densités comparables du fait de leur diffusion lente. De plus des espèces de second degrés, issues des réactions entre les réactifs produit dans le plasma et l'acétylène ont été incluse et nous avons montré qu'elles jouaient un rôle important.
Ces prédictions ont été comparées avec des mesures par spectromètre de masse pour des expériences avec divers ratios d'acétylène et d'argon et différentes puissances. Nous avons montré que l'évolution du flux d'espèces au niveau du substrat en fonction du ratio d'acétylène était similaire dans les simulations et les expériences. Il a même été possible de faire correspondre les pentes de l'évolution du flux des ions entre les simulations et l'expérience en fonction de la puissance de décharge, ce qui veux dire que nos résultats devraient pouvoir être extrapolés à plus haute puissance. Cette évolution linéaire provient du fait que la puissance est proportionnelle à la densité électronique, que l'énergie des électrons demeure constante, et que les collisions principales qui gouverne la PCR sont les collisions entre les électrons et l'acétylène injecté dans la chambre en flux constant. Cela signifie que les résultats de nos simulations sont extrapolables à plus haute énergie au moins tant que la densité des réactifs demeure négligeable comparer à celle de l'acétylène.
Puisque les concentrations en espèces réactives variaient en fonction de la position dans la chambre, des variations des conditions du dépôts et donc les propriétés des films déposés à différent endroit devais différer. C'est pourquoi de nouvelles simulations ont été effectuées avec un modèle de la déposition de carbone amorphe incluant la création et la désorption de liaisons hydrogène influant sur les propriétés de déposition des radicaux. Malgré des temps de simulations approchant la millisecondes il n'a pas été possible

d'atteindre l'équilibre de la couverture en hydrogène, ce qui a nécessité une extrapolation de la contribution au dépôt de certaines espèces, et malgré la nécessaire extrapolation en puissance, nous avons montré que les prédictions de vitesse de déposition en fonction du ratio d'acétylène et en fonction de la position du substrat était quantitativement comparable avec les résultats expérimentaux. Le modèle du dépôt présenté nécessiterait des améliorations puisque la stœchiométrie en hydrogène des films simulés et ceux mesurer par ERDA différait de manière irréconciliable même en considérant les erreurs possibles introduite par l'incertitude concernant les probabilités des réactions de surface. Des perspectives d'amélioration du modèle sont présentées, mais nous avons montré que d'ores et déjà ces simulations sont capables de prédire quantitativement les concentrations en réactifs partout dans la chambre et les vitesses de déposition. Ces simulations PIC-MC sont à notre connaissance les premières à inclurent autant d'espèces dans un modèles 3D cohérent allant de l'injection du gaz jusqu'au dépôt de films.

Table of Contents

List of Figures

List of Tables

List of Abbreviations

DLC – Diamond Like Carbon
a-C – amorphous carbon
a-CH – amorphous hydrogenated carbon
ta-CH – tetrahedral amorphous hydrogenated carbon

DSMC – Direct Simulation Monte-Carlo
PIC-MC – Particle-In-Cell Monte-Carlo
PVD – Pulsed Vapor Deposition
CVD – Chemical Vapor Deposition
PECVD – Plasma Enhanced Deposition
EEDF – Electron Energy Distribution Function
IEDF – Ion Energy Distribution Function
NTC – No Time Counter method

XPS – X -Ray Photoelectron Spectroscopy
IBA – Ion Beam Analysis
RBS – Rutherford backscattering spectrometry
OES – Optical Emission Spectroscopy
QCM – Quartz Crystal Microbalance
MS – Mass Spectrometer
SIMS – Secondary-ion mass spectrometry
RGA – Residual Gas Analysis

PIII – Pulsed Ion Impact Implantation
CCP – Capacitively Coupled Plasma
ICP – Inductively Coupled Plasma
MW – Microwave
ETP – Expanding Thermal Arc
HIPIMS – High-power impulse magnetron sputtering
MS – Magnetron sputtering (or Mass Spectrometer)
DCMS – DC Magnetron sputtering

PCR – Plasma Chemical Reactions
CS – Cross Section
EII – Electron Impact Ionization
DI – Dissociative Ionization
EE – Electronic Excitation
EID – Electronic Impact Dissociation

DE – Dissociative Excitation
DEA – Dissociative Electron Attachment
DR – Dissociative Recombination
SEEY – Secondary Emitted Electron Yield (or SEE, or SEY)
Nreal – statistical weight factor of superparticles in a PIC-MC simulation

LARN – Laboratoire d'Analyse par Réaction Nucléaire
NISM – Namur Institute of Structured Matter
UMIST – University of Manchester Institute of Science and Technology
NIST – National Institute of Standards and Technology
PLASMANT – Plasma Lab for Applications in Sustainability and Medicine of Antwerp
SRIM – Stopping and Range of Ions in Matter

List of Equations

Introduction

Thin film deposition from plasma sources already has omnipresent applications from electronics, to engineering or even medicine; it is a constantly improving field with ever-increasing number of available technics and applications. The physics behind near-vacuum plasma discharges involves charged and reactive species, carrying relatively important energies and interacting with surfaces and electromagnetic field. Even though, taken individually, particles and fields behave in a predictable manner, the transition from microscopic rules to macroscopic dynamics, expressed with the Boltzmann equation [1], is a particularly difficult mathematical problem. Meanwhile, the ongoing numerical revolution and the exponentially increasing computational power available to scientists allow the direct simulation of such complex systems.

When a plasma discharge is simple enough, like the linear Direct Current (DC) discharge at low pressure or the Townsend discharge, analytical models can be setup. However, if the chemistry or the electromagnetic excitation becomes more complex, numerical modelling prevails. When the gas pressure is high enough, some approximations to the Boltzmann equation and the particle transport can be made. The resulting fluid or hybrid numerical models are fast and can include many reactions and species [2]. However, for the magnetron sputtering deposition technique, which operates at an even lower pressure, studying the plasma phase requires considering individual particles trajectories in kinetic models like Direct Simulation Monte-Carlo (DSMC) or Particle-In-Cell Monte-Carlo (PIC-MC). These models rely on using a great number of simulated particles to obtain statistically significant results, hence they are by nature computationally costly.

Magnetron sputtering belongs to the Plasma Vapor Deposition techniques (PVD) and usually involves noble gases or simple reactive gases like N_2 or O_3 to produce either metallic or inorganic thin films. However, when used in conjunction with more complex gaseous precursors (referred as Plasma Enhanced Vapor Deposition (PECVD)), the increased number of species and possible interactions create a new challenge for simulation. Additionally, since some species are very reactive and short-lived, and the deposited films usually have very complex structures, in-situ diagnostics and film characterizations will only give partial information on the physical processes involved.

Diamond Like Carbon (DLC) is a type of thin film containing tetrahedrally bonded carbons and possibly hydrogen. Like natural diamond, this material has many one-of-a-kind properties that make it an interesting high-added-value coating for micro-electronics, automotive, medical, or engineering applications. Even though these types of coatings have been known and deposited via plasma methods since 1953 [3], the deposition techniques and their applications are in constant evolution and growth. Magnetron sputtering with a reactive hydrocarbon precursor gas like acetylene is a popular method of deposition for industrial applications because it is easily scalable and very modular. For example, even though this method does not produce the strongest films or have the fastest deposition rates, it can be enhanced via the use of multiple cathodes, complex magnetic field arrangements, substrate bias, multi-layered or doped films. Currently, the only available method to design or improve the reactive magnetron sputtering deposition of a DLC film onto any object relies on costly experimental trial-and-error. Commonly faced problems include creation of a reliably smooth, dense, and hard film on objects of any composition and shape while avoiding delamination, stress and inhomogeneities, as well as transposition and scale-up of the processes from laboratory reactors to industrial batch coaters. To help in this endeavour, numerical tools must be developed so that they are able to predict the characteristics of produced films directly from the plasma parameters (e.g. pressure, fluxes, discharge power, magnetic field arrangement).

The aim of this thesis is to develop a PIC-MC model of the PECVD of DLC thin films from reactive magnetron sputtering, and to validate it experimentally. For this purpose, a research plasma deposition chamber was used and represented numerically by a simplified 3D-meshed model. The species and reactions included were chosen carefully based on the double constraint of having a self-coherent view of the plasma chemical reactions (PCR) while remaining computable. An optimized PIC-MC simulation code was used to run simulations on a high-power computing (HPC) cluster. Comparing PIC-MC simulations with experiments is a complicated task for several reasons. The powers attainable in such simulations are in the order of 1W, whereas it can go up to thousand watts for experimental discharges. Additionally, attainable simulation time are in the order of the hundreds μs, but experimental results are acquired on much longer time scales. Hence, several methods had to be developed to be able to compare simulations with experiments in a constraining way.

This thesis puts emphasis on modelling the plasma phase and the deposition process in a simple case with DC power, an unbalanced magnetic configuration with a grounded planar substrate facing the cathode with a graphite target. While, as explained earlier, many configurations are possible for this method of deposition, it is difficult to constrain PIC-MC plasma deposition model from direct comparison with experiments, thus the general approach of this study is to reduce the number of input parameters and vary each of them individually. The main parameters of interest were the discharge power and the acetylene ratio since they seemed to affect the discharge the most; but the effect of other parameters on the discharge, e.g. the substrate bias, the initial pressure, or the distance between the substrate and the cathode, were also studied.

In Chapter 1 some brief introduction to plasma physics, DLCs, and an overview of the different deposition techniques for DLC films, will form the theoretical background on which the thesis will rely. For a more complete introduction to the plasma physics domain and its application to depositing DLC, references to major reviews and books will be given. In Chapter 2, a literature review will discuss the main concepts introduced above in more details. This review includes an overview of the PCR and their relative importance for reactive magnetron sputtering in acetylene discharges. This discussion drives the decisions regarding the parametrization of the PIC-MC simulation model. The creation of the model, the geometry, magnetic field configuration, and other important parametrization aspects are described in Chapter 3. This chapter also describes experimental methods for studying the plasma phase, or in-situ measurements, as well as the film characterization techniques. The main results of this study are divided in two parts: Chapter 4 presents all the simulation and experimental results on the plasma phase, while Chapter 5 presents the results regarding the predicted film deposition compared to results from film characterization. Both chapters are presented around peer-reviewed articles along with some complements. Chapter 6 describes general conclusions, and introduces some perspectives for continuation of this work.

Chapter 1 *Theoretical background*

Some fundamentals of plasma physics are given as a preliminary for understanding the different methods of plasma deposition of diamond like carbon films. For more complete theoretical description of plasmas, the reader could refer to [4–6]*, and for more complete reviews of the DLC deposition methods to* [3,7–10].

1.1 Fundamentals of plasma physics

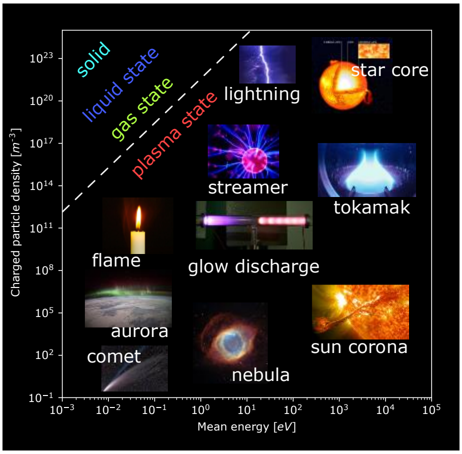

Figure 1.1 Plasma in nature sorted by mean energy and charged particles density[1]

Plasma is the fourth state of matter and constitute 95% of the visible matter in the universe [11]. When energy is added to mater in the form

---

[1] *Original artwork made by the author from individual pictures taken from Wikimedia Commons and licensed under the Creative Commons Attribution-Share Alike 3.0 Unported license.*

of heat, it turns solid into liquid, then into gas, and finally into plasma, when gas particles have enough energy for collisions to strip electrons. On Earth plasmas are naturally present as flames, lightnings, polar aurorae, ionosphere, magnetosphere, and cosmic rays. In space, the most recognizable source of plasma is stars, which are dense and warm plasmas heated by fusion energy. But plasmas are also present in stellar winds, comets, interstellar medium, pulsars, active galactic nucleus jets, or accretion disks around dense objects like neutron stars or black holes [11]. When weighing the mass contributions of galaxy clusters, 5/6 of the mass is identified as dark matter, the remaining 1/6 is primarily in the form of hot (~ 2 – 10 keV) diffuse intracluster plasma, and all the galaxies, stars and planets only account less than a percent of the total mass[12].

In general, plasmas are constituted of equal densities of positively and negatively charged particles (quasi-neutrality), and can conduct electricity, sometimes even better than metals. The crucial parameters defining the plasma behaviour are the proportion of charged particles (“ionization degree”) and the mean energy of charged species. When most of the gas is ionized or when the kinetic energy is high, plasmas can reach thermal equilibrium, which means that the temperature of all species, charged and neutral, is the same. In a gas or a plasma, when a group of particles is in thermal equilibrium, their kinetic energy can be described by the single macroscopic parameter called temperature, and the probability density function that a particle has a velocity contained in the infinitesimal three-dimensional velocity volume $\mathrm{d}^3 v$ centred in v, follows the Maxwell-Boltzmann distribution:

$$f(v)\mathrm{d}^3 v = \left(\frac{m}{2\pi k_b T}\right)^{\frac{3}{2}} e^{-\frac{\frac{1}{2}mv^2}{k_b T}} \mathrm{d}^3 v, \qquad \text{(Eq. 1.1)}$$

with m the mass, v the velocity, k_b the Boltzmann constant, and T the temperature.

However, at low pressure, it is possible to accelerate charged particles with an electric field, and thus have different energy distributions for different particle types. For example, if a voltage is applied between two metallic plates in a low-pressure gas, then some pre-occurring free electrons (created mostly from cosmic radiation) might get accelerated enough to cause the ionization of the gas, creating more free-electrons. If the ionization rate is high enough, the electrons will trigger a cascade reaction or “Townsend cascade”, and an electric current will pass through the gas.

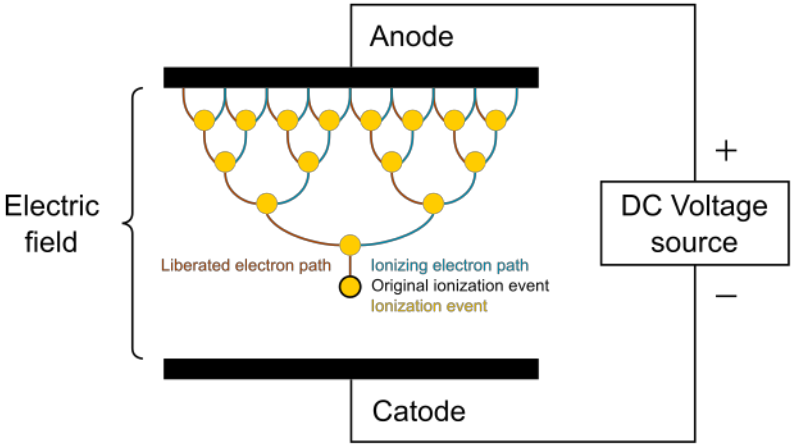

Figure 1.2 Schematic representation of Townsend discharge or Townsend avalanche. The accelerated free electrons collide with the gas particles and ionize some of them, creating an increasing number of free electrons.[1]

For a given gas, pressure and distance between the plates, the breakdown voltage will be given according to Paschen’s Law [6]. There exists an optimal distance at which the breakdown voltage will be minimum. Following the ignition of the plasma, the current can be increased, injecting more energies into the gas via electron collisions and creating more ions and excited particles. Electronically excited atoms can release their energy via photo-emission, thus giving off a characteristic glow which depends on the electronic orbital configuration of the gas species in use (the “glow discharge” regime of Figure 1.3).

Such a regime defines what is called “cold plasma” as the temperature of both the gas and the ions remain low compared to the temperature of the electron that carries most of the energy. When the electric field and the current get stronger, more kinetic energy is transferred to the gas and the discharge enters the “abnormal glow regime”. When the electric field becomes even stronger, an electric arc is formed and the temperature of the gas surrounding the discharge increases dramatically.

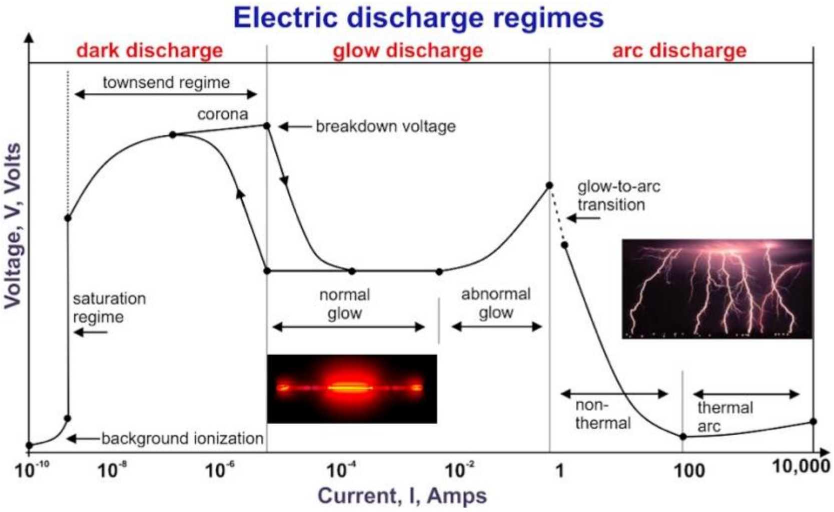

Figure 1.3. The typical I-V characteristic (voltage vs. current) of a linear plasma discharge between two planar electrodes, showing the different discharge regimes[2]

Due to the electron's higher mobility, positively charged ions are quickly surrounded by a shield of electrons in such a way that seen from a distance, the quasi-neutrality is respected. This shield's radius is called the Debye length and depends on the electronic density and the electron's temperature in the following way:

$$\lambda_D = \left(\frac{\epsilon_0 k_b T_e}{n_\mathrm{e} e^2}\right)^{1/2} \qquad \text{(Eq. 1.2)}$$

with ϵ_0 the permittivity of free space, T_e the electronic temperature, n_e the electronic density, and e the charge of an electron. If the studied plasma has a Debye length that is neglectable compared to a characteristic length of the discharge[3], then the plasma is called "ideal" and a fluid description is possible [6].

Similarly, a sheath of cations is created near surfaces depending on their electrical potential. Often, when generating cold plasmas in a vacuum chamber, only an electrode with negative potential is used and the

---

[2] *Taken from Wikimedia Commons and licensed under the Creative Commons Attribution-Share Alike 3.0 Unported license.*

[3] *The mean free path of particles could be used as a characteristic length. Alternatively, the number of charged particles in a sphere with a radius of one Debye length is used to characterize the « ideality » of a plasma, i.e. the propension of it to follow the quasi-neutrality and allow particle diffusion resembling that of a gas* [6].

chamber is grounded[4]. In this case, positively charged sheath is made of cations is created in front of the cathode to mask its negative charge. Additionally, presheath layer forms, with a potential drop which accelerate the ions enough to cross the positive sheath. This gives a condition on the minimum speed needed for ions to enter the sheath called the Bohm sheath criterion, which is related to the value of the potential drop from the plasma potential to the potential at the edge of the sheath [6]. The potential drop in the presheath is called the floating potential, and it is the potential that conducting surfaces will take if they are embedded in the plasma phase, with no connection to the ground or to a generator.

---

[4] *There is sometimes confusion on whether the negatively charged electrode is called "the cathode" or "the anode", the convention is that "the cathode" is the electrode that can give electrons to the medium and can attract positively charged ions like for an electric battery.*

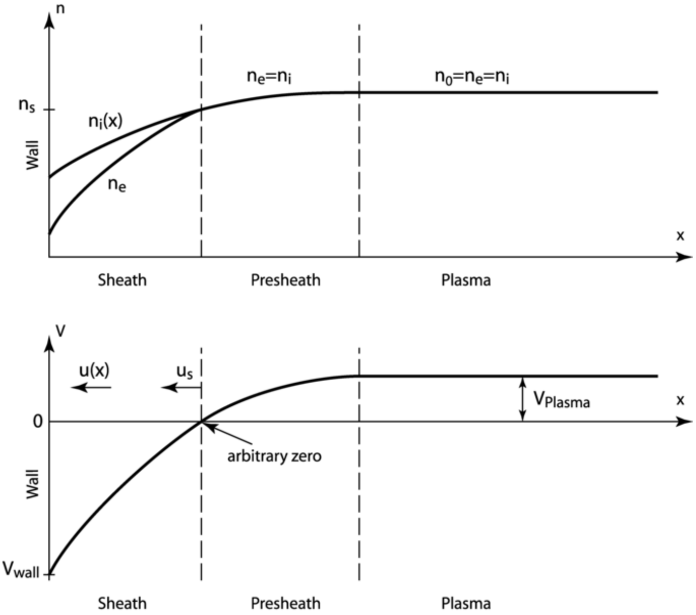

Figure 1.4 Plasma sheath and presheath near a negatively charged cathode. Density of electrons and ions (top), and electric potential (bottom).[5]

The impinging of ions onto the cathode leads to the sputtering of material via a collision cascade, which can direct the kinetic energy of the ions backward (see Figure 1.5). The ion recombination during impinging on the surface can also generate secondary emission of electrons, which are an important source of new electrons in magnetron discharges. The amount of material that is sputtered depends primarily on the nature of the ion, its energy, and the material of the cathode (or target). For most materials and ions, this sputtering yield can be either

---

[5] *Taken from Wikimedia Commons and licensed under the Creative Commons Attribution-Share Alike 3.0 Unported license.*

measured or predicted by the Stopping and Range of Ions in Matter (SRIM) simulations [13]. According to the Bragg's rule, in case of compound targets it is also possible to simply obtain the sputtering characteristics of a material by linearly adding the contributions for each atomic species composing the target's material. However, some corrections might have to be taken into account depending on the atomic bounding (double, triple bonds) [13]. More details on the simulation of the sputtering used in this study will be given in the complement section of Chapter 5.

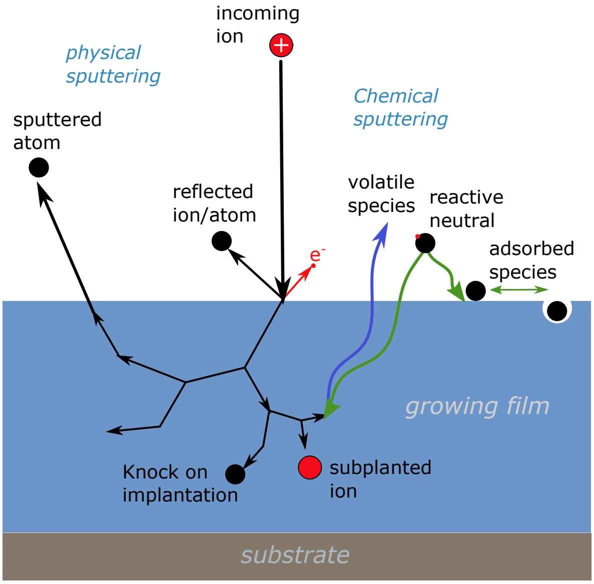

Figure 1.5 Schematic illustration of the sputtering due to the impinging of a surface by energetic ions: The incoming ions are either reflected or subplanted, then a collision cascade can cause the ejection of one or more atoms from the target's surface, and secondary electrons might be emitted. This scheme also shows potential interactions of neutral species inducing chemical sputtering by diffusing inside the material's surface, creating volatile species by bonding to weakly bonded atoms, and the adsorption-diffusion of neutral species on the film's surface.

Sputtering induced by ion bombardment is useful for many applications; for example, microelectronics relies on the plasma etching of masked silicon plates to create millions of transistors composing our modern CPUs. In the case of reactive magnetron sputtering (RMS) reactive species are also generated in the plasma and condense onto the target and the substrate. The concentration of plasma due to the magnetic confinement leads to a concentration of the damage to the target over a "racetrack" which could become problematic after long use of the cathode, and is the object of countering techniques like the use of cylindrical cathode or moving magnetic field [14]. The sputtering of material from surface subject to energetic ion impinging can be enhanced in the presence of reactive neutrals that can diffuse through the material, like atomic hydrogen [15], and bound with displaced atoms. This is called chemical sputtering; it is important in the case of the reactive magnetron deposition of a-CH, as explained in more detail in Section 1.3 and Chapter 5.

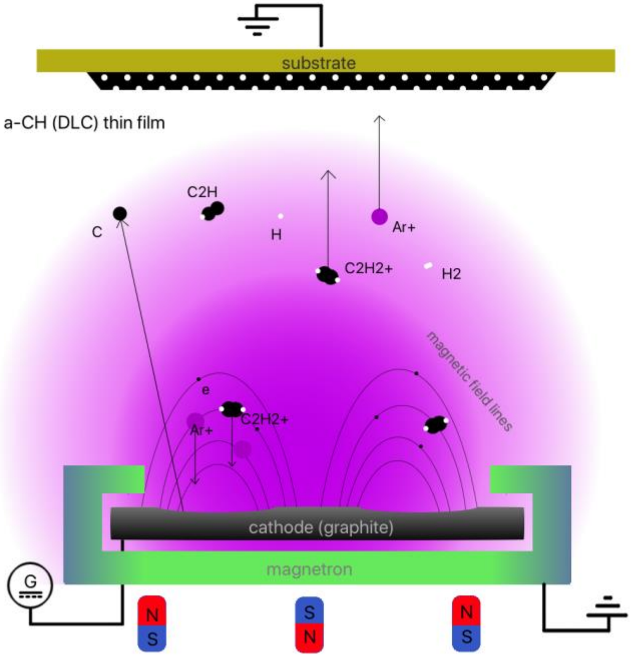

Figure 1.6 Scheme of the reactive magnetron sputtering deposition of amorphous hydrogenated carbon (a-CH) from a DC powered cathode with a graphite target in a low-pressure acetylene/argon gas mixture.

Apart from ionizations, other types of non-elastic electron collisions can transfer energy to the gas. Often a noble gas is used to ignite cold plasma because of its stability. In this case, only electronic excitation is possible, with sometimes metastable states like for argon [16]. However, when a molecular gas is used or added in the chamber, vibrational or rotational excitation modes are available. Furthermore, electron collisions can lead directly or after passing by excited states to the dissociation of molecules. This leads to the creation of very reactive species that might not be easily created otherwise with standard chemistry reactions. Those reactive species are interesting for film deposition, but also for polymer or nanoparticle creation [5]. In Chapter 2, an overview of the plasma chemical reactions (PCR) that are relevant for the PECVD of a-CH with reactive magnetron sputtering will be presented.

1.2 Diamond Like Carbon

Carbon is one of the most abundant elements on Earth, it is the backbone on which organic molecules and biology is built. Being the 6th element of the periodic table, carbon has the electronic configuration: $1s^22s^22p^2$, which makes it tetravalent. It can be found in pure form in nature as diamond or graphite. Graphite is the most stable crystalline form of carbon under standard conditions and apart for its known use in pencils, it is a good electrical and thermal conductor widely used in electronic products like electrodes, circuits, or batteries. It is composed of many hexagonally-arranged single-atom layers, stacked in an AB sequence and linked by a weak Van der Walls interaction produced by a delocalized π-orbital [17]. In the recent decades, material science discovered various ways to produce single-sheet graphite, or graphene, which has outstanding physical properties [18]. It can be either produced from top-down approaches by separating sheets of graphite, or in a bottom-up approaches like Chemical Vapor Deposition (CVD) [18], and it has already many high-end applications like touch screens, LCD, or solar panels. Diamond, on the other hand, has a face-centred cubic crystallographic structure in which each carbon is bonded to 4 others in a tetrahedral arrangement. This dense packing and the strength of the tetrahedral σ-bonds make diamond the natural material with the highest hardness and thermal conductivity, and is used in many industrial applications, e.g. in cutting or polishing tools. Nowadays, synthetic diamonds can be grown with CVD techniques at high pressure and temperature, so industrials and scientists are not solely reliant on the mining prospects of natural diamond.

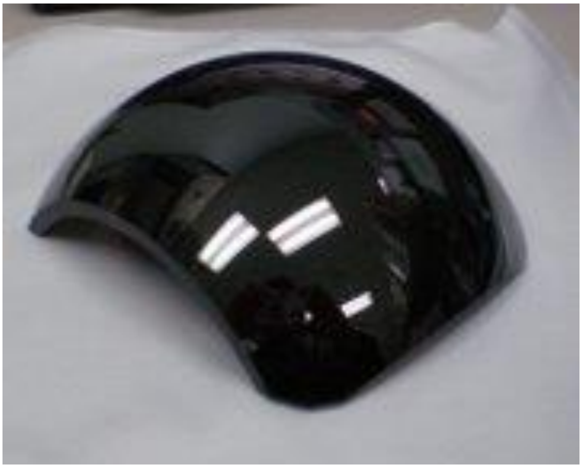

Figure 1.7 Dome coated with DLC for optical and tribological purposes.[6]

Diamond like carbon (or DLC) is an amorphous and metastable material analogous to synthetic diamond but without grain boundaries

---

[6] *Taken from Wikimedia Commons and licensed under the Creative Commons Attribution-Share Alike 3.0 Unported license.*

and cheaper to produce. It contains various amounts of tetrahedral (sp^3) and graphite-like (sp^2) carbon bonds and various amount of hydrogen. Due to its interesting properties, DLC is widely used as a protective coating by the industry. DLCs have a high mechanical hardness and low dry-wear resistance, and they enhance lubricant adhesion due to the surface hydrogen [19]. This makes these types of coatings a good interfacial layer for mechanical and engineering applications (e.g. in the automotive industry, or for cutting tools). Additionally, due to their density and chemical inertness, they serve as a strong corrosion and diffusion barrier (e.g. for hard disk drive). In thin layer, they can be made optically transparent, which is interesting for applications involving protecting coatings on car windows, smartphone screens or other see-through media. DLCs can be highly smooth, and are hydrophobic – a feature desirable for creating micro-electro-mechanical systems (MEMs). Finally, they are also wide band-gap semiconductors, and they are bio-compatible with potential applications in medicine (e.g. in orthopaedic prosthetics, in biology as a biosensor layer [20]).

A common problem faced during DLC deposition is delamination (when the surface of a film is peeling off), or most generally a problem of attachment and stability of the film [3,21–23]. The reasons of this could be that the carbon atoms bonds preferably between themselves and not with the substrate atoms, or that the impinging of ions on the growing film is building up stress in the layer which causes the film density to rise which is beneficial for hardness but when this stress becomes too important or when the film becomes too thick then it can no longer maintain its coherence and it delaminates. To avoid this problem several techniques are used by experimentalists like: (i) keeping the sample's surface well cleaned (with e.g. ultrasound bath, alcohol cleaning, etching) [24], (ii) depositing an interfacial layer before the DLC [23,25–28], (iii) or minimising the stress by for example metal doping or heat treatments [21,22,29,30]. In general, these techniques and the resulting complex procedures to deposit state-of-the-art DLC are the fruit of many trial and error experiments, and could benefit greatly from a better understanding of the C_2H_2 plasma chemistry at low pressure.

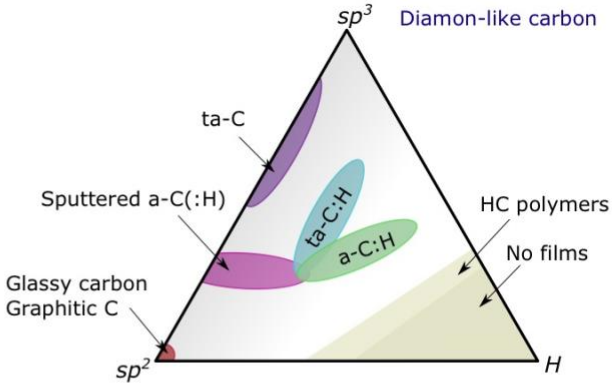

Figure 1.8 Ternary phase diagram of bonding in amorphous carbon-hydrogen alloys.

Depending on the deposition technique used, various types of DLCs can be produced. They can be conveniently sorted according to their sp^2/sp^3 ratio and H content in a ternary diagram, as first presented by Jacob and Möller [31] (see Figure 1.8). These two parameters are the most significant ones regarding the resulting film characteristics mentioned above. The films containing more sp^3 and less hydrogen are the hardest and densest, and are thus preferable for many applications; however, some constraints might favour the faster PECVD techniques involving the usage of hydrocarbon precursors, and thus implying the incorporation of hydrogen atoms within the deposited films.

Table 1 Comparison of major properties of amorphous carbons with those of reference materials: diamond, graphite, C60 and polyethylene (taken from [19]*).*

Material	sp3 (%)	H (%)	Density (g.cm-3)	Gap (eV)	Hardness (Gpa)
Diamond	100	0	3.515	5.5	100
Graphite	0	0	2.267	0	0.3
ta-C	80	0	3.1	2.5	80
a-C:H hard	40	30-40	1.6-2.2	1.1-1.7	10-20
a-C:H soft	60	40-50	1.2-1.6	1.7-4	<10
ta-C:H	70	30	2.4	2.0-2.5	50
Polyethylene	100	67	0.92	6	0.01

1.3 Methods of deposition

❖ Ion beam

Ion beam techniques were the first capable of producing DLC films. They usually consist of an ion source, e.g. carbon sputtered from a graphite electrode or an ionized hydrocarbon gas, and grid electrodes that accelerate those ions, sometimes with a magnetic field acting as a guide. The best results are obtained when the amount of residual neutrals is low and the mean energy per carbon atom is around 100 eV [8]. The creation of sp^3 bonds is due to the densification of the film below its surface resulting from ion subplantation. It is possible to filter ions based on their masses and thus have a controlled ion beam with only one type of ion, which is very useful for the study of plasma-surface interaction. However, the deposition rate of this technique is usually very low.

❖ Thermalized plasma

Cathodic arc and Expanding thermal plasma (ETP) are two DLC deposition methods that rely on the usage of thermalized plasma arcs for either sputtering a graphite cathode at high rates, or ionizing a non-reactive gas that will interact with a hydrocarbon gaseous precursor [19,32]. The particles created in ETP are then drawn by the pressure difference into a vacuum chamber towards a substrate in a supersonic jet. Cathodic arcs can include filtering of the species and are suitable for depositing films onto isolating substrates, but often present instabilities. This technique allows the usage of high power and high ionization degree thermal plasmas without damaging sensitive substrates by delocalizing the particle source and the substrate. They are reliable methods of DLC deposition; however, they do not produce the hardest films or have the fastest deposition rates. As with cathodic arcs, the Pulsed Laser Deposition technique rely on creating highly ionized plasma away from the substrate by using very short and intense laser pulse to vaporize materials.

❖ PECVD

Plasma Enhanced Vapor Deposition (PECVD) is a commonly used method to deposit DLC. It relies on creating a plasma (e.g. with radio frequency (RF) or micro wave (MW) discharges) within a gas mixture containing a hydrocarbon precursor (e.g. C_2H_2 or CH_4). The dissociative collisions between energetic electrons and the background gas create new reactive species, which then recombine into heavier species or condense onto the substrate. This process is usually fast, but the film often contains large amount of hydrogen and is weaker than the films produced via other methods. The two gaseous monomers most commonly used for DLCs deposition are C_2H_2 and CH_4. To enhance the deposition, the charged species can be energized via the use of inductive (ICP) or capacitive (CCP) coupling between the power source and the plasma. Some grid electrodes or some magnetic field arrangements can be further used to accelerate ions toward the substrate. One problem faced when doing PECVD of DLC is that the hydrocarbon chemistry can easily create dust particles or soot via fast polymerization reactions. Hence, it is usually preferable to work at the lowest possible pressure.

❖ Magnetron Sputtering

Sputtering or Physical Vapor Deposition (PVD) is one of the most common DLC deposition method. It uses either DC or RF excitation to ionize a noble gas at low pressure and pulverize carbon from a graphite cathode onto a substrate. Several techniques are commonly used to improve this method of deposition and circumvent the low sputtering yield of graphite. Magnetron Sputtering (MS) is a commonly used practice that relies on using permanent magnets behind the cathode to confine electrons and reach a higher ionization degree. By using an unbalanced magnetic field, it is possible to have magnetic field lines pass through the substrate and to direct a high ions flux towards the growing film. To increase the energy of the ions bombarding the film, as well as the film's density and hardness, a negative voltage bias is often applied to the substrate. With Reactive Magnetron Sputtering (RMS), a reactive gas is used to either react with the target and substrate (e.g. the RMS deposition of TiO_2 [33]), or to enhance the deposition via the creation of reactive radicals like in PECVD (see Figure 1.6 for an overview of this method for the case of an a-CH deposition from an Ar/C_2H_2 mixture, studied in this manuscript). This method of DLC deposition is the preferred one for industrials due to its versatility, scalability, and availability (commonly used in many other applications). However, they do not produce the hardest films because the ionization degree is rather small. Nowadays, a lot of attention is drawn toward the High-Power Impulse Magnetron Sputtering which involve short pulses at high powers to enhance the ionization degree and improve film quality without sacrificing the high deposition rates.

Chapter 2 *Literature Review*

This chapter presents the description of Plasma Chemical Reactions (PCR) that can happen inside the plasma phase of an acetylene discharge focused on the reactions important for magnetrons (Section 2.1). Description of the available simulation models for simulating low-temperature plasmas, with examples of such models applied to acetylene containing discharge and their main findings (Section 2.2).

2.1 Plasma-Chemical Reactions

Low-pressure plasma reactor, like a magnetron, produce cold plasma, where electrons have high energies but do not collide often enough with gas atoms to obtain a thermal equilibrium. Usually, the temperature of ions and neutral species are only few hundred degrees above room temperature, whereas electrons can carry tens of eV of energy. Hence, the most important reactions for cold plasmas from simulation perspective are electrons collisions with the gas atoms or gas molecules. Electrons collisions produce some new electron and ion pairs, which fuel the plasma; but they also sometimes break molecular bonds and produce reactive radicals, or create excited species.

Cross sections are the probability of one type of collision to occur expressed in m^2. They depend on the kinetic energy of the colliding particles in their centre-of-mass reference frame, and they have sometimes an energy threshold below which the reaction cannot occur. They are of crucial importance for PIC-MC simulations and therefore for this study. Even though many studies of the plasma-chemical reaction (PCR) of acetylene are available, it is hard to determine the probable reaction pathways and their cross-sections, since the hydrocarbon chemistry can be complex and involve many species. For example, one study of acetylene plasma in a radio frequency discharge conducted by Ming Mao et al. [34] considered no less than 78 species containing up to 12 carbon atoms, and around 400 volume reactions. Their simulation was what is called a fluid model, meaning that the electrons are simulated by solving the two terms approximation of the Boltzmann equation, coupled with transport equations based on the drift-diffusion approximation, which decouples the electric field-induced drift from the thermal diffusion. This approach allows the authors to treat more molecules species as the calculations are not limited by computation time, as for PIC-MC simulations. In our case, we must limit the number of species. The comparison of the predictions of their model with mass spectrometer data lead them to conclude even though they obtained correct proportions for the leading neutral, cations and anions, they are forgetting many lesser abundant species and heavier clusters.

According to many studies the reactions occurring in acetylene plasma involve first, ionization and breaking of the hydrogen bonds of the C_2H_2 molecules into radical and ionic species, then polymerization occurs leading to the creation of heavier hydrocarbons [32,35–38] that in term could give rise to nanoparticle nucleation and growth. One polymerization pathway leading to the formation of nanoparticles and soot is via the formation of PAH or polycyclic aromatic hydrocarbon [34,37,39,40]. But some other polymerization pathways are possible, like the one for example based C_2H and C_2H^- which is sometimes reported to be important in the formation of $C_{2x}H_y$ species with even number of carbons in C_2H_2 containing discharges [34]. This nucleation of carbon nanoparticles has been studied by many authors and although interesting, it will not be as important for us as we are working at low pressure precisely to avoid their formations (see Valerie De Vriendt et al. [36]). Nonetheless, we can expect heavier hydrocarbons to form inside our reaction cluster and the polymerizations path must be investigated.

2.1.1 Cross sections and reaction rates

The reaction probability between two particles is defined as the cross section $\sigma_{AB}(v_{rel})$, with $v_{rel} = |\overrightarrow{v_A} - \overrightarrow{v_B}|$. It is a function of the collision energy or of the relative velocity of the two particles expressed in m^2. For example, the collision of two hard spheres will have for cross section $\sigma_{hs} = \pi(r_1 + r_2)^2$, which gives for typical radii values a cross-section in the range of 10^{15}–10^{16} cm^2 [32]. However, cross sections can exceed by several orders of magnitude this geometric one in case where there is an attractive force between reactants, or be much smaller if for example the reaction is endothermic.

Let us call the density of both species n_A and n_B and their velocity distribution function $f_A(\overrightarrow{v_A})$ and $f_B(\overrightarrow{v_B})$. Then the reaction probability of particle A with particle B on a path of length dx is (according to [32]):

$$\begin{aligned} P_{coll}(dx) = \ & n_B dx \int [\sigma_{AB}(v_{rel}) f_B(\overrightarrow{v_B})] d\overrightarrow{v_B} \\ = \ & n_B \langle \sigma_{AB} \rangle dx, \end{aligned} \qquad \text{(Eq. 2.1)}$$

The collision frequency of A with B is:

$$v_{AB} = v_A n_B \langle \sigma_{AB} \rangle, \qquad \text{(Eq. 2.2)}$$

And, the mean free path between two collisions is:

$$\lambda_A = (n_B \langle \sigma_{AB} \rangle)^{-1} \qquad \text{(Eq. 2.3)}$$

One useful set of parameters to study the chemical dynamics in gaseous system or in plasmas are the reaction rates. The reaction rate R_{AB} of a reaction between A and B represents the number of times this equation occurs by second for a given volume and is given by:

$$\begin{aligned} R_{AB} &= n_A n_B \int\int [v_{rel} \sigma_{AB}(v_{rel}) f_A(\overrightarrow{v_A}) f_B(\overrightarrow{v_B})] \, d\overrightarrow{v_A} d\overrightarrow{v_B} \\ R_{AB} &= n_A \, n_B \langle v_{rel} \sigma_{AB}(v_{rel}) \rangle \end{aligned} \qquad \text{(Eq. 2.4)}$$

It is often possible to find “reaction rate coefficients” for chemical reactions in tabulated databases. Those coefficients tell us how often a reaction occurs if multiply them with the density of all the reactants, plus the eventual parameters on which they depend. The rate coefficient k_{AB} for a reaction involving two species is defined by:

$$k_{AB} = \langle v_{rel}\sigma_{AB}(v_{rel})\rangle \qquad \text{(Eq. 2.5)}$$

It has the unit of m^3s^{-1} and gives when multiplied by the densities a reaction rate in $m^{-3}s^{-1}$. In the same manner one can define the rate coefficient for a three-specie reaction in m^6s^{-1}.

The dependence of the reaction rates on v_{rel} is really a dependence on the energy of the constituents. In fact, the excited states of particles will have to be considered as special species since their probability of reacting will be different from the ground state ones. This make it harder to obtain reliable data on reactions in reactive plasmas, since species can be excited in many ways by the energetic electrons.

Most of the times when the collision involves electrons the probability of a reaction to occur will be given as a cross sections, and when the collisions is between atoms, molecules, or ions this probability of reaction will be given in term of a reaction rate with a possible dependence on the gas temperature and other macroscopic parameters. However, in cold plasmas heavier particles are considered at thermal equilibrium whereas electrons are at higher energies and usually their energy distribution is not purely thermal. In this case, the reaction rate could be obtained from integrating the cross-sections together with the electron energy distribution function (EEDF) as in (Eq. 2.4).

2.1.2 The acetylene molecule

In the context of amorphous carbon deposition with low pressure plasmas many precursors where considered but the most commonly used are acetylene (C_2H_2) and methane (CH_4). Acetylene is an interesting precursor inside plasma reactors for several reasons. Firstly, it has a strong triple bond (9.97 eV) that is usually conserved, hence the spectrum of products and reactions is promoting hydrocarbons with pair number of carbon atoms. One advantage of C_2H_2 is that it has the fewer hydrogen atoms per carbon whereas methane contains four times more hydrogen than carbon. This hydrogen to carbon ratio is important because the percentage of hydrogen contained in a film will greatly influence its properties [41–44]. C_2H_2 is unstable at room temperature and can decompose in an exothermic reaction forming soot through the HACA mechanism (hydrogen abstraction and C_2H_2 addition which create aromatic compounds (PAH) [45]). This mechanism is also present in low temperature plasmas as shown by many experimental and theoretical studies [32,40,42,46], and it could be the preferred path for the polymerization occurring in the plasma phase [46]. In fact the capacity for hydrocarbons to form polymers is well known and is a key factor for applications like nanoparticles or carbon nanotubes formation [32,47,48]. Since acetylene is studied for many applications and domain (Fusion, PECVD, Combustion, Astrophysics, Bio-medical) there is an extensive number of measurements, articles, and reviews about its properties. For example, Mi-Young Song et al. review article [49] on "Cross Sections for Electron Collisions with Acetylene" compiled and reviewed all available data on electron-acetylene collisions. Another review paper from J. Benedikt [32] is often cited as a reference for acetylene based cold plasma and has greatly inspired the following discussion.

Collisions for other hydrocarbons molecules that might be produced during C_2H_2 containing discharges are also available in the literature and the most complete set in terms of number of species with C_xH_y are from the articles of Janev and Reiters [50] which comes from experiments and theoretical calculations for fusion research, hence as stated by Mi-Young et al. [49], those cross sections may contains some uncertainties at low kinetic energies like the one involved in cold plasma discharges.

2.1.3 Electron collisions

❖ **Total scattering, momentum transfer and elastic collisions**

Total scattering is the sum of all possible collisions. It can be directly measured in swarm experiments but it is of no use for kinetic and chemistry models since what matters is the decomposition of collisions between particles in distinct reactions with their associated cross sections. The elastic scattering englobes momentum transfers as well as vibrational and rotational excitations, and is available for acetylene, including differential elastic scattering cross sections (depending on the collision angle). However, the momentum transfer collisions are more interesting since they play a key role for the diffusion of species.

Thanks to the inclusion of the exact elastic cross sections, diffusion computed by Monte-Carlo simulations can become more accurate than with simpler collision models that use the hard sphere or variable soft sphere approximations. This difference is significant for energetic species like electrons. There are data on momentum transfer collisions between electron and many molecules, including C_2H_2 [49,51,52] (see Figure 2.1) and C_2H [53]. Mi Young et al. recommended values come from good agreements between three sources, two theoretical and one experimental. One interesting feature of electron elastic collisions with acetylene is the $^2\Pi_g$ resonance centred around 2.5 eV [54–62]. The momentum transfer cross sections at very low energy is not defined with accuracy since the sources reported cross section differ from simple to triple.

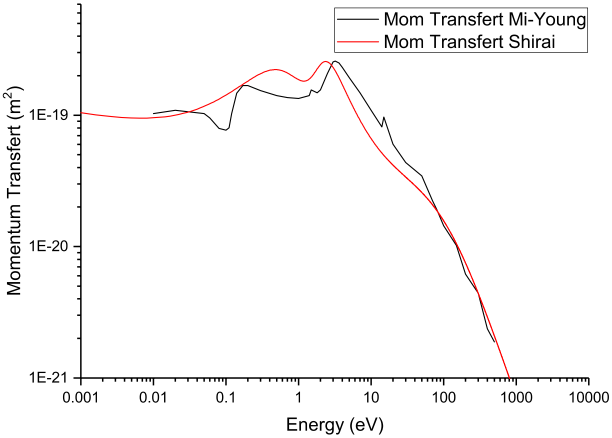

Figure 2.1 The momentum transfer collision cross section from Shirai et al. 2002 [51] *compared to the one recommended in Mi-Young et al. 2017* [49].

❖ Electron impact ionizations (EII) and Dissociative Ionizations (DI)

The most important reactions are the ionizations as they feed the plasma by creating new free electrons[7] that will themselves be accelerated by the electric field, leading to even more ionizations. The cross sections for ionizations all share some common traits with a lower energy threshold and similar shapes (see Figure 2.2). Bellow that threshold the ionization is not possible unless the atoms are already excited because of previous collisions. For example acetylene ionization threshold is 11.40 eV [51], but ionized acetylene with electronic temperatures of 2 or 3 eV can occur because the acetylene molecules easily get excited electronically, rotationally or vibrationally; and this will lower the amount of energy needed to abstract an electron. This stepwise ionization process although important might be neglected in some cases when the pressure is low or if the excited states are very unstable. In our case, stepwise ionization is very unlikely since our working pressures is low, around 1 Pa.

---

[7] *One other source of new electrons is the secondary emitted ones from ions colliding with surfaces .*

Dissociative ionizations are reactions where an ion is formed, but is quickly dissociated in one charged species and one or several neutral ones. The excess energy is shared between the products as the kinetic energy. Those reactions often have a higher threshold than EII and thus a lower probability but they are the main source of radicals[8]. When the injected precursor is not reactive on its own at low temperature (like acetylene) they are the initial step for the PCR and for polymerization.

The cross sections of EII and DI as fitted by Mi Young Song et al. [49] are presented in Figure 2.2. The most probable DI is the reaction $C_2H_2 + e \rightarrow C_2H^+ + H + 2e$, which is 10 times less probable than the EII at 20 eV but produce the very reactive species H and C_2H^+. Within the framework of this thesis, the EII and DI of other species than C_2H_2 and Ar will not be considered since C_2H_2 and Ar are by many orders of magnitude the dominant species. Therefore, the ions considered here and produced by EII and DI are by order of importance: Ar^+, $C_2H_2^+$, C_2H^+, H^+, CH^+, C_2^+, and C^+.

There are other ways to ionize a particle like when the kinetic energy of two molecules or atoms exceeds the ionization potential of one, but this cannot happen in cold plasma. Also, the chemical energy of colliding neutrals may result in ionization according to the so-called associative ionization processes or Penning ionization. However, at

---

[8] *Reactive species with free electrons.*

very low pressure (bellow 1 Pa) the probability of this reaction that required successive collisions is neglectable.

Double and triple ionizations are also possible for electron energies above 40 eV and often results in dissociation. For example, the cross section for the formation of H^+ above 100 eV is mainly due to the double ionization of C_2H_2 followed by a dissociation [63]. However, the probability is always lower than single ionization for magnetron's typical EEDF[9], and therefore we will neglect them.

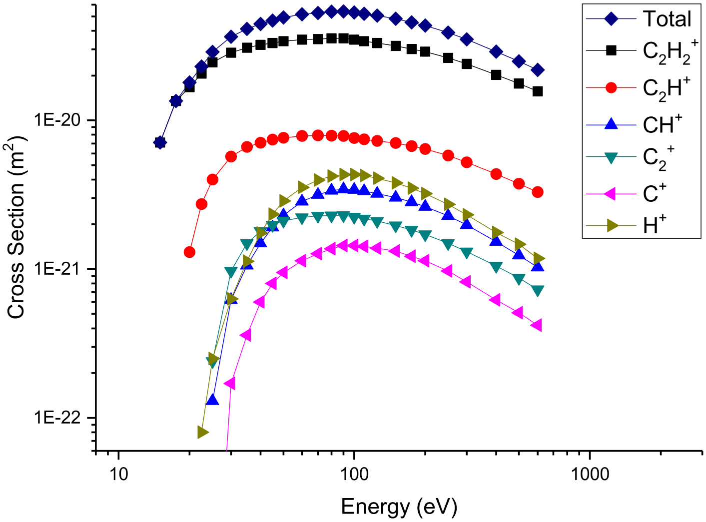

---

[9] *Typical magnetron EEDF are shaped as Bi-Maxwellian distribution with a first temperature close to the plasma potential (2-4 eV) and a second temperature close to the energy threshold of the main EII (10-20 eV)* [6,10,64].

Figure 2.2 Cross sections of electron impact ionizations (EII) producing $C_2H_2^+$ *and all dissociative ionizations (DI) of acetylene best fit proposed by Mi Young et al. 2017* [49].

❖ Electronic Excitations (EE) and Dissociative Excitation (DE)

Electronic Excitations (EE) reactions are important for plasma simulations even if step-wise ionizations or excited species are neglected because they absorb a lot of energy from excited electrons and define the shape of the EEDF [64]. Argon is notorious for having metastable states [16,38,65–70] which can survive longer than other excited states, and hence have more probability to interact with other particles. In particular they can produce some more ionization in what is known as the Penning process [6]. This is why it was studied and integrated in many simulations or experiments involving C_2H_2/Ar mixture. As reported by Gordillo-Vázquez et al. [71] the reaction:

$$Ar^*\left(n = 2\ {}^3P_{0,2}\right) + C_2H_2 \rightarrow C_2H_2^+ + Ar + e, \qquad \text{(Eq. 2.6)}$$

has a reaction rate of 3.5×10^{-10} cm^{3}s^{-1} which makes it a fast reaction. However as stated before this Penning ionization process is more important for higher-pressure plasmas than in magnetrons and is neglected for us because of pressures below 1 Pa.

Sometimes electronic excitation leads to an unstable excited state which results in the breaking of the molecules. Electron Impact Dissociations (EID) or Dissociative Excitation (DE) is a good way to form radicals in their neutral states hence they will not be attracted by the cathodes and have more time to further react in the gas phase. For the acetylene molecule, the most probable reaction includes removing one hydrogen atom in the reaction:

$$C_2H_2 + e \rightarrow C_2H + H + e \qquad \text{(Eq. 2.7)}$$

Threshold energies for EID of acetylene determined by photoabsorption experiments are 7.5 eV for H/C_2H, 8.7 eV for C_2 /H_2, and 10.6 eV for CH/CH pairs [49]. Based on the bond energy of the C-H bond a rough estimate of $1{\sim}2\times10^{-16}$ cm^2 for the cross section of the EID that produces the C_2H radical at 15 eV is given by Mi-Young et al., but the analytical formula given in Janev and Reiters [52] yields a value of around 5×10^{-15} cm^2 for the same energies. In this work, we will use the Mi-Young et al. fits as they are easier to implement and probably more accurate as Janev and Reiters data tend to be less precise at low energy.

❖ Rotational and Vibrational Excitations

Molecules have additionally to electronic excitations, vibrational and rotational excitations which are usually responsible for the major part of energy exchange between electrons and molecules [41]. In cold plasmas if the vibrational-translational relaxation is slow, the vibrational and rotational temperatures can become high. For example, temperatures of T_{rot} = 1190 K and T_{vib} = 1940 K have been measured in an ETP plasma with argon and acetylene as precursors, with the cavity ring down spectroscopic technic [72].

Acetylene has five main energy levels of vibrational excitation:

Table 2 Vibrational modes and excitation energies for C_2H_2*. Taken from* [49].

Symbol	Mode	Energy(eV)
$\boldsymbol{\nu_1}$	Symmetric C-H stretch, σ_g^+	0.421189
$\boldsymbol{\nu_2}$	Symmetric C-C stretch, σ_g^+	0.245712
$\boldsymbol{\nu_3}$	Asymmetric C-H stretch, σ_u^+	0.411238
$\boldsymbol{\nu_4}$	Symmetric bend, π_g	0.0754729
$\boldsymbol{\nu_5}$	Asymmetric bend, π_u	0.0903944

Excitation levels ν_1 and ν_3 as well as ν_4 and ν_5 are similar energy wise (see Table 2). In fact, those levels are degeneracies and the measurements reported can only give cross section of merged levels ν_1/ν_3 and ν_4/ν_5.

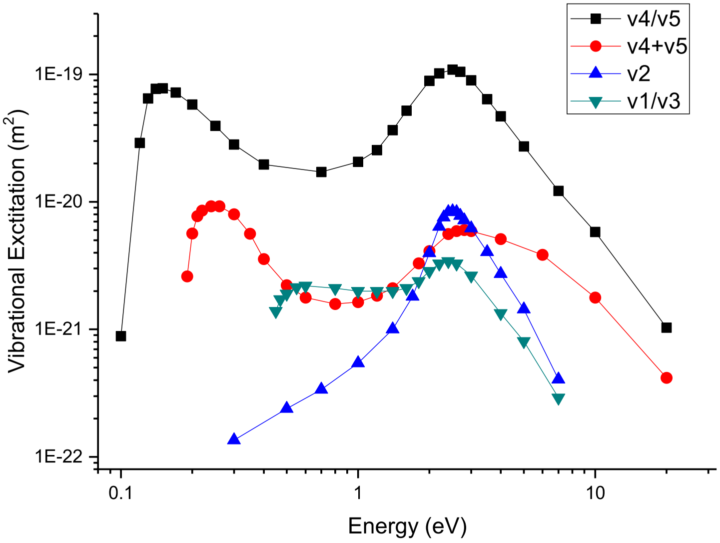

Figure 2.3 Suggested fit for the main vibrational excitation cross sections of C_2H_2 by electron impact, data from Mi-Young et al. [49].

The only data available for rotational excitation is from the ab initio theoretical calculation of Thirumalai et al. [73] which provides the cross section for several energy level transitions for collisions at 10 eV. The reason for this lack of experimental data is the high symmetry of acetylene, which makes those cross sections small and hard to determine.

❖ Electron Attachment (EA) and Dissociative Electron Attachment (DEA)

Electron Attachment is the process by which an electron attaches to a molecule which then becomes negatively charged (i.e. $C_2H_2 + e^- \rightarrow C_2H_2^-$). Given the difficulty to add an electron to the valence shell, the acetylene anion $C_2H_2^-$ is unstable with respect to auto detachment [40]. The privileged way to produces anion is then by DEA collisions.

Dissociative Electron Attachment (DEA) is the process by which an electron collides with a molecule and its energy is enough to break a bond, creating two or more reactive species including one negative ion, and distributing the excess energy amongst the reactants' kinetic energy. As for rotational and vibrational excitations, cross sections have been measured for C_2H_2 in beam or swarm experiments. This reaction is resonant which means that it only occurs within a limited energy range.

The DEA reaction $C_2H_2 + \mathrm{e} \rightarrow C_2H^- + H$ can produce a C_2H^- anion which is much more stable than the acetylene anion due to a larger electron affinity [40]. Despite the fact that the cross sections for this reaction and the other DEA of acetylene are around 4 orders of magnitude lower than DI and EII (see Figure 2.4), it can still produce a substantial amount of anion that might get trapped in the plasma bulk and have a long residence time. For the simulation of nanoparticle formation in RF discharge in C_2H_2, De Bleecker et al. [40] considered this reaction to be important because additionally to the aforementioned trapping of the anions in the bulk, those anions can initiate chains of polymerizations reactions in what is known as the Winchester mechanism [74] which they suspected to be the seeds for nanoparticle formation. They are referring to an experimental study from Deschenaux et al. [75] which reported a great number of negative ions from mass spectrometry measurements in a similar discharge. However, Valérie de Vriendt et al. experiments on the PECVD of acetylene in magnetron systems reported that this polymerization pathway lead to the formation of oligomers with poor hydrogen content (C_nH with n>4) which were not seen in mass spectrometry experiments [42]. This made them suspect that the prominent polymerization pathway is the HACA mechanism which consists of successive reactions of hydrocarbons with C_2H and H. In the hybrid model presented by Mao et al. [76], the negative ions were ignored to save computational effort on the simulation of acetylene containing ICP discharge for CNT growth, even if it had been shown in [34,40] that anions were playing a key role during nanoparticle formation, they explained that the proposed mechanism for the formation of CNTs from a previous study showed that the concentration of anion is at least one order of magnitude lower than electrons which justified their choice.

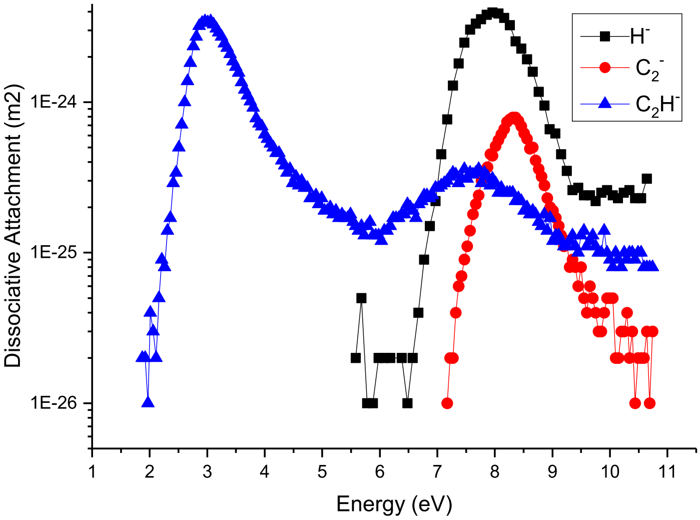

Figure 2.4 Dissociative Electron Attachment (DEA) cross sections of acetylene: (Black) $C_2H + H^-$*, (Red)* $C_2^- + H_2$*, and (Blue)* $C_2H^- + H$ *(data from* [49]*).*

❖ Dissociative Recombination (DR)

Recombination is the process by which an ion recombines with an electron (e.g. $e + Ar^+ \rightarrow Ar$). This process is usually highly inefficient since the excess energy can only result in excitation of the recombined species which is possible only at certain energy levels or a third body partner or radiative transfer. Dissociative Recombination (DR) is the combination of a recombination followed by a dissociation of the ionic species (e.g. $e + C_2H_2^+ \rightarrow C_2H + H$). It is a fast reaction since Coulomb attraction bring the reactant together; and it is possible for a wide range of energy since the excess energy will be distributed among the products.

Muland and Mc Gowan [77] have provided, cross sections for the dissociative recombination of C_2^+, C_2H^+, $C_2H_2^+$, and $C_2H_3^+$. The cross sections for DR reaction with hydrocarbons are weakly dependent on the species, inversely proportional to the electron energy and high for low energies (10^{-13}–10^{-14} cm^2), and that there is no threshold (see Figure 2.5). The author remarked this species independence and compared those cross sections with previously obtained DR cross sections for other polyatomic species and found only small differences with other hydrocarbons. These finding will allow us to make the hypothesis that, if we want to include other DR in our chemistry model, similar cross sections apply to other hydrocarbons of which no experimental data are available.

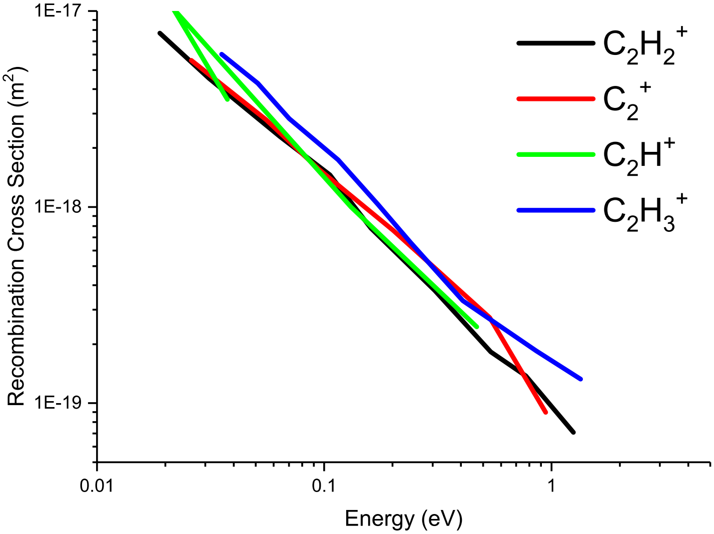

Figure 2.5 Dissociative Recombination (DR) cross sections of several hydrocarbon ions that are interesting in C2H2 plasma from Muland and Mc Gowan [77].

When there are many ways to break a molecular ion through DR, the probability of each reaction branch (or branching ratio) must be determined by some dedicated experiments. Derkatch et al. [78] measured those branching ratios for $C_2H_2^+$ recombinaison at collision energies between 0 and 7.4 meV, and found that the main DR channel is the one producing C_2H + H and C_2 + 2 H with branching ratios of 0.50 ± 0.06 and 0.30 ± 0.05 respectively. The branching to CH + CH was measured to be0.13 ± 0.01, whereas two other energetically-allowed channels were found to be almost negligible.

Branching ratios and cross sections for the DR of other species are also available in the literature, C_2H^+, $C_2H_3^+$, and $C_2H_4^+$ in [79] and C_2H^+ and $C_2H_4^+$ in [80]. The DR branching ratio of C_2H^+ is the most important for this work aside the one for acetylene ion because, as stated preciously, the DI cross section that gives C_2H^+ is only one order of magnitude smaller than the EII of acetylene hence there is probably a great number of ethynyl ions in our plasma phase. However, when the molecular ions are in an excited state the relative abundances of the dissociation products can change.

Table 3 Branching ratio for the Dissociative recombination of $C_2H_2^+$ *from Derkatch et al. 1999* [78]

Reaction	Exothermic part	Branching ratio
$C_2H_2^+ + e \rightarrow C_2H + H$	5.8eV	0.5
$C_2H_2^+ + e \rightarrow C_2 + H + H$	0.2eV	0.3
$C_2H_2^+ + e \rightarrow CH + CH$	1.2eV	0.013
$C_2H_2^+ + e \rightarrow CH_2 + C$	2.4eV	0.05
$C_2H_2^+ + e \rightarrow C_2 + H_2$	5.1eV	0.02

Table 4 Branching ratio for the Dissociative recombination of C_2H^+ *from Ehlerding et Hellberg 2004* [80]

Reaction	Exothermic part	Branching ratio
$C_2H^+ + e \rightarrow C_2 + H$	6.60eV	0.43
$C_2H^+ + e \rightarrow CH + C$	3.98eV	0.39
$C_2H^+ + e \rightarrow C + C + H$	0.43eV	0.18

Another interesting property of DR is that it is an exothermic reaction, which redistributes the energy released when breaking the bonds in the form of kinetic energy distributed amongst the reaction products (see

Table 4)

2.1.4 Other reactions

- **Ion-Ion reactions**

Ion-Ion binary recombination $(A^+ + B^- \rightarrow A + B)$ is the most important ion loss reaction in electronegative gases at low pressure, whereas at higher pressure and with a non-electronegative gas, 3-body recombinations are more probable. This collision cross section exceeds the normal gas-kinetics collision cross section by several order of magnitude due to Coulomb attractive force. Similarly to DR, those cross sections are weakly dependent on the ionic species [81] and there is an empirical formulae to calculate them [82]. In the model of Mao et al. 2008 [34] they considered some of those reactions as a way to neutralize hydrocarbon anions with H^+, H_2^+ and $C_mH_n^+$ ions. The cross sections for those reactions where approximated for all hydrocarbon anions to be dependent only of the ion and they used Hickman's formulae [82], and equal to 3×10^{-14}, 2×10^{-13} and 5×10^{-13} cm^3s^{-1} respectively.

- **Ion-Neutral reactions**

Due to the polarizability of particles, Ion-Neutral reactions are typically 10 times faster than Neutral-Neutral ones. Because the polarization potential scales with distance as r^{-3}, the resulting cross section (or Langevin radius [6]) is inversely proportional to the velocity; hence the cross section for Ion-Neutral collisions are temperature independent.

Those reactions rates for hydrocarbons have been measured in a variety of experiments [83–87] and are available in the UMIST database [88]. There is in general less experimental measures of reaction rates for reactions involving hydrocarbon anions, and this is why in the C_2H_2 chemistry models of De Bleecker et al. and Mao et al. 2008 [34,40] the authors had to use for some reactions involving anions reaction rates for SiH_n^- ions with SiH_m radicals.

One type of interesting Ion-Neutral reaction for cold plasmas is the Charge Transfer (CT). It is still relatively fast and is the most important source of hydrocarbon ions in remote plasmas like ETP reactors. As for DI, it can also dissociate the colliding partners, and this is why for ETP models like [41], the pathways for acetylene chemistry involve primarily dissociations induced by collisions with Ar^+. Reaction rates and branching ratios of CT reactions between Ar^+ ion with several hydrocarbons at thermal energy, including C_2H_2, have been measured by Tsuji et al. in flowing afterglow apparatus [89].

- **Neutral-Neutral reactions**

Neutral-Neutral gas phase reactions are usually temperature dependent with different rates for the forward and reverse reaction directions. Reactions with unsaturated hydrocarbon radicals like C_2H can be highly exothermal [90]. Their measurement must be carefully conducted as those reactions also depend on many parameters like: pressure, temperature, and the presence of other species. Rates for reactions with hydrocarbons are found in extensive databases like the NIST [91] or

GAPHYOR [92] but their applicability to our case must be checked as well as their precision.

It is known that acetylene-containing plasmas are prone to polymerize or form nanoparticles. We already presented the HACA mechanism (H abstraction C_2H_2 addition) which can lead to increasing size hydrocarbons or nanoparticle formation as well as the Winchester mechanism which revolves around successive reactions with ethynyl (C_2H^-) anions.

Table 5 Reactions in Gas Phase considered in [42] *as the initial steps of the C_2H addition and H abstraction chain for the plasma polymerization in an acetylene containing Magnetron Sputtering reactor.*

Reaction	Rate constant [cm^3s^{-1}]
$C_2H + C_2H_2 \rightarrow C_4H_2 + H$	5.8×10^{-11}
$C_2H + C_4H_2 \rightarrow C_6H_2 + H$	6.6×10^{-11}
$H + C_2H_2 \rightarrow C_2H_3$	3.5×10^{-13}
$H + C_4H_2 \rightarrow C_4H_3$	1.2×10^{-12}
$H + C_6H_2 \rightarrow C_6H_3$	1.6×10^{-12}
$H + C_4H_3 \rightarrow$ \`$H_2 + C_4H_2$	2.4×10^{-11}
$H + C_6H_3 \rightarrow H_2 + C_6H_2$	6.6×10^{-11}
$C_4H_3 + C_2H_2 \rightarrow C_6H_5$	4.0×10^{-12}
$C_6H_5 + H \rightarrow C_6H_6$	4.0×10^{-12}

There is also the polymerization chain that involve C_2H insertion and H abstraction described by De Vriendt et al., Mao et al. and J. Benedikt [32,34,42,47]. Many studies reported the important role of the C_2H radical which seems to be an important precursor for carbonaceous film growth as well as nanoparticle formation when the precursor is C_2H_2 [5,34,42,46,71,76,93]. Considering all the cross-sections presented above, it seems that the main sources of C_2H will probably be, by order of importance: (i) the DI of acetylene, (ii) followed by DR and (iii) DE which are however more probable than DI at low electron energy.

❖ Plasma chemistry pathways investigation

Mao et al. [34] have investigated the chemistry of a capacitive coupled RF discharge (13.56 MHz) in a parallel plate reactor for a pressure of 27 Pa and a power of 40 W in C_2H_2. They included in their model 400 reactions and 78 species. The reactions include electron impact collisions with hydrocarbons containing up to twelve carbon atoms including:

- Cluster Growth through C_2H insertion
- Hydrogen insertion
- Hydrogen abstraction
- Cluster growth through acetylene insertion
- Other neutral–neutral reactions
- Cluster growth through hydrocarbon anions with C_2H_2
- Cluster growth through H_2CC^- with $C_{2n}H_2$
- Reactions between H^+ and hydrocarbons
- Reactions between H_2/H_2^+ and hydrocarbons
- Reactions between C_2H/ C_2H^+ and hydrocarbons
- Reactions between C_2H_2/ $C_2H_2^+$ and hydrocarbons

- Reactions between C_2H_3/ $C_2H_3^+$and hydrocarbons
- Reactions between C_2H_4/ $C_2H_4^+$and hydrocarbons
- Neutralization reactions of hydrocarbon anions with H^+, H_2^+, $C_nH_m^+$

The purpose of that study was to understand the pathways of nanoparticle formations and they were able indeed to form bigger negatively charged hydrocarbons, eventually trapped in the plasma long enough to further grow. They compared they simulation with Deschenaux et al. [94] mass spectrometry measurements and although there are less species in the model, the same general trend was observed.

For the negative ions, a slightly less good agreement was observed. Those results have been improved in a subsequent article by including dissociative attachment of large hydrocarbon ions with the idea of generating anionic seeds for nanoparticles formation. Indeed, in the first model, the anion where primarily obtained by the so-called Winchester mechanism from successive reaction with C_2H^- hence there were a downward trend towards larger hydrocarbons.

Another example of the investigation of the plasma chemistry pathways in C_2H_2 plasmas is the study of Gordillo-Vázquez and Albella [93] on the influence of the pressure and power of an RF discharge in C_2H_2/H_2 and Ar with low C_2H_2 content (less than 1 %). They showed that when the total pressure decreased, the concentration of C_2, C_2* and C_2H increased whereas the concentration of other species decreased or remained constant. In addition, they noted no significant effect of the power change. Since the condition with the lower pressure corresponds to their best experimental conditions for nanodiamond film deposition, they conclude that C_2 and C_2H play a crucial role in the nanodiamond film growth.

These examples demonstrate that plasma chemistry can be investigated with numerical models, like for example fluid models, but also that the included reactions greatly affect the results and every prediction should be carefully compared with experimental measurements.

❖ On the reaction rates incertitude and the model complexity limitation

As plasma chemistry models become increasingly complex by adding new reactions, it is tempting to believe that they will gain in predictivity since more possible pathway could be explored. Unfortunately this is often not the case [7]. Reaction rates obtained by theoretical calculations or experimental measurements are available from reliable sources and compiled in extensive databases. However, those reaction rates often lack precision or are obtained from very different sources which might be accurate only for very different conditions (e.g. different pressures, temperatures, energy ranges). Thus, they can introduce great uncertainties if combined in a model containing hundreds of reactions. M. M. Turner [95] demonstrated this sensibility with a helium-oxygen plasma chemistry global model containing around 400 reactions. He carefully checked the uncertainty associated with every reaction in the model and used a Monte-Carlo procedure to quantify the resulting uncertainty on the prediction from the model. He reported that in average, the precision on final species densities were uncertain with a relative error up to a factor of two to five, and in certain cases up to a factor of ten. He later showed in another article [96] a method to reduce a chemistry model to its most influencing reactions. The purpose of this analysis being to reduce the difficulty of analysing the predictions uncertainty by focusing on reducing the uncertainties associated with only the most influential reactions. The collateral benefit of such a sensitivity analysis is the reduction of the reaction set, since they showed that similar predictability could be attained with a model containing only 50 reactions (compared to the 400 initial reaction set).

Another algorithm was developed by Lehmann [97] to identify the most significant pathways by performing an analytical investigation on the most probable reaction based on their reaction rates. This algorithm can now be freely download as part of the PumpKin software [98]. Peerenboom et al. [99] also demonstrated the benefit working with only a subset of the possible reactions. They used for this purpose the principal component analysis (PCA).

A summary of all reactions included in the model is presented in Table 6 and

Table 7.

Table 6 Summary of principal electron collisions reactions and their interest for the modelling of acetylene low temperature plasmas.

Symbol	*Name*	*Reaction*
EII	*Electron Impact Ionization*	$e + A \rightarrow 2e + A^+$
DI	*Dissociative Ionization*	$e + AB \rightarrow A + B^+ + 2e$
—	Stepwise Ionization	
EE	Electronic Excitation	$e + A \rightarrow e + A^*$
EID	Electronic Impact Dissociation	$e + AB \rightarrow e + A + B$
DE	Dissociative Excitation	$e + AB \rightarrow e + A + B^*$
—	Vibrational & Rotational Excitation	
DEA	*Dissociative Electron Attachment*	$e + AB \rightarrow A^- + B$
	Recombination	$e + A^+ \rightarrow A$ or $e + A^+ + B \rightarrow A + B$
DR	Dissociative Recombination	$e + AB^+ \rightarrow A + B$

Table 7 Summary of the main sources for hydrocarbon electrons collisions cross sections relevant for acetylene low temperature plasmas.

Articles	*Reactions*	*Species*
Janev 2002 [53] *Janev 2004* [52]	*EII, DI, DE, DR, DEA, CT*	$CH_{1,4}, CH^+_{1,4},$ $C_2H_{1,6}, C_2H^+_{1,6},$ $C_3H_{1,8}, C_3H^+_{1,8},\ H^+$
May 2008 [100]	*DEA*	$C_2H_2,\ C_4H_2$
Song 2017 [49]	*Review on e + C_2H_2*	$C_2H_2, C_2H_2^+$
Muland McGowan 1980 [77] *Amitay 1996* [101] *Derkatch 1999* [78]	*DR*	$C_2^+,\ C_2H^+,\ C_2H_2^+,$ $C_2H_3^+$ $CH, C_2^+,\ C_2H^+,\ C_2H_2$
Thirumalai 1981 [102]	*Elastic, and Rotational*	C_2H_2
Tsuji 1993 [89]	*Dissociative CT*	Ar^+ $+ CH_4, C_2H_{2,4,6}, C_3$
Shirai 2002 [51]	*EII, DI, DE, DR, DEA, CT… (138 reactions)*	$CH_4, C_2H_6,\ C_2H_4,$
Toshio 2006 [103]	*CT (with C^+)*	$CH_4,\ C_2H_2,\ C_2H_4,$ $C_3H_8C_3H_6, (CH_2)_3$

2.2 Plasma Modelling

This chapter describes the different models as found in the literature for simulating the plasma phase involved in this work. We restrict ourselves to technics that are relevant for cold plasma simulations and for reactive magnetron sputtering in Ar/C_2H_2. Some simulated processes based on other precursor (mainly CH_4) are mentioned for demonstrating simulation technics but their findings might not apply to our case.

There are several types of numerical models used in the literature to simulate PECVD, including, by order of numerical resources demands: analytical models, global models (0D), one or two-dimensional fluid models, Boltzmann models, hybrid models, Direct Simulation Monte-Carlo (DSMC) and Particle-In-Cell Monte-Carlo (PIC-MC).

Plasma phase modelling schemes for PECVD usually include both physical (e.g. electron heating, fluid dynamics, diffusion, electric or magnetic field calculations) and chemistry (evolution of densities and reaction rates). Usually different methods are more suited to investigate one of those two aspects [2,47]. Simulations of acetylene PECVD are most often done with fluid models and global models that trade precision about the plasma behaviour[10] for a more complex chemistry with more species. With hydrocarbons, the PCR can be rather complex and involve polymerizations, but we expect from previous experimental

---

[10] *Those models usually do not take account of the out-of-equilibrium behaviour of cold plasmas, and the energy transport is simplified.*

results [39] a quite low density of reactive, hence the PCR complexity should be reduced compared with for example RF PECVD.

For a more general review of plasma computer modelling the reader could refer to the reviews from Bogaert et al. [2,47].

2.2.1 Analytical and global models

Analytical models can resolve plasma behaviour fast but they rely usually on restrictive approximations. F. Gordillo-Vázquez and J. Albella [65] are presenting a quasi-analytical model for a RF inductively coupled plasma (ICP) in a $C_2H_2/H_2/Ar$ mixture, based on time and space averaging of the Electron Boltzmann Equation coupled with rate and balance equations.

Global Models, or 0D models, are one of the most popular modelling approaches for PECVD in complex chemical environment (see Figure 2.6) because they are fast and not limited by the number of species and reactions they can consider. The principle of those models [1] is to solve an approximation of the Boltzmann equation in order to get the EEDF by assuming a uniform electric field, uniform collision probabilities, and uniformly distributed velocities for the electrons. Then from the EEDF and cross sections, reactions rates are calculated and the evolution of the species densities is deduced form balance equations. One of the main disadvantages of these models is that the particle transport is neglected, which in most case plays a critical role as the species are usually not created in the direct vicinity of the substrate.

However, this problem can be circumvented in the case of ETP (Expanding Thermal Plasma) reactors because the plasma source is remote and the gas constituents have an important velocity along one axis; the evolution through time of the densities can be seen as an evolution through space [67,104]. Global models can also include a detailed surface chemistry model [105,106].

As pointed out by Hurlbatt [7] and Turner [96] those models, as all plasma models including a complex PCR, suffer from the lack of precision on the reaction rates databases that are generally taken from astrophysics or fusion researches [88,91] and hence are generally precise only to an order of magnitude at the temperatures and electron energies that matters for cold plasmas. As they have shown, the results of global models can be very sensitive to the variation of some reactions constants and the tendency to add more reactions and species to a model to improve it could in fact be counterproductive.

2.2.2 Fluid models

Fluid models are an improvement on global models because transport equations based on the drift-diffusion approximation are introduced. Generally, in one or two dimensions, those models are widely used in an array of applications (see Figure 2.6). Although 1D and 2D models gives similar results [107] the advantage of 2D simulation is that the homogeneity profile of film deposition can be inferred from the variations of the flux onto the substrate. We found only one article [108] trying to apply a fluid model to a magnetron discharge without using a hybrid approach. This is because magnetron discharge plasmas are very inhomogeneous and charged particles trajectories are influenced by a magnetic field. In this article, the author applies a 1D fluid model of the plasma phase by considering an equivalent reactor where the magnetic field lines over the target are artificially straightened. Many examples of fluid and hybrid models of acetylene containing plasmas have been published by the PLASMANT group of Antwerp [2,34,40,47,76,109–113]. M. Mao et al. [34], presented a 2D fluid model of a RF discharge in C_2H_2 including more than 400 reactions and 42 species (up to species containing 12 carbon atoms). In this study, they compared with quite good agreement their findings with mass spectrometry measurements made by Deschenaux et al. in a similar reactor. In De Bleecker et al. [40], the authors coupled a 1D fluid model with a sticking model for the surface interactions of a RF discharge in C_2H_2. Results generally include density profiles of the species as well as their flux towards the substrate, which helps identifying the growth precursor and important radicals, and the decomposition rate of the precursor gases injected which is of importance for optimizing the deposition process.

Some models are assuming the shape of the EEDF (e.g. Maxwellian) instead or solving the Boltzmann equation, or do not take account of the self-induced electric field, which makes them not self-consistent but easier to set. These assumptions prevent taking account the non-equilibrium behaviour of the plasma. In Ivanov et al. [109] (Similar results were also found in [114]) a 1D PIC-MC model and a fluid model are compared for an ICP discharge. They found significant differences at a certain power with the appearance of a bi-Maxwellian energy distribution for the electrons which cannot be reproduced with the fluid model. This discrepancy comes from the fact that the ionization rate must be fully determined by the local electric field in the fluid approach.

The PCR of C_2H_2 is simulated by those models usually with good agreement with measurements. Most common findings are: (i) species with pair number of carbons are usually more represented [41,93,113], (ii) the pressure is found to have a big impact on the chemistry [39,93]. Most of these models are used to simulate reactors operating at pressures above 10 or 20 Pa (RF, ICP, MW…), whereas in reactive magnetron sputtering the pressure is usually bellow 1 Pa, hence the PCR might be different. For example, at lower pressure long reactions chains like presented in [46] can be neglected. Additionally, lower pressures might be an advantage when using kinetic models like DSMC or PIC-MC since the computing resources they require will be less important.

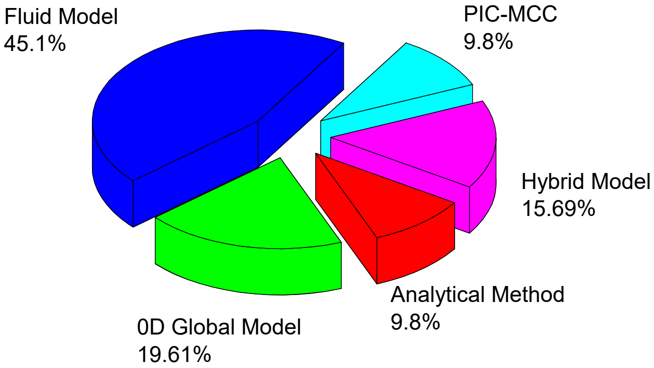

Figure 2.6 Repartition of the 51 numerical models from Mohan 2011 review chapter on modelling deposition from Plasma Chemically Enhanced Deposition (PECVD) of amorphous carbon. [47]

2.2.3 Hybrid models

Models mixing different approach to get the advantages of each, also known as hybrid models, are gaining a lot of popularity in recent years. Usually, one model[11] is used for the energetic species (electrons and maybe ions), and a fluid model for the others species considered at thermal equilibrium. In this way, the model is self-consistent (i.e. the

---

[11] *Either PIC-MC, DSMC or a solver based on the 2-terms approximation of the Boltzmann equation.*

locally created electric field is considered), fast and may take the complex chemistry into account.

Ariskin et al. [111] published a good example of a hybrid model of a CCP discharge in Ar/C_2H_2. They used a PIC-MC model that include few species, including $C_2H_2^+$ and excited states of C_2H_2, to ignite the plasma and extract information on the EEDF and ions densities. A 1D fluid model was then used with 42 species and 146 reactions to study the chemistry inside the chamber. They noticed a change in the plasma characteristics when C_2H_2 was injected showing the importance of the gas mixture for the plasma. They showed that the excitation cross sections of complex molecules like C_2H_2 have important impact on the EEDF since electrons energy are absorbed by the gas more efficiently.

May et al. [115] used another hybrid scheme which consists of a Boltzmann model for energetic species together with a 0D global model and a detailed surface chemistry model. They reviewed in their paper all the theoretical efforts towards understanding diamond-like film deposition in Microwave assisted plasma CVD (or MW). Mao et al. [113] developed an hybrid model for their ICP plasma reactor to improve their existing 2D fluid model [110]. They added only few reactions and species but studied the effect of different gas mixture with the help of a PIC-MC model coupled with the fluid model. They found long chained carbon containing molecules and ions where the main precursor for nanotube formation even at low pressure (50 mTorr). Those heavy ions can enhance physical sputtering of amorphous carbon film of the catalyst particles, which is an important part of carbon nanotube formation, and might also plays a key role for our studied process in magnetrons. Interestingly they found that the plasma does not contain much atomic carbon, hence CTNs growth must be linked to the decomposition of hydrocarbon species at the catalyst surface in a chemisorption process. In this article, a numerical parameters study was performed, varying the gas ratios, gas pressure, coil power, bias power, and substrate temperature. This wide parameter sensibility analysis has been made possible by the hybrid approach, which allows fast calculations.

Typical results of hybrid models include the power density, the gas temperature, the electron temperature, the densities, and the fluxes towards the substrate. Since our system is different, the results from the studies presented above might not be relevant but it is good to note that in general few radicals (not necessary the same) are found to be leading every process. This is interesting since the cost of including many species in PIC-MC models is high, and it is possible that a very restricted set of species could give a good insight and allow the prediction of general behaviours. Among all reactive species, the most common one known to play a critical role in many PECVD studies of hydrocarbon containing plasmas, is atomic hydrogen. We therefore added it to our PCR model.

2.2.4 Particle-in-Cell Monte-Carlo

Direct Simulation Monte-Carlo (DSMC) are a very accurate way to simulate gas transport, gas phase reactions and surface interaction. Mathematically simpler than other approaches, they consider all species as superparticles that account for millions of actual particles. The motion of those superparticles are calculated with Newton's laws, and they are colliding according to probabilities taken from tabulated cross section data. Their validity relies on the usage of a great number of super particles to achieve accurate statistical predictions. Therefore, they usually require longer calculation time and more computing power than fluid models.

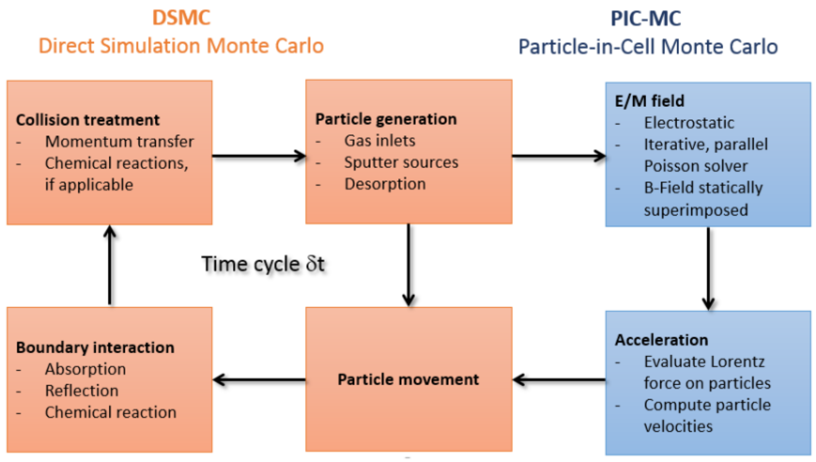

Figure 2.7 Schematic description of DSMC and PIC-MC algorithm. Taken from the presentation given by Dr. A. Pflug at the 15th Int. Conference on Coatings on Plasma Surface Engineering PSE Garmisch-Partenkirchen, September 11, 2016

Particle-in-cell Monte-Carlo (PIC-MC) simulations differs from DSMC ones by taking account of the effect of charged particle transport on the electric-field, making charged particle transport "self-coherent". For this purpose, the particles are confined to cells and the electric field is recomputed at each time-step from Poisson's equation (see Figure 2.7). Those models are even more resource demanding therefore they are usually perceived as not suited for complex chemistries. However, PIC-MC simulations can be used together with other models to take advantages of their better description of the PCR. Already mentioned is the article from Ivanov et al. [109] which compared a 1D fluid model to a 1D PIC-MC model of an RF discharge with CH_4/H_2. The authors demonstrated the superior predictivity of PIC-MC, in particular for the calculation of the EEDF when there are out-of-equilibrium or non-local effects[12]. Miagawa et al. presented [116] a PIC-MC model of a pulsed plasma immersion ion implantation (PIII) in C_2H_2 at 3 Pa. They included $C_2H_2^+$, C_2H^+, CH^+, H^+, CH_2, CH, H species, but the set of cross

---

[12] *The study of cold plasmas often relies on the hypothesis of quasi-equilibrium or quasi-neutrality, which implies that the number of positively and negatively charge balances out everywhere in the chamber. Another criterium is the "ideality" of plasmas which refers to the fact that all ions are shielded by electrons with a shield which is small compared to ion motions (see 1.1). Magnetrons at low pressure exhibits some out-of-equilibrium behaviour for the electrons close to the target.*

sections was limited to Dissociative Ionizations (DI) and double ionization of C_2H_2, EII of H, and elastic collisions. Other electron impact collisions were ignored because the plasma densities were quite low and species created were always several orders of magnitude lower than the precursor densities. It was noted that the effect of the positive pulse was to bring the plasma closer to the high aspect ratio substrate, and that both the pressure and the SEEY were the most important parameters.

Since ion bombardment plays indeed an important role for the deposition, and since the behaviour of charged particles is better modelled with PIC-MC, some authors use this types of models only for the charged particles, or decided to include only a few representative reactions and species to account for the PCR and its effect on deposition [109,117–119].

Proshina et al. published a study of a CCP in CH_4 at 18 Pa with a 1D PIC-MC model. They included only the two ionic species CH_4^+, and CH_5^+, and several neutrals H_2, C_2H_6, C_2H_4, C_3H_8 and C_2H_2. They included many ionizations, excitations, and charge transfers. They showed that because of the resonant charge transfer of CH_4^+, the IEDF of both ions where quite different at low frequencies. They also showed that the frequency influenced the density and energy of electrons as well as the dissociation rate. They compared there results with the hybrid model of Ivanov et al. [109] and found that their PIC-MC model gives a lower ion flux toward the substrate. They noticed a correlation between the IEDF and the experimental deposition rate of amorphous carbon which indicate that ions plays an important role for the deposition in CCP reactors.

Hirata and Choi presented a PIC-MC model of a pulsed discharge ion implementation technique (PBII&D) PECVD deposition of amorphous hydrogenated carbon using only e, Ar and Ar^+ [119]. They studied the homogeneity of deposited film on high aspect ratio micro-trench and showed that the distribution of thickness and hardness of the film is correlated with ions angles and energy distribution and that it could be tuned by changing the shape of the pulse. They noticed that the film thickness was decreasing and the hardness increased with the depth in the micro channels. Their model although using only one species could explain partly those observations, but the second important factor of these inhomogeneities was identified as the radical depletion, which cannot be rendered with only Ar.

Alexandrov and Schweigert [118] presented a 2D PIC-MC simulation of a CCP discharge in methane with a set of species restricted to few neutrals and only one ion. They justified this assumption by the fact that density profile of all ions are in general similar [107]. They observed as in experience a transition between two regimes with the evolution of the voltage. They latter applied a fluid model to the PCR inside the chamber from the densities and energy distribution functions obtained from the PIC-MC simulation and find good agreement with experiments.

In an article about PIC-MC simulations of planar magnetron cathodes [120], a demonstration of a recently discovered phenomenon called spokes is presented. Instabilities in the form of plasma wave revolving around the racetrack[13] are forming in front of magnetron cathodes and they seem to have a great influence on the plasma characteristics. They cannot be predicted with fluid models, since the detailed motion of particles is reproduced only in kinetic models like PIC-MC. In a comparison study between a 2D and a 3D PIC-MC simulation [120], Pflug et al. demonstrated that good qualitative agreement can be obtained for the simulation of a magnetron discharge with a 2D model, but that only the 3D model was able to reproduce quantitatively the I-V characteristic and proper electron transport for discharges like magnetron with such characteristically out-of-equilibrium behaviours like plasma spokes.

Another motivation to choose the PIC-MC modelling approach for studying the magnetron PECVD of a-CH is that the working pressure is very low (bellow 1 Pa), hence the characteristic Knudsen number[14] describing the particle flow characteristic is high (above 0.1), which

---

[13] *The « racetrack » is the erosion left on the target by the sputtering due to ion bombardment in magnetrons. It follows the magnetic field and its shape is due to the electrons confined above the target and rotating around it due to* $E \times B$ *drift* [143].

[14] *The Knudsen number is a dimensionless parameter giving an insight in the characteristics of a particle flux, and is equal to* λ/D *with* λ *the mean free path and D a characteristic distance of the flux (see* [122]*).*

means that the gas phase cannot be treated as a continuous medium and each particles' trajectory must be considered.

One problem with most PIC-MC simulations is that they are limited by the charge densities and powers attainable since with increasing power, smaller cells and time steps are required, and this increases the computational cost dramatically[15]. Fortunately, as demonstrated in the study of Tonneau et al. [64], it is possible to extrapolate simulation results to higher powers as long as the studied discharge remains in the normal "glow discharge" regime (see 1.1).

---

[15] *The computational cost proportional to the number of cell and time-step, hence augmenting the simulation's power should have a quartic cost for a 3D simulation (doubling the power multiplies the load by 16).*

Chapter 3 *Methods*

3.1 The PIC-MC model

Here are described the PICMC-algorithm used, geometrical meshing of the chamber and the simplifications that were operated to speed up simulations, as well as a description of the magnetic field generation, and a description of the numerical parametrization.

3.1.1 The PIC-MC algorithm[16]

In 1872, Ludwig Boltzmann derived the kinetic theory of gases and a general formulation of their dynamics. It has become one of the most powerful tools of scientists with applications from fluid dynamics to material sciences and in particular for the study of plasmas (e.g. for weakly ionized gases, fusion, astrophysics) [121]. However, this set of equations were derived from purely physical considerations of the gas particles, translated into a system of differential equations, which now (since around 1960) can directly be solved via computer simulations without any recourse for an analytical solution. The validity of such simulations is no lesser than this mathematical formulation, and complex effects like ternary collisions, chemical reactions, thermal

---

[16] *The PIC-MC simulation code used during this work was developed and provided by partners from the Fraunhofer Institute. The description of the algorithms used by this simulation are given here for reference purpose and authorized by Fraunhofer IST. For more detailed description of the code the reader could refer to* [120,133,144–146] *or contact directly the main author of the code, and head of the simulation group: Dr. Andreas Pflug (andreas.pflug@ist.fraunhofer.de).*

radiations, or plasma-surface interactions can be integrated with much less added complexity [122]. The general way to implement a Particle-in-Cell Monte-Carlo algorithm is to solve at each time step the equations of motions for each particle, equating their accelerations to the sum of all the forces acting upon them, then calculating the macro-quantities of interests (e.g. density, pressure, electric and magnetic field) over a grid division of the simulation volume. In the case of a non-relativistic plasma, the equations of motion have the following form:

$$\frac{d\vec{X}_i}{dt} = \vec{V}_i,$$

$$\frac{d\vec{V}_i}{dt} = \frac{e_i}{m_i}\left(\vec{E}(\vec{X}_i) + \vec{V}_i \times \vec{B}(\vec{X}_i)\right) \tag{Eq. 3.1}$$

For $i = 1..N$, with $\vec{E}(\vec{X}_i)$ and $\vec{B}(\vec{X}_i)$ the electric and magnetic field, at the location of the cell containing the particle i, which position and velocity are given by $\vec{X}_i$ and $\vec{V}_i$ respectively.

The electric and magnetic field can be calculated by solving the Maxwell's equations from ρ and $\vec{J}$ the charge and current densities calculated from the position and velocity of all particles in the simulations and averaged at every cell.

For magnetron reactors[17] the magnetic field is imposed by permanent magnet and thus does not vary much with the motion of the charged particles. In such electrostatic case the Maxwell's equation reduces to the Poisson equation, which in the most general case is written:

$$\Delta\phi + \frac{\nabla \epsilon_r \nabla \phi}{\epsilon_r} = -\frac{\rho}{\epsilon_0 \epsilon_r} \qquad \text{(Eq. 3.2)}$$

with ϵ_r the relative dielectric permeability of the background.

As seen in Figure 2.7 depicting the PIC-MC general scheme, solving those two equations is done sequentially and not simultaneously. In order for simulations to remain coherent, this creates some limitations regarding the time steps and other numerical parameters (for more details on the numerical parametrisation see section 3.1.4).

To calculate the electric field from (Eq. 3.2) the "Gauss-Seidel" method with successive overrelaxation (SOR) is used (for a description of the algorithm see [123]). This method relies on small adjustment of the electric field at each cell until a convergence is attained. It is initially a long process to obtain a stable electric field with this method; However, since the results of the previous time steps are reused and since the charged particles do not move much between two iterations, the calculations become gradually faster.

---

[17] *This is also the case for most cold plasma reactor types*

As for many other numerical simulation schemes PIC-MC algorithm use discretized time steps. In order to solve the dynamics equation with high accuracy and speed, “leap-frog” methods are commonly used. They are reversible solvers, which relies on the explicit calculation of the velocity and position of the particle at the next time-step from the previous ones; but with velocities calculated in between time steps, making the calculation time-centred:

$$\frac{\vec{X}_{k+1} - \vec{X}_k}{\Delta t} = \vec{V}_{k+1/2},$$

$$\frac{\vec{V}_{k+1/2} - \vec{V}_{k-1/2}}{\Delta t} = \frac{e}{m}\left(\vec{E}_k + \frac{\vec{V}_{k+1/2} + \vec{V}_{k+1/2}}{2} \times \vec{B}_k\right) \qquad \text{(Eq. 3.3)}$$

To solve the equation above, several methods are possible. However due to its accuracy, efficiency and long-time stability the Boris method is the preferred one for plasma simulations [121,124]. It can be written for the general non-relativistic case as follows:

$$\vec{X}_{k+1} = \vec{X}_k + \Delta t \vec{V}_{k+1/2},$$

$$\vec{V}_{k+1/2} = \vec{u}_+ + q\vec{E}_k \qquad \text{(Eq. 3.4)}$$

With $\vec{u}_+ = \vec{u}_- + \left(\vec{u}_- + \left(\vec{u}_- \times \vec{h}\right)\right) \times \vec{s}$, $\vec{u}_- = \vec{V}_{k-1/2} + q\vec{E}_k$, $\vec{h} = q\vec{B}_k$, $\vec{s} = 2\vec{h}/(1 + h^2)$, and $q = e\Delta t/2m$.

This is often the most time consuming part of the simulation, as it requires around 39 operations per superparticle. The other important algorithm not discussed yet is the collisions routine. Since it will be too time consuming to check every single particle trajectory for collisions (*O*(N^2)), the simulation uses the No Time Counter (NTC) method.

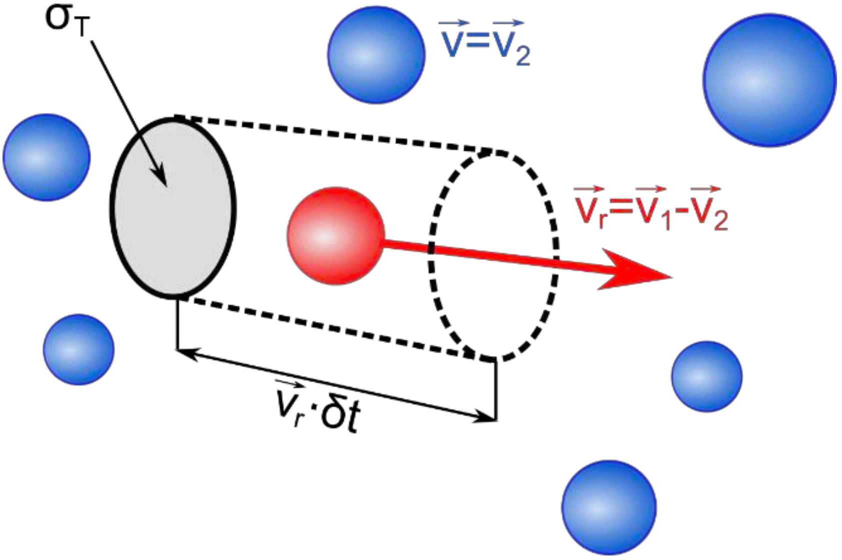

Figure 3.1 Collision of a test particle with velocity v_1 *(red) with particles of the same cell with velocities* v_2 *(blue)*

The NTC method main goal is to diminish the number of collisions to check by finding a maximal amount of collisions per collision partners and per cell. To do that one particle of type 1 is chosen randomly in the cell and a volume is calculated based on the maximum product of relative velocity between this particle and particles of type 2 and the cross section[18]. The maximum probability of a collision between

---

[18] *A cross section in this context is the collision probability given in* m^2*. It usually depends on the relative speed (or energy) of the two particles. See section 2.1.1 for more precisions.*

particle 1 and 2 to happen in this cell is then given by the ratio of this volume to the cell volume:

$$p_{12.max} = \frac{< \sigma \mathrm{v_r} >_{max} \delta t}{V_c} \qquad \text{(Eq. 3.5)}$$

With v_r the relative velocity, σ the cross section (that can depend on v_r), and V_c the volume of the cell. Passing from this probability to an expected maximum number of collisions per cell is done by considering the Nreals[19]:

$$N_{preselect} = N_1 N_{r1} N_2 N_{r2} P_{12.max} \qquad \text{(Eq. 3.6)}$$

With N_y the number of superparticles of type y in the cell, and N_{ry} the Nreal of those superparticles.

After the calculation of this number, $N_{preselect}$ particle pairs are randomly chosen in the cell and a random number is generated. The collision between the selected pair is said to occur if this random number is smaller than $\sigma \mathrm{v_r}/< \sigma \mathrm{v_r} >_{max}$.

In general, many collision types are available between two particle type. For example, electrons hitting a C_2H_2 molecule can ionize (e + $C_2H_2 \rightarrow C_2H_2^+ + 2e$) or dissociate (e + $C_2H_2 \rightarrow$ e + C_2H + H). In this case, the random number generation and test will happen for every

---

[19] *We call Nreal the number of physical particles represented by one superparticle. More on those parameters in section 3.1.4.*

collision type sequentially until one collision is said to happen or the list is exhausted.

Depending on the number of reactions and species, this collision routine can become even more computationally intensive than the other main procedures occurring at every time steps of simulations: (i) the kinetic solver (Boris method), (ii) or the electrostatic field solver (Gauss-Seidel method), (iii) or the data generation (averaging macroquantities on a per cell basis from the positions and velocities of particles).

Finally, particles impinging on surfaces and simulation volume's boundaries are detected based on their position and either reflected, absorbed, or re-injected at another surface. When surface reactions and particle sources are specified a random number is drawn and if the condition is fulfilled, the impinging particle is absorbed or reflected and the new particles are injected based on angular and energetic distributions specified in the parameter files.

3.1.2 The chamber

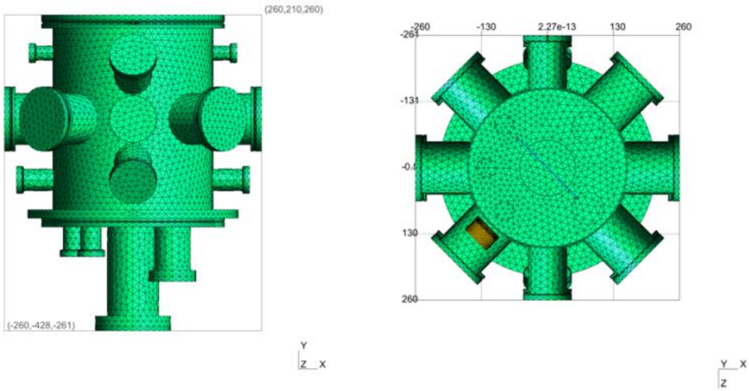

Figure 3.2 Side view (left) and horizontal cut (right) of a 3D mesh of the MANTIS experimental plasma reactor used in this study, obtained from the CAD model provided by the manufacturer. The magnetron is in orange and the substrate position is represented by a blue line.

The reactor used for this study is a composed of a small size vacuum chamber with many ports where standard 2” circular magnetrons can be mounted, as well as measurement devices, substrate holders, or shields. We used principally the following configuration: (i) an unbalanced magnetron with a graphite target operated in DC mode, (ii) a turbo pump with a fixed throttle valve that kept the pressures before discharge at 5mTorr or 1.6 Pa, (iii) variable mass-flow-controller (MFC) gas inlet behind the cathode injecting argon and acetylene, (iv) a grounded substrate holder centred in the chamber and facing the cathode, (v) a removeable shield in front of the substrate with a masked opening to allow multiple deposition without opening the chamber, (vi) various measuring instruments (e.g. MS, OES, QCM). For more details on this chamber the reader could refer to [33].

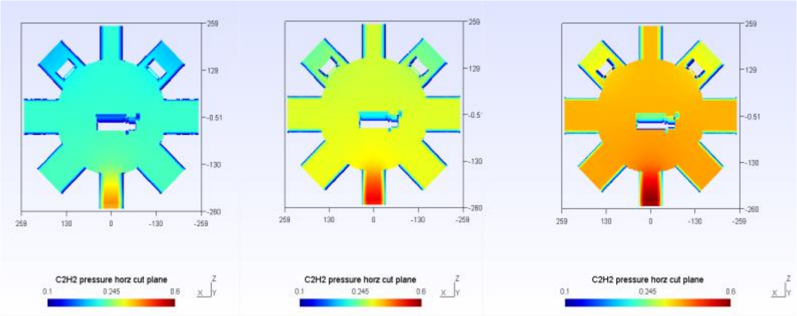

Figure 3.3 Horizontal cuts of DSMC simulations of the gas flow throughout the chamber. The colours correspond to the partial pressure of C_2H_2 in Pa for 3 different fluxes.

DSMC simulations of the gas flow in the chamber proved that the partial pressures of all injected gases are relatively homogenous in the centre (see Figure 3.3). Several membranes[2021] where added on the grounded substrate to sample the fluxes of particles (see Figure 3.4). Those membranes correspond to vitreous carbon samples that where utilized to measure the deposited film composition with ERD/RBS (see Chapter 5).

---

[21] *The "membranes" are oriented meshed planar surfaces added to the model that does not have any interaction with the plasma but only counts the particle passing through them in a specific direction and sample their energies and angles.*

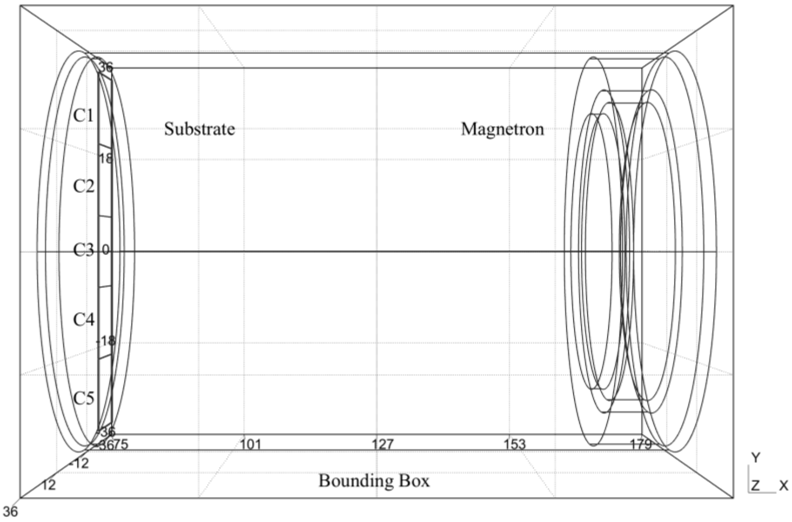

Figure 3.4 Scheme of the deposition chamber used for simulations, with samples from C1 to C5 used for experimental a-CH film depositions. Coordinates are given in millimetres. The magnetron target surface is at x = 166.35 mm, and the substrate surface is at x = 80 mm

To speed up simulations a simplified 3D mesh of the chamber was used: the walls were set to a floating potential acting as a total absorbent for all particles, and a source for Ar and C_2H_2 at the initial pressure. This is like considering that the particles emitted inside a small volume would not affect the homogenous background gas composition will diffusing outward; and that the grounded walls of the chamber are sufficiently far so that the PP at the location of the simulation box to be the floating potential. This assumption on the potential was tested with three simulations: (i) one plasma simulation in a bigger volume, (ii) one with grounded walls, (iii) and one with floating potential walls (see Figure 3.5). It was noticed that the latest parametrisation option (iii) gives result closest to the bigger volume one (i) hence is more realistic.

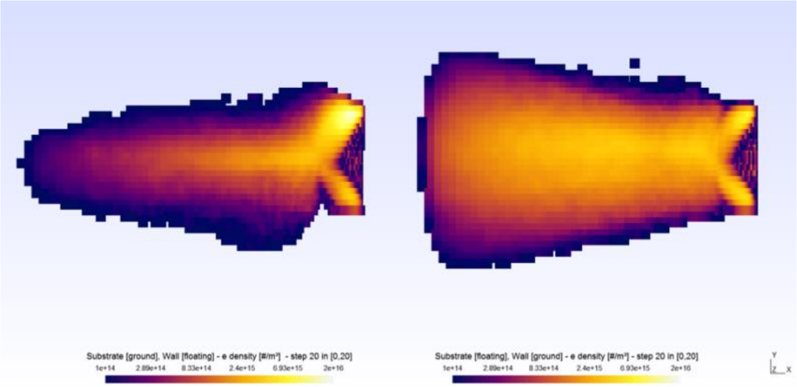

Figure 3.5 Illustration of the effect of grounding the simulation box walls or leaving their potential to the floating potential.

3.1.3 The magnetic field

The magnetic field was calculated prior to simulations using a boundary element method (BEM) from the shape, remanence (1.4 T) and relative permeability (1.05) of the magnets which were cylindrical permanent neodymium magnets mounted on a ferrite yoke (see Figure 3.6).

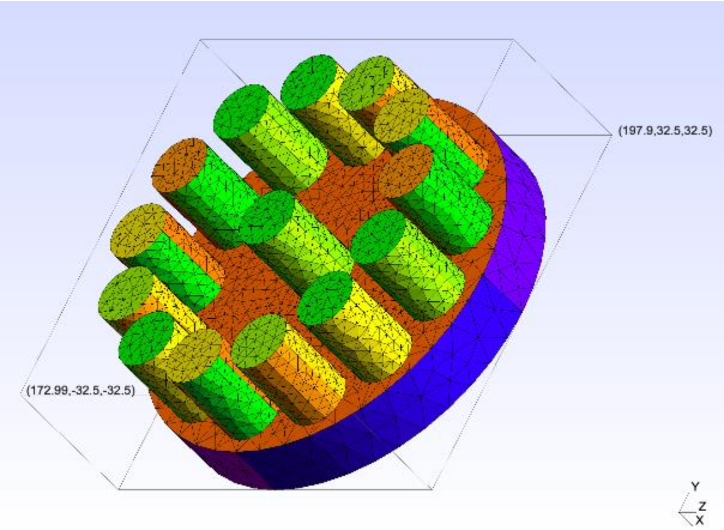

Figure 3.6 3D mesh of the permanent magnets used to simulate the magnetic field.

The resulting magnetic field was parallel to the target at ≈12 mm from the centre (see Figure 3.7). This distance corresponded to the size of the ringed plasma confinement, and to the size of the experimental racetrack (see footnote 13), which is a good indication of the validity of the calculation.

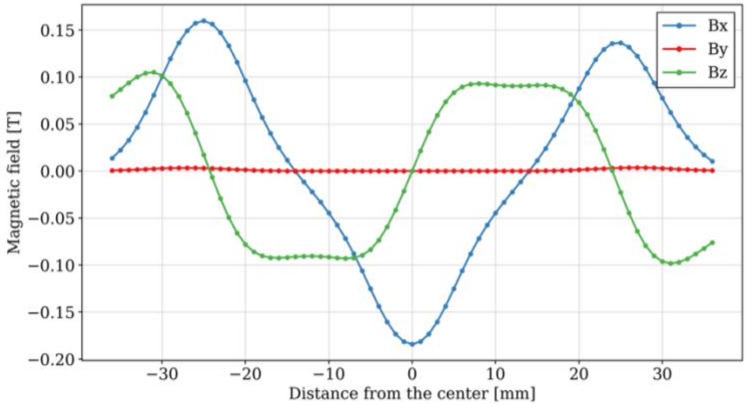

Figure 3.7 Magnetic field over the target's surface vs distance from its centre (x is the normal axis and z is an axis in the cut plane, see Figure 3.4).

3.1.4 Numerical constraints

To optimize simulations but ensure that they remain statistically accurate, numerical constraints had to be respected and the simulation volume had to be divided in several volume segments or "quads", which are simulated on separate CPUs. To avoid limitations due to too many communications between computing nodes, simulations were kept on single nodes[22] by dividing the simulation volume by 5 in the longitudinal direction and by 2 in both other directions, for a total of 20 quads, or 21 CPUs on the 24 available per nodes (see Figure 3.8). Those quads are then subdivided in cells which will contain the super

---

[22] Nodes on the large job queue of the Tiers-1 ZENOBE cluster used (http://www.ceci-hpc.be/zenobe.html), are composed of 24 CPUs and 64 Gb of memory and have a maximum length of 24 hour.

particles. The quad division aimed at having the same amount of computation strain on each CPU. Another use of the quad division is that the cells' size can be adjusted per quad. Thus, it is possible to have small enough cells near the plasma bulk to simulate the complex behaviour of energetic species, and gradually increase the cell size further away from the cathode (from 0.5 mm to 1.8 mm wide). Scaling tests have shown that the speed of PIC-MC simulations was directly correlated to the total number of cells, hence minimizing this number is of crucial importance.

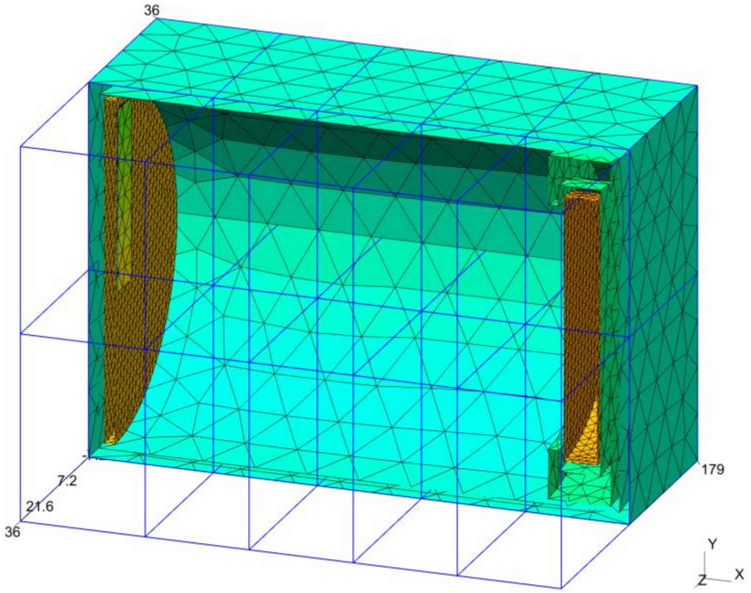

Figure 3.8 Domain decomposition of the simulation box in 20 quads which are to be computed by individual CPUs of the cluster[22].

The time step in a PIC-MC simulation should be sufficiently small to resolve all relevant physical mechanisms (e.g., it should be smaller than the angular frequency of the electron oscillations around the ions). The time step was set to 5×10^{-11} s, as it corresponds to a tenth of the oscillation period for an electron density of 1×10^{15} m^{-3}. Another numerical constraint concerns the cell size, which must remain below 3.4 times the Debye length to properly resolve electrical potential gradients [121,125], which gives a value close to 1 mm in this case. One issue to avoid is cell-hopping, which can occur if the distance a particle moves in one time step becomes larger than the cell width. In our case the fastest particles are electrons and e.g. even at 200 eV with $\delta t = 5 \times 10^{-11}$ s the travel distance is around 0.43 mm so smaller than our chosen cell width. Charged and neutral species are represented with super-particles, which usually comprise a larger number of real particles via a statistical weight factor (further referred to as Nreal). Well-chosen weight factors are crucial since a certain amount in the order of 10 particles per cell are needed to give statistically accurate results and allow all collision pathways to happen, while too many particles render the simulation time and the memory consumption impractical.

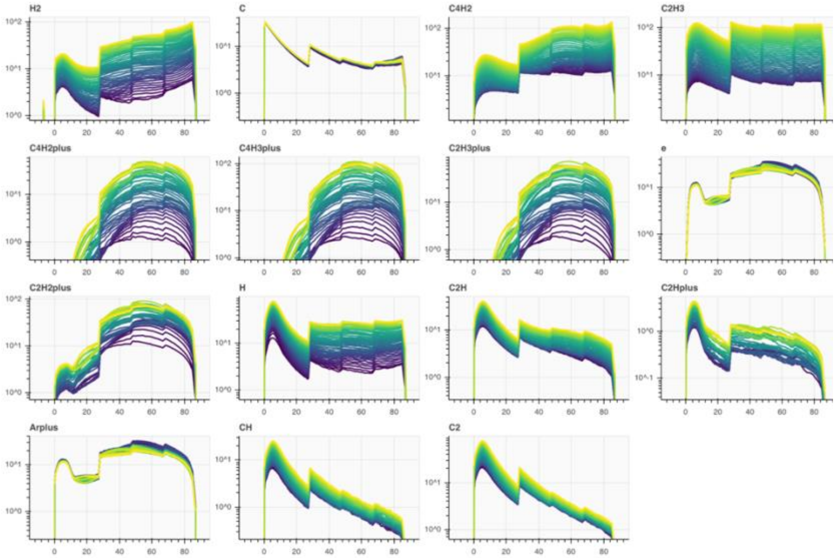

Figure 3.9 Line averaged number of superparticles per cell in a simulation with 20% C_2H_2 at 0.9 W after 300 μs of simulation. Each curve corresponds to a snapshot every 5 μs from the beginning of the simulation (blue) to the end (yellow). The quad delimitation is visible as steps in the data as the cell size was different in every quad.

As can be visible in Figure 3.9 the variability of the cell size implies that the number of particles in a cell varies throughout the chamber. One difficult task was to find cell sizes and Nreals for each species which together can maintain a reasonable number of particles and for every position in the chamber (with densities that can vary up to 2 orders of magnitude) and for every time-step (with densities of radicals and ions that varied from 0 initially to 1×10^{15}–1×10^{16} m^{-3}). Like for a random variable, the precision on any macro quantity calculated per cell is proportional to the square root of the number of particles. Thus, there are two ways to improve accuracy and reduce fluctuations of the simulation: (i) lower the particles Nreal (at the cost of speed), (ii) average any quantity over longer simulation time. With those considerations the numerical scaling parameters were obtained from calculations and trial-and-error, they are shown in Table 8.

Table 8 Physical and numerical parameters of the simulations

Domain size	$100 \times 72 \ \times 72$	$[mm]$
Input power	$0.2 - \ 1.2$	$[W]$
Input power density	$9.8 \times 10^{-5} - \ 5.9 \times 10^{-5}$	$[W.cm^{-2}]$
Temperature	*300*	*[K]*
Species	$Ar, Ar^+, C_2H_2, C_2H_2^+, H, C_2H, C_2H^+, CH, C_2,$ $H_2, C, C_4H_2, C_2H_3, C_4H_2^+, C_4H_3^+, C_2H_3^+$	
Pressure	0.6	$[Pa]$
Magnetron radius	25.4	$[mm]$
Magnets remanence	*1.4*	$[T]$
Cell size	$0.5 \ - \ 1.8$	$[mm]$
Division of the simulation domain in cells	N_X = *[13,13,15,40,40]* N_Y = *[24,24]* N_Z = *[24,24]*	$[cells]$
Division of the simulation domain in mm	D_X = *[24,20,20,20,20]* D_Y = *[36,36]* D_Z = *[36,36]*	$[mm]$
Arrangement of simulation volume segments	$5 \ \times 2 \times 2$	$[quads]$

Time step width	5×10^{-11}	$[s]$
Maximum physical simulation time and related calculation time	1×10^{-3}, 1×10^{6}	$[s]$
CPUs cores used	21	[*CPU*]
Memory used	*12*	[*Gb*]
Weight factors $\boldsymbol{Ar}, \boldsymbol{C_2H_2}$	$1\times 10^{10}\times ratio$	[*particles*]
Weight factors $\boldsymbol{e}, \boldsymbol{Ar^+}, \boldsymbol{C_2H_2^+}$	1.4×10^{5}	[*particles*]
Weight factors for all other species	$6\times 10^{2} - 1.7\times 10^{4}$	[*particles*]
Sampling for the power dissipation	1×10^{-7}	$[s]$
Carbon yield	*0.03*	
Secondary electron emission yield	*0.11*	

3.2 Building the PCR model

The main reactions occurring in acetylene containing low-pressure plasmas have been reviewed in Chapter 2, in particular, all the electron collisions with acetylene and secondary reactions between the reactive species created by those reactions and the background acetylene have been presented. However, including all possible reactions and species in a PIC-MC simulation is impossible as the computational cost would increase exponentially with PCR complexity. In this section we present efforts made toward getting a simpler, yet comprehensive chemistry model.

3.2.1 Radical's lifetime

The computational cost of adding species to PIC-MC simulations is high. Moreover, adding reactions could introduce higher uncertainty due to possible incompleteness of the PCR or imprecision of the CS as discussed above. As already discussed the most important reactions in our case are the electron collisions and in particular dissociations that will create ions and reactive radicals. First models, could be limited to those reactions. Second in term of importance, the reactions between those reactive species and the background C_2H_2 could be fast enough so that most of the particles would react at least once before reaching the substrate or detector. To know if this is the case and if secondary reactions should be included in the PCR some approximative calculation of radicals' lifetime duration can be done. One of the most reactive species created in the plasma will be C_2H and is produced in the following reactions:

Table 9 Main reactions producing the C_2H radical

Reaction	Name	CS [m^2]	Notes
$C_2H_2 + e \rightarrow C_2H^+ + H + 2e$	DI	1×10^{-20}	Only 10 times less important than EII
$C_2H_2 + e \rightarrow C_2H + H + e$	DE	5×10^{-21}	branching ratio 0.51, others C_2, H, H_2, and C
$C_2H_2^+ + e \rightarrow C_2H + H + 5.8eV$	DR	1×10^{-19} (at 1 eV) 1×10^{-20} (at 10 eV)	high cross section at low energy and no threshold

The tight correlation of those reaction to the simple ionisations in the plasma lead us to think that C_2H production rate will be of the same order as the ions production. In a typical 1 W magnetron plasma simulation the ion density is 4 orders of magnitude lower than the background gas density (10^{-4} ionisation degree). Provided that we are working around 5 mTorr or 0.66 Pa, the density of acetylene at 300 K is around 1.59×10^{20} m^{-3}. Which means that the C_2H density if no reactions where consuming it would be in the order of 10^{16} m^{-3}.

The fastest reaction than C_2H will undergo is:

$$C_2H + C_2H_2 \rightarrow C_4H_2 + H\ [1.3 \times 10^{-16}\ \mathrm{m^{-3}s^{-1}}] \qquad \text{(Eq. 3.7)}$$

This mean than, based on [32] the average lifetime of C_2H is:

$$T_{C_2H} = \frac{1}{\rho_{C_2H_2} * k_{C_2H\,loss}} = 48\ \mu s \qquad \text{(Eq. 3.8)}$$

The average times that the C_2H molecule would take to reach the substrate (at 86.35 mm from the target see Figure 3.4) can be calculated from the Brownian motion mean thermal diffusion length:

$$\bar{x}^2 = 2D_{C_2H}T_{diff} \qquad \text{(Eq. 3.9)}$$

With T_{diff} the time, and D_{C2H} the diffusion coefficient which can be approximated based on the Chapman-Enskog theory for C_2H in a typical mixture of 20% C_2H_2 and 80% Ar, by a linear interpolation of the Lennard-Jones coefficients of various other hydrocarbons (see

Table 10 and Figure 3.10) and the following equation for the binary diffusion coefficient of species i in gas j:

$$D_{ij} = \frac{3}{16}\frac{k_b T_{gas}}{P_{tot}}\frac{\left(2\pi k_b T_{gas}/m_{ij}\right)^{\frac{1}{2}}}{\pi\sigma_{ij}^2\Omega_D(\Psi)} \qquad \text{(Eq. 3.10)}$$

with k_b the Boltzmann constant, T_{gas} the gas temperature, P_{tot} the total pressure, m_{ij} the reduced mass and $\sigma_{ij} = \frac{\sigma_i+\sigma_j}{2}$, and $\Omega_D(\Psi)$ a coefficient which depends on temperature and which expression can be found in [111].

We found that the diffusion coefficient of C_2H was 2.76 m^2s^{-1} in a mixture of 80% Ar and 20% C_2H_2; Which means that based on (Eq. 3.9) the average time that it would take for a C_2H molecule to reach the substrate with purely thermal diffusion, is 1.35 ms, which is around 30 times bigger than this radical's mean lifetime. This values also gives us an idea of the length that simulation will have to reach to have representative radical concentrations.

This means that to fully understand the PCR in magnetron DC discharge in acetylene at pressures around 0.66 Pa it is important to: (i) include a second layer of reactions with the reactive species produced in electron collisions, (ii) simulate the plasma discharge for times approaching or bigger than the millisecond.

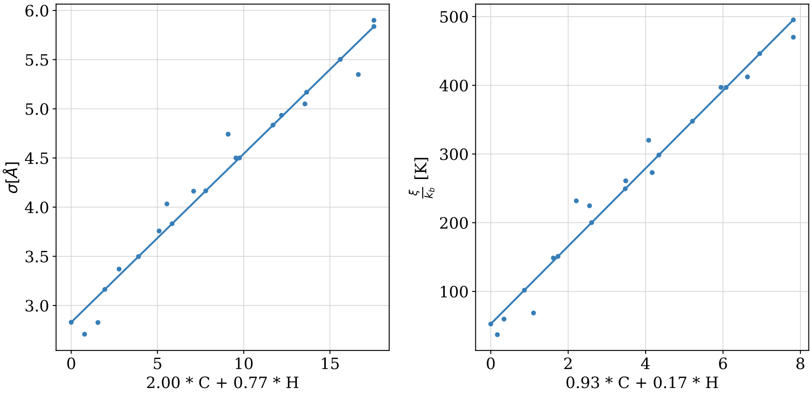

Figure 3.10 Linear regression of the Lennard-Jones parameters of several hydrocarbon species based on the number of carbon and hydrogen atoms.

Table 10 Lennard-Jones coefficients of several species of interest for C_2H_2 plasmas, including the coefficients of C_2H that where interpolated from other values (see Figure 3.10).

Species	**σ (Å)**	**ξ_i/k_b [K]**	**Source**
C_2H_2	4.033	231.8	[40]
H_2	2.827	59.7	[40]
H	2.708	37	[40]
CH	3.37	68.6	[40]
CH_4	3.758	148.6	[40]
C_2H_4	4.163	224.7	[40]
C_6H_6	5.349	412.3	[40]
Ar	3.54	93.3	[111]
C_4H_2	4.5	320	[111]
C_6H_2	5.05	397	[111]
C_8H_2	5.9	470	[111]
C_2H	3.65	168	(Interpolated)

3.3 Experimental methods

Description of the experimental methods used in this study to characterize the plasma phase (in-situ) and the deposited film (film characterization). This is not an exhaustive list of all the available methods, *the reader is invited to refer to these reviews for a broader picture of the available methods* [126–128].

3.3.1 Plasma in-situ diagnostics

- **Mass spectrometry**

To investigate the PCR and identify the species created inside the plasma phase an important tool at are disposition is mass spectrometers (MS). We used to this intent a quadrupole PSM003 mass spectrometer supplied by Hiden Analytical, equipped with a turbo-molecular pump reaching a typical pressure of 10^{-8} mbar and connected to the deposition chamber by a 100 μm in diameter extraction orifice, facing the magnetron target at distance of 10 cm. Mass spectrometry measurements of neutrals were performed in residual gas analysis (RGA) mode and in Secondary-ion mass spectrometry (SIMS) mode for the ions. Neutral species entering the mass spectrometer were ionized inside the spectrometer with a 70 eV electron source to allow their detection. In SIMS mode, the detector was calibrated with a low-power pure argon plasma.

- **Quartz Crystal Micro-balance**

Quartz Crystal Micro-balance (QCM) was used in several experiments as a qualitative deposition rate sensor. It is constituted of a vibrating piezo-electric crystal which resonance changes when film is deposited onto it, thus allowing the measurement of a film thickness live evolution or deposition rate. Even though it is in theory possible to obtain quantitative information on the deposition rate with a QCM via proper calibration, it requires knowing the acoustic impedance of the deposited film which is a complicated information to obtain for a-CH since it depends on the structure of films which strongly depends on experimental conditions like for example the Ar/C2H2 ratio, the substrate distance, or the discharge power. Moreover, QCM can get biased from the evolution of the quartz temperature when bombarded with energetic species, thus a cooling down system should be implemented when the quartz is close to the magnetron. Interesting results obtained with the QCM are presented and discussed in section 5.1.1.

❖ Optical Emission Spectroscopy

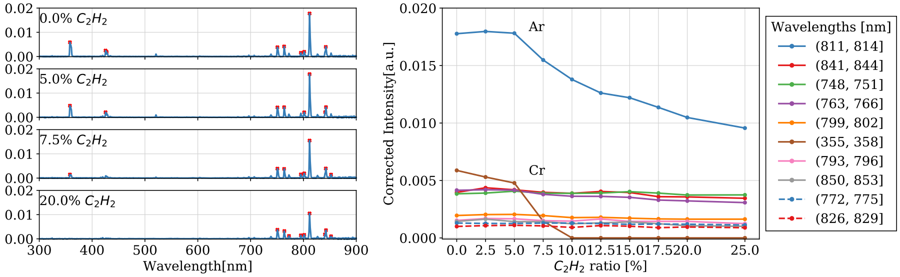

Figure 3.11 OES spectra examples (left) and summary for discharges with varying C_2H_2 ratio at 5 mTorr, and 0.16 A with a chromium target.

An interesting method of in-situ measurements for cold plasmas is optical emission spectroscopy (OES). Many electronically excited species are created within the plasma and they often relax to lower energy level via the emission of photons (hence the term "glow-discharge", see Chapter 1). The wavelengths of these emitted photons are specific to species and energy levels, thus allowing the identification of the amount of species in each excited state. However, since the photo-emission is not directly proportional to the density of particles in an excited state, quantitative information is often impossible to obtain.

In our case, no clearly discernible emission lines were found for the C_2H_2 molecules and its excited states. However, when an acetylene discharge was ignited with a chromium target, we observed that the Cr lines, which comes from the sputtered Cr, where clearly visible and influenced by the C_2H_2 ratio (see Figure 3.11). This probably comes from the fact that the deposition rate augments with the C_2H_2 ratio and thus the cathode's target gets polluted faster

This method of observation can be used to find an optimal C_2H_2 ratio for fast film deposition. Indeed, the discharge speed is proportional to the C_2H_2 ratio as demonstrated in simulation in experiments; however, if too much C_2H_2 is injected in the chamber, an a-CH film gets deposited on magnetron's target faster than it is sputtered, which results in arcing and a quenched discharge. Hence, the chromium OES lines can help to find the maximum ratio of C_2H_2 before the cathode pollution overcomes sputtering.

❖ Langmuir probe

One of the oldest methods to study a plasma discharge is to measure the electron current towards a thin metallic probe embedded in the plasma, while variating its electric potential. The characteristic current-voltage relationship obtained thereby (often called the I-V characteristics), gives valuable information on the plasma potential, floating potential and electronic temperature or more generally on the EEDF (see 1.1 for more details on those terms). It is a very valuable tool to validate PIC-MC simulations as it is one of the most direct way to compare the accuracy of simulations as shown in [129,130]. Unfortunately, in the case of reactive plasma with an high deposition rate of a dielectric film like with acetylene Langmuir measurement are hard to obtain and less reliable [131], hence none were performed.

3.3.2 Film characterization

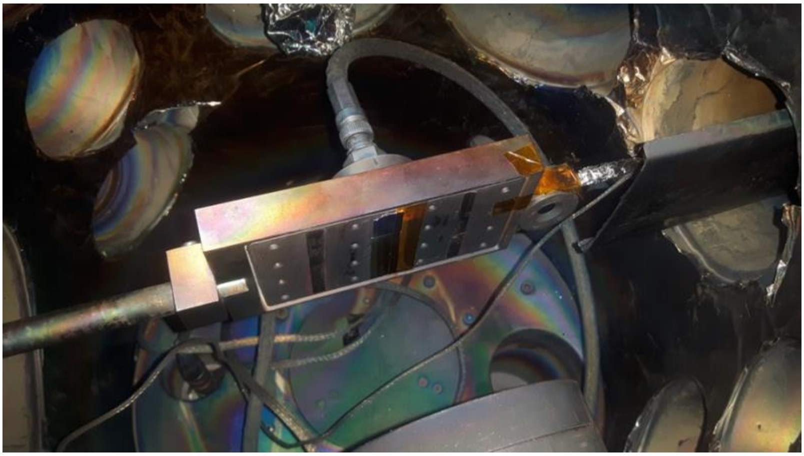

Figure 3.12 Picture of the substrate holder with vitreous carbon samples and a QCM, in the middle of the vacuum chamber.

❖ Contact Profilometer

A contact profilometer[23] is a handy tool that can provide information on film's roughness by dragging a thin diamond stylus on its surface and measuring the vertical resulting force as a function of the position. It can also be used to measure film's thickness if a step is created on the sample by masking some parts of it with insulating tape. This technique is quite reliable if the films are smooth and clean, and can give measurements with height precision of down to 10 nm.

For the experiments presented in Chapter 5, we used a somewhat unusual masking approach which was proven useful in our case. In general, multiple small samples partially masked with Kapton tape are placed in the chamber in various positions giving deposition rates at various points of the substrate holder. To get a better insight on the evolution of the deposition rate over a wide distance from the centre of the substrate holder we used long (6 cm) vertical silicon samples, with a tape mask running along the longest edge. Then the film thickness was measured with the profilometer every 2 mm, giving a thickness profile that span the full height of the substrate holder. Those profiles could then be compared with simulations in term of absolute deposition rate, but also in term of shape of deposition profiles. This

---

last comparing method gave us more confidence on the reliability of the simulation predictions and allowed us to precise the nature of the main deposition precursors.

❖ X-Ray Photoelectron Spectroscopy

X-Ray Photoelectron Spectroscopy (XPS) is a technique based on the stimulated photon emission of atoms from a surface irradiated by X-rays. The energetic X-rays can provide enough energy to atoms located up to 10 nm within a material for breaking covalent liaisons and ejecting non-valence electrons, thereby ionizing them. By measuring the wavelength of the emitted photons precise knowledge on the energy level and their occupancy could be obtained, and thus knowledge about the atomic composition and structure of materials. However, since only non-valence-electrons can be used it is not possible to detect hydrogen and hydrogen bonds with this technique. Another problem of this method is that due to matrix embedding effects and heterogeneities it gives usually only qualitative results.

This technique could be used for a-CH films to retrieve the proportion of sp^2/sp^3 C-H liaisons, since they have a slightly different bonding energy. Since a-CH is non-conductive, its surface might get statically charged and shift the energy measurement. To circumvent this effect an electron-flood gun is used. However, accurate calibration of the energy measurement remains a complex task, even more so without clearly discernible spectrum peaks. Additionally, as for many other types of film, surface pollution must be avoided or etched with e.g. Ar^+ clusters.

XPS measurements were performed on the a-CH samples in an Escalab 250Xi machine (ThermoFishers Scientific, England) with a 1486.7 eV monochromatic Al Kα X-ray source and a 400 µm wide spot. Soft etching with 1000 Ar atoms clusters at 6 kV were performed for 200 s on 2 × 2 mm^2 areas before each measure.

❖ Ion Beam Analysis

Ion Beam analysis (IBA) is a type of analysis that relies on bombarding samples with a beam of high energy ions with a known kinetic energy. The fast ions collide with the sample constituent atoms' nucleus and are detected either after passing through the sample (ERDA) or after being reflected backward (RBS). It is a non-destructive technique to obtain quantitative information on a film atomic composition and on the evolution of this composition with depth.

The LARN is equipped since 1998 with a linear particle accelerator called ALTAÏS (Accélérateur Linéaire Tandétron pour l'Analyse et l'Implantation des Solides) which allows accelerating heavy ions and can be used to perform IBA on film samples in various configurations.

In our case, atom compositions were obtained through the combination of ERD and RBS. An impinging beam of $^4He^+$ at 3.5 MeV of about 1.5 mm in diameter with a typical current of 10 nA was used, and the samples surface were tilted by an angle of 70° with respect to the incident beam direction. The detectors were placed at 135° (RBS) and 30° (ERD). Square glassy carbon samples of 12 mm width and 3 mm thickness were used for ERD instead of silicon for clearer spectra. The film densities were obtained by comparing the surface mass density (atom count per surface unit) from ERD with the profilometer-measured thickness.

❖ Raman spectroscopy

Raman spectroscopy is a technique to identify the composition and structure of a material by irradiating its surface by monochromatic laser light. The inelastic scattering of the light, after filtering out the unaltered light and performing a spectrum analysis; gives information on the availability of vibrational excitation modes in molecules or phonons in solids and other weak energy transitions of the surface's atoms. This allows characterizing the nature and structure of some materials. This inexpensive and fast method of detection has been made possible by improving filter and spectral analysers to overcome the weakness of the Raman scattering of light compared to other types of scattering.

As for many spectroscopes the procedure for calibration require measuring a known frequency peak. In the case of a-CH a diamond is commonly used, with a characteristic narrow peak at 1332 cm^{-1}. Amorphous hydrogenated carbon structure is composed of covalently bonded carbon and hydrogen atoms. Two types of bonds are commonly found, sp^2 flat bounds like in graphite and sp^3 tetrahedral bonds like in diamond. The sp^2 bonds are forming rings in a-CH like in graphite which have two types of vibration modes named G and D (see Figure 3.13).

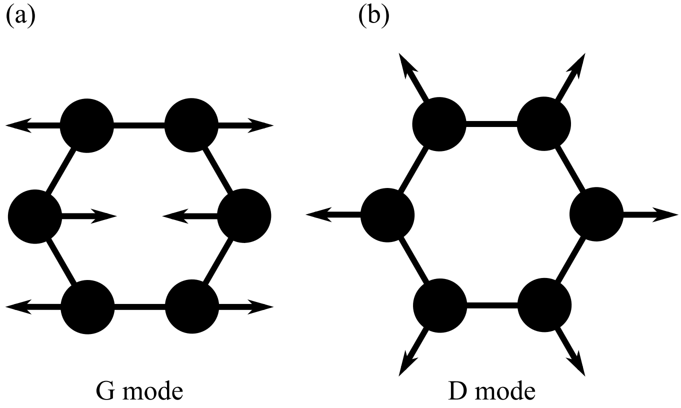

Figure 3.13 Carbon motion in G (a) and D (b) vibration modes of sp2 bounded (graphite-like) rings. Only the D mode is specific to rings and the G mode can be found in carbon chains too.

The G and D mode create photon with mean wavelength of around 1355 cm^{-1}, and 1581 cm^{-1} respectively, but many resonances and other effects makes the measured peaks quite wide and interlacing

Chapter 4 *Simulation of the plasma phase (Article 1)*

A mixed PVD/PECVD deposition process of DLC films with acetylene precursor and graphite magnetron target was simulated using a 3D Particle-in-Cell Monte-Carlo (PIC-MC) code. The simulation comprises of a carefully chosen, self-contained plasma chemistry scheme involving 18 species and 150 reactions, and a dynamic deposition model that includes ion subplantation and the creation of dangling bonds. Mass spectroscopic measurements of neutrals and ions have been performed at substrate position to validate the simulation's predictions. Despite the difficulty in performing reliable mass spectrometry in reactive plasmas and the impossibility of running PIC-MC simulations with powers and time scales comparable to the experiment, we were able to correlate the simulated and experimental densities with varying discharge powers and acetylene contents. We showed that the relative concentrations vary spatially within the chamber due to differences in species' diffusion, energy, or creation area (plasma or chamber). The power dependence of the hydrocarbon ion densities was linear with similar slopes and relative concentrations in experiments and simulations. This is an indication that our model could be extrapolated to relevant experimental conditions and give quantitative predictions on densities, fluxes, and energies of principal species, which could be used as input for film growth simulations. It can also form the basis for simulation frameworks of deposition processes that involve the decomposition of C_2H_2 *in* *low-pressure plasmas (below 1 Pa) with complex reactor geometries and electromagnetic fields.*

Surface & Coatings Technology 400 (2020) 126195

Contents lists available at ScienceDirect

Surface & Coatings Technology

journal homepage: www.elsevier.com/locate/surfcoat

Experimental and theoretical study of a magnetron DC-PECVD acetylene discharge: Determination of the main species and reactions taking place in the plasma

A. Fauroux[a], C. Vandenabeele[a], A. Pflug[b], S. Lucas[a,*]

[a] Laboratoire d'Analyse par Réactions Nucléaires (LARN), Namur Institute of Structured Matter (NISM), University of Namur, 61 Rue de Bruxelles, 5000 Namur, Belgium
[b] Fraunhofer Institute for Surface Engineering and Thin Films IST, Bienroder Weg 54e, 38108 Braunschweig, Germany

ARTICLE INFO

Keywords:
PIC-MC
Magnetron
C2H2
PECVD
Simulation
Mass spectrometry
DLC

ABSTRACT

A mixed PVD/PECVD deposition process of DLC films with acetylene precursor and graphite magnetron target was simulated using a 3D Particle-in-Cell Monte-Carlo (PIC-MC) code. The simulation comprises of a carefully chosen, self-contained plasma chemistry scheme involving 18 species and 150 reactions, and a dynamic deposition model that includes ion subplantation and the creation of dangling bonds. Mass spectroscopic measurements of neutrals and ions have been performed at substrate position in order to validate the simulation's predictions. Despite the difficulty in performing reliable mass spectrometry in reactive plasmas and the impossibility of running PIC-MC simulations with powers and time scales comparable to the experiment, we were able to correlate the simulated and experimental densities with varying discharge powers and acetylene contents. We showed that the relative concentrations vary spatially within the chamber due to differences in species' diffusion, energy or creation area (plasma or chamber). The power dependence of the hydrocarbon ion densities was linear with similar slopes and relative concentrations in experiments and simulations. This is an indication that our model could be extrapolated to relevant experimental conditions and give quantitative predictions on densities, fluxes and energies of principal species, which could be used as input for film growth simulations. It can also form the basis for simulation frameworks of deposition processes that involve the decomposition of C_2H_2 in low-pressure plasmas (below 1 Pa) with complex reactor geometries and electromagnetic fields.

1. Introduction

Numerical simulation helps to understand the underlying physical mechanisms involved in complex processes and may reduce the need for costly experimental approach of trial and error. This is why the digitalization in the industry calls for representation of each involved production process by its digital twin. Consequently, the development of numerical simulation tools for plasma deposition processes is an ongoing effort of many research groups. For cold plasma systems, the Particle-in-Cell Monte-Carlo (PIC-MC) method has been used to simulate various discharge types [1–7] with the general goal to first compute the density of neutrals and charged particles in the gas phase and second understand or predict the growth of specific coatings.

Among the large variety of coatings, hydrogenated amorphous carbon (a-C:H), a soft form of diamond-like carbon (DLC), are popular among scientists and industrials for their advantageous properties, such as moderate hardness, low friction coefficient, chemical inertness and optical transparency, making them practical for biomedical, tribological and protective applications [8–10]. Nowadays, the development of new deposition methods (like Filtered arc or Catalytic plasma deposition) or new techniques (e.g., High-power impulse magnetron sputtering or HiPIMS) facilitates the production of harder forms of carbon coatings, like tetrahedral amorphous carbon (ta-C), which show improved physical properties compared to softer carbon films [11]. However, the low-pressure plasma deposition in a magnetron reactor with a reactive hydrocarbon precursor such as acetylene remains a popular and flexible method to generate smooth and soft DLC films which relies on combining plasma-enhanced chemical vapor deposition (PECVD) and physical vapor deposition (PVD) [12–14]. It has the advantage to be suitable for industrial upscaling [14] and it is often used in combination with other processes to create more complex film structures like multilayers [8] or doped films [9]. Moreover, this

---

[*] Corresponding author.

E-mail addresses: antoine.fauroux@unamur.be (A. Fauroux), cedric.vandenabeele@unamur.be (C. Vandenabeele), andreas.pflug@ist.fraunhofer.de (A. Pflug), stephane.lucas@unamur.be (S. Lucas).

https://doi.org/10.1016/j.surfcoat.2020.126195
Received 13 April 2020; Received in revised form 11 June 2020; Accepted 10 July 2020

process allows the deposition on more complex substrate shapes by using various techniques like substrate motion, multiple sources, or bias application to produce more homogenous film [26]. These methods can produce a variety of carbon coatings since the film physical properties can be tuned by adjusting the operational parameters. For example, depending on the pressure, films ranging from very smooth to microstructured can be created [13]. An important challenge is to deposit, in a reproducible way, the same homogeneous coatings on different complex substrate geometries. Commonly faced problems include bad film adhesion to substrates that requires the deposition of interfacial layers [15], or high compressive stress and delamination, which can be reduced by adjusting the bias, temperature or film thickness [16–18]. Inhomogeneity on substrates with complex shapes is another common pitfall, and could be reduced via substrate holder motions or the application of variable bias [19]. The flux ratio between the background gas (usually argon) and the hydrocarbon precursor (most often C_2H_2 or CH_4) can also have a big impact on the H and sp3 content of films, which are among the most significant parameters for coating properties [8,14,20]. As seen from these few examples, deposition processes are highly tunable and can become increasingly complex due to the high number of factors impacting the deposited film properties. Moreover, experimental diagnostics give only partial information on particle dynamics and do not allow a clear understanding of these processes. Unfortunately, not many modelling studies exist on this particular a-C:H deposition method from magnetron sputter sources.

There is an abundant literature on similar processes involving pure PECVD with acetylene in different types of reactors and for different applications but they often involve higher pressures. Mao et al. [21] presented a 1D fluid model of an RF discharge in acetylene, including more than 400 reactions and 78 species (containing up to 12 carbon atoms), based on a previous model developed by De Bleecker et al. [22]. Like in most plasma fluid models, they used a two-term Boltzmann equation solver to obtain the electron energy distribution function (EEDF) and Chapman-Enskog theory for neutral transport. Their findings were successfully compared with the mass spectrometry measurements of Deschenaux et al. [23]. They confirmed, as in other studies [13,22], the prominence of $C_{2n}H_x$ species plasmas due to the strength of acetylene triple bonds, and pointed out the role of anions in nanoparticle formation. Ariskin et al. [24] presented a hybrid model, which consists of a 1D fluid model with 146 chemical reactions and many species including 16 cations and 6 anions, of a capacitively coupled radio frequency discharge (CCRF). But instead of a two-term Boltzmann solver, they used a Particle-in-cell Monte-Carlo (PIC-MC) solver to obtain the electron energy distribution function (EEDF). They compared their results with a simpler approach that uses an approximated Maxwellian EEDF, and found a slight difference in densities and energies of charged species. They also showed that a relatively small amount of acetylene can have an important effect on the plasma behavior: the addition of only 5.8% of acetylene to the background gas, composed mainly of argon, lowers the plasma density by a factor of 5, and makes the mixture more electronegative. In another work, Mao et al. [25] used a hybrid model to simulate an inductively coupled plasma reactor for carbon nanotube or nanofiber synthesis from various feed gases, and found that with acetylene, higher decomposition rates and the formation of long neutral and ionic hydrocarbon chains occurred. In the work of Miyagawa et al. [26], a PIC-MC simulation of plasma immersion ion implantation (PIII) in nitrogen and acetylene was presented. In order to study the deposition precursors and their energies, 10 hydrocarbon species were considered ($C_2H_2^+$, $C_2H_2^{2+}$, C_2H^+, CH^+, H^+, C_2H_2, C_2H, CH_2, CH, H). Apart from elastic collisions, the authors considered only direct ionization, dissociative ionization and double-ionization of acetylene and nitrogen. They found that a positive pulse followed by a negative one was the most efficient bias mode for making plasma conformal to their substrate. $C_2H_2^+$ and H were the prominent species, but, as they pointed out, this model might not be sufficient to identify deposition precursors, since no chemical reactions nor sticking coefficients were included. Gordillo-Vázquez et al. [27] developed a space-time averaged kinetic model to study the influence of the pressure and power on the deposition of DLC in an RF reactor within a mixture of Ar/H_2 and 1% of C_2H_2. They found that for high content of argon (95%), the concentration in C_2H, C_2 and C_2^* grows as the pressure decreases. They also found that the electron density is not significantly influenced by the power, but increases with pressure.

Experimental characterization of the plasma chemistry of low-pressure acetylene plasmas is a complex task, due to the great number of possible compounds and high deposition rates. No in-situ experimental studies of the magnetron PECVD in Ar/C_2H_2 itself exist (to authors' best knowledge). However, there are some studies of this process from the perspective of sample characterization [13,14], and some were conducted on other acetylene-containing plasma discharges. For example, Baby et al. [28] did an experimental study on the chemistry of Ar/C_2H_2 mixtures in capacitively and inductively coupled RF plasma (CCP and ICP) using mass spectrometric measurements. It was found that the injection of acetylene had an important impact on the discharge voltage, electron temperature and electron density. The dominant ion species for CCP was $C_2H_2^+$ followed by Ar^+ and $C_4H_3^+$, whereas for ICP the argon ions dominated. This observation stems from the higher density and greater portion of medium energy (3–11 eV) electrons in ICP plasma discharges, which are below the acetylene ionization threshold at 11.4 eV, but can still ionize argon through the Penning ionization process. The main neutral species were H_2, CH, C_2, C_2H, C_2H_2, C_2H_3, C_2H_4, C_4, C_4H, C_4H_2 and C_4H_3. Similarly to Deschenaux et al. [23], Baby et al. did not observe the heavier species seen by De Bleecker et al. [22] and explained that charge transfer with the dominant argon species might lower the probability of chain polymerizations, hence diminishing the number of heavier hydrocarbons. Thiry et al. [14] noticed a substantial pressure-drop in an acetylene containing magnetron discharge, as did Baby et al. [28]. They attributed it to the dissociation of C_2H_2 and the deposition of generated radicals, as this pressure drop was proportional to the acetylene ratio. The ethynyl radical C_2H has been commonly identified as being the most important DLC growth precursor [13,29,30] due to its abundance and high surface loss probability [31]. This radical is also highly reactive with the background C_2H_2. Benedikt [30] showed that in an expanding thermal plasma (ETP), the C_2H density has a second order behavior with respect to the acetylene flow, since as when the C_2H_2 flow becomes important, C_2H have a higher probability of reacting before reaching the substrate, and diacetylene species (e.g., C_4H_2, C_4H and C_4) become dominant. The author also proposed a quasi-1D chemistry model to demonstrate the role of other radicals in the deposition of a-C:H, like C_3 and C_3H, which are said to originate from C_2H_2 collisions with C and CH radicals and have high sticking coefficients.

As demonstrated above, plasma processes with C_2H_2 involve a high number of species and reaction pathways. The aforementioned numerical studies are mainly based on computational fluid dynamics (CFD) and implement rather complex chemical reaction schemes; still, this allows to address only small or lower-dimensional simulation volumes. In case of magnetron sputtering at pressures below 1 Pa, CFD approaches are no longer valid [32,33]. Additionally, magnetron discharges are characteristically non-equilibrium processes; the magnetic plasma confinement and the non-thermal emission characteristics of sputtered species play a significant role in the deposition process, which cannot be studied simply with a fluid or hybrid model [32,33]. Nevertheless, studying a low-pressure process has certain advantages; it greatly simplifies the plasma chemistry and facilitates kinetic simulation approaches like PIC-MC, which are generally more resource-demanding than CFD methods.

The goal of the present study is therefore to simulate a low-pressure magnetron plasma discharge in C_2H_2 in order to predict the main neutral, radical and charged species concentrations. For this purpose, a 3D PIC-MC simulation model including a detailed plasma and surface

Table 1
Physical and numerical parameters of the simulations.

Domain size	100 × 72 × 72	[*mm*]
Input power	0.2 − 1.2	[*W*]
Input power density	$9.8 \times 10^{-5} - 5.9 \times 10^{-5}$	[$W.\ cm^{-2}$]
Temperature	*300*	*[K]*
Species	Ar, Ar^+, C_2H_2, $C_2H_2{}^+$, H, C_2H, C_2H^+, CH, C_2, H_2, C, C_4H_2, C_2H_3, $C_4H_2{}^+$, $C_4H_3{}^+$, $C_2H_3{}^+$	
Pressure	0.6	[*Pa*]
Magnetron radius	25.4	[*mm*]
Magnets remanence	*1.4*	[*T*]
Cell size	0.5 − 1.8	[*mm*]
Arrangement of simulation volume segments	5 × 2 × 2	
Time step width	5×10^{-11}	[*s*]
Maximum physical simulation time, and related computation time	100×10^{-6}, 4×10^5	[*s*]
CPU cores used	21	
Weight factors Ar, C_2H_2	$1 \times 10^{10} \times$ *ratio*	
Weight factors e, Ar^+, $C_2H_2{}^+$	1.4×10^5	
Weight factors for all other species	$6 \times 10^2 - 1.7 \times 10^4$	
Sampling for the power dissipation	1×10^{-7}	[*s*]
Carbon Yield	*0.03*	
Secondary electron emission Yield	*0.11*	

description was set up. The simulations were validated with mass spectrometric measurements made in an experimental reactor in a similar configuration. This is a stepping stone in a longer effort of the authors to create a complete model of the smooth a-C:H deposition process.

The first part of this article describes the experimental setup and the PIC-MC model. The experimental apparatus is described in Section 2.1. The numerical parametrization is described in Section 2.2. The plasma chemistry reactions are listed, and their relative importance discussed in Section 2.3. Subsequently, the surface reactions for the substrate, chamber walls, and target are presented in Section 2.4. Both experimental and numerical results are shown and discussed in Section 3. Finally, main conclusions are summarized in Section 4.

2. Method description

2.1. Experimental setup

For this work, a small-size research reactor already described in [7] was used. The plasma was generated from a DC-powered unbalanced circular magnetron operated in fixed-current mode on a 2 in. graphite target. The pressure was set to 5 mTorr (0.66 Pa) with injection of argon and acetylene behind the cathode. The total mass flow was kept constant during experiments with variable acetylene/argon ratio, keeping a constant total pressure by adjusting the effective pumping speed via a throttle valve. The maximum effective pumping speed with a fully open throttle valve was 70 l s^{-1} as in [7] and the total mass flow was 12, 16 or 20 sccm depending on the experiment. Mass spectrometry measurements of the gas phase were performed using a quadrupole PSM003 mass spectrometer supplied by Hidden Analytical, equipped with a turbo-molecular pump reaching a typical pressure of 10^{-8} mbar and connected to the deposition chamber by a 100 µm in diameter extraction orifice, facing the magnetron target at distance of 10 cm. Mass spectrometry measurements of neutrals were performed in residual gas analysis (RGA) mode and in Secondary-ion mass spectrometry (SIMS) mode for the ions. Neutral species entering the mass spectrometer were ionized inside the spectrometer with a 70 eV electron source to allow their detection. In SIMS mode, the detector was calibrated with a low-power pure argon plasma. In order to compare with PIC-MC simulation which are limited in attainable power, measurements were performed with the plasma ignited at power ranging from as low as 5 W up to 200 W (or, in terms of power density, from 0.25 to 9.87 W cm^{-2}), with the aim of estimating the measurements dependence on power.

2.2. Simulation parameters

A parallelized PIC-MC software running on a Tier-1 cluster and developed at Fraunhofer IST [38,39] was used. In order to keep the computational time reasonable, the chamber geometry was simplified by considering only a magnetron surrounded by a small bounding box, with a grounded substrate located at 80 mm from the target (see Fig. 6). To take advantage of the parallelization, the chamber was cut into several volume segments or “quads”, which are simulated on separate CPUs. To avoid limitations due to too many communications between computing nodes, simulations were kept on single nodes by dividing the simulation volume by 5 in the longitudinal direction and by 2 in both other directions, for a total of 20 quads, or 21 CPUs on the 24 available per nodes. The magnetron, composed of several cylindrical magnets, a metallic yoke, and a graphite target surrounded by a grounded shield, was modelled based on the one used in the experiments. The magnetic field was computed with a boundary element method solver (BEM) from the shape, remanence (1.4 T) and relative permeability (1.05) of the magnets. For a reference, the magnetic field value on the cathode-target surface at the point where the field is tangential to the surface was 0.10 T. The time step in a PIC-MC simulation should be sufficiently small to resolve all relevant physical mechanisms; in particular it should be smaller than the angular frequency of the electron oscillations around the ions. The time step was set to 5×10^{-11} s, as it corresponds to a tenth of the oscillation period for an electron density of 1×10^{15} m^{-3}. Another numerical constraint concerns the cell size, which must remain below 3.4 times the Debye length to properly resolve electrical potential gradients [5,35] which is close to 1 mm in this case. The cell sizes were adapted throughout the chamber (from 0.5 mm to 1.8 mm wide) to keep a more precise sampling close to the target where the particles have high energies. Charged and neutral species are represented with super-particles, which usually comprise a larger number of real particles via a statistical weight factor. Well-chosen weight factors are crucial since a certain amount in the order of 10 particles per cell are needed to give statistically accurate results and allow all collision pathways to happen, while too many particles render the simulation time and the memory consumption impractical. To ignite the plasma, an initial population of charged species (e, Ar^+, and $C_2H_2{}^+$) with a small (1×10^{13} m^{-3}) and uniform density was added. A list of the relevant simulation parameters and statistical weight factors is given in Table 1.

2.3. Plasma chemistry

In all low-pressure plasma sources electrons carry most of the kinetic energy due to their higher mobility, so the most important reactions to consider are the ones between electrons and the background gases. Since acetylene is used in many applications (fusion, thin film deposition, combustion, astrophysics, bio-medicine), an extensive number of measured and calculated cross sections are available. According to our best knowledge, the latest and most complete review of cross-sections of electron-acetylene collisions is given by Song et al. [36]. Collisions for many other hydrocarbons are also available in the article of Janev and Reiter [37], but they lack precision at low energies as they are based on experiments and theoretical calculations for fusion research. For elastic collisions between molecules, the variable soft sphere model was used with parameters taken from [38], and for elastic collisions between electrons and acetylene, which exhibit a resonance around 2.5 eV, the recommended cross sections from [36] were used.

Electron impact ionizations (EII) and Dissociative Ionizations (DI) collisions are the main source of ions for molecular precursors like acetylene, as the electrons carry most of the energy and the pressure is too low for the stepwise ionization to occur. The DI reactions are approximatively 10 times less probable than the EII, but they are important to include because they are the main producer of new reactive species. Acetylene does not naturally react with the substrates at low temperature. Hence, to deposit thin a-C:H films, it first needs to be dissociated in more reactive hydrocarbon species. Dissociative excitation (DE) and dissociative recombination (DR) are two other sources for reactive species. DE is similar to DI in terms of cross sections and products for acetylene, but it does not produce charged species. DR is an electron-ion recombination followed by a dissociation (e.g. $C_2H_2{}^+ + e \rightarrow C_2H + H$), which is a fast reaction with no energy threshold, due to the Coulomb attraction between reactants and the possibility for the excess energy to be distributed among the products. Mul and McGowan [39] have provided cross sections for the dissociative recombination of electrons with $C_2{}^+$, C_2H^+, $C_2H_2{}^+$ and $C_2H_3{}^+$. The cross sections for DR reactions with hydrocarbons are weakly dependent on the species, inversely proportional to the electron energy, and really high for low energies (10^{-13}–10^{-14} cm^2). DR has higher probability to occur if ions are present in sufficient amounts and electrons have low energies. As we will show later, these are conditions that occur in magnetron discharges away from the plasma bulk. Since the computational limitations of the PIC-MC simulation are related to the absolute collision rate rather than to the number of possible reactions, all the DI, DE and DR reactions for C_2H_2 and C_2H were included.

Electrons can lose energy by inducing excitation of gas species upon impacts in excited states. This energy can be stored as electronic, vibrational, or rotational excitation. The stored electronic excitation energy can sometimes be released by photon emission with a precise wavelength. Several such excitations, followed immediately by photon de-excitation, were included for acetylene with fitted cross sections given in [40]. Vibrationally and rotationally excited states are usually responsible for the major part of energy exchange between electrons and molecules [30] in plasma reactors like ETP. In cold plasmas, if the vibrational-translational relaxation is slow, the vibrational temperature can become much higher than the gas temperature. For example, temperatures of $T_{rot} = 1190$ K and $T_{vib} = 1940$ K were measured in an ETP plasma with argon and acetylene as precursors, by cavity ring down spectroscopy [41]. Acetylene has five main vibrational excitation energy levels with high cross sections at low energies between 0.1 and 10 eV. The effect of vibrationally excited molecules is the increase of gas temperature, and it might have some effect on the electron temperature in the discharge. However, since accounting for the vibrational states in the simulations would turn out to be really costly in terms of memory usage, and since vibrational-translational collisions cross sections are not available in literature but they must however be slow at low pressure, the vibrational excitations were not included in the model. For rotational excitation, the only data available is from the ab initio theoretical calculation of Thirumalai et al. [42], which provides the cross sections for several energy level transitions for collisions at 10 eV. The reason for this lack of experimental data is the high symmetry of acetylene, which makes those cross sections small and difficult to measure. For these reasons, rotational excitations were also not included in the model.

Argon is notorious for having metastable states [28,43], and can stay excited longer and therefore have higher probability of being able to interact with other particles. Moreover, excited argon can ionize other molecules through the Penning process [44]. For this reason, metastable argon is an interesting species to study in various simulations or experiments involving a C_2H_2/Ar mixture. As reported by Gordillo-Vázquez et al. [45] the reaction $Ar^*(n = 2, {}^3P_{0,2}) + C_2H_2 \rightarrow C_2H_2{}^+ + Ar + e$ has a high rate of 3.5×10^{-10} $cm^3\,s^{-1}$. However, the Penning ionization process involves the collision of three reactants, and an ionization through collisions with metastable argons consists of a chain of collisions. This makes these two processes less probable at low pressure, and thus they were not included.

As discussed earlier, Mao et al. [21] demonstrated the importance of anions for the nanoparticle formation and included them with success in their model. Anions are easily trapped in RF plasma discharges and react more than positive ions. However, since the magnetron mixed PVD/PECVD is a DC discharge, anions will be accelerated towards the substrate, hence anion trapping should not occur. As acetylene and electrons are the main reactants, the most probable source of anions in our case is dissociative electron attachments (DEA) [36]. These reactions are enhanced and exothermic due to the Coulomb attraction, but their resonant character means that they can be caused only by electrons with the right energies. In this work, those reactions were included without their products in order to verify their relative importance without adding complexity.

The first order reactions between energetic electrons and the background gas create ions and several highly reactive radicals that can latter react in fast and sometimes exothermic reactions. In fact, mass spectrometric measurements reveal important concentrations of C_4H_y species as it will be shown in the experimental section (Fig. 1 and Fig. 2), the presence of which can only be explained by secondary reactions. The computational cost of incorporating more species to a PIC-MC simulation is high because a sufficient amount of all the species in all the cells is required so that statistically accurate results could be obtained. Fortunately, in the case of acetylene, the subset of species generated from secondary reactions is restrained by the fact that the acetylene triple bond is hard to break. It was therefore possible to include most of the reactions between the species generated in first order reactions in our model, with more than 150 reactions for only 18 species. The complete list of reactions incorporated in the model is displayed in Tables 2 and 3 along with typical reaction rates from one simulation.

2.4. Surface reactions

The surfaces in the numerical model are the target, substrate and chamber walls, delimiting the simulation boundaries (see Fig. 6). This simulation box is a subsection of the whole experimental chamber. While the poles of the power supply are connected to the target and substrate, the surrounding box is set on floating potential, which has a similar effect as a buildup of a space charge in a larger volume. The box acts as a perfect pump for all generated species and as a pressure-controlled source for the two process gases, effectively maintaining a constant pressure in the volume by reinjecting Ar and C_2H_2 molecules with ratios corresponding to their initial partial pressure ratio. The model of a pressure-controlled source acts as an interface between an infinitely large chamber with homogenous gas composition and the simulation volume, which contains the plasma and many species that diffuse only outward. It was shown by changing the box size that this

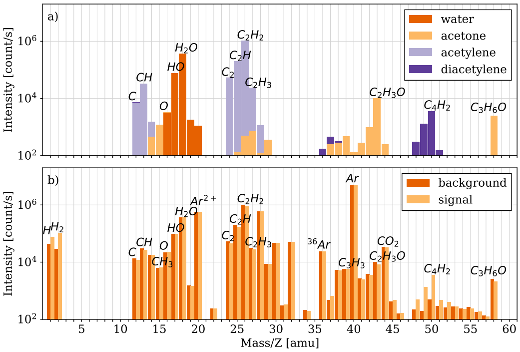

Fig. 1. (Top (a)) Mass spectrum generated from cracking pattern taken from the NIST database [54]. Each pattern was scaled relatively to the backgound level of its main peak in the spectrum below. (Bottom (b)) Mass spectrum in RGA mode with the plasma on (signal) and off (background) at 0.02 A, 0.66 Pa and 10 cm from the cathode with a ratio of 20% C_2H_2 in logarithmic scale. Some possible species attributions are shown above prominent peaks.

assumption was justified and the bounding box size was considered to have only a minor impact on species concentrations. For the grounded substrate, we developed a film growth model in order to study the film deposition and its effect on species concentrations in the surface vicinity. This model is based on complex amorphous carbon growth models described in literature [8,46–50], and it includes the growth by subplantation of ions and the growth due to the radicals sticking to the dangling bonds at the amorphous hydrogenated carbon film surface. The sticking probability of hydrocarbon radicals is generally lower than 1 and is dependent on the surface state [46,49,50]. In particular, it depends on the availability of dangling bond sites (not terminated by hydrogen bonds) on the surface of the growing a-C:H film. In this model, we included surface state dependence by declaring two types of surface sites, each with specific reactions: high sticking coefficients for radicals on dangling bond and small ones on H-terminated sites, H removal from ions impact, surface bonded hydrogen desorption from reaction with H or C_2H, as well as the fast H absorption reaction on free sites. Some radicals, like the atomic carbon created by target sputtering, have a high sticking probability even on H-terminated sites due to the availability of more than one valence electron. Another important way of creating dangling bonds is by ion impact, and a yield of one surface hydrogen atom by ion impact was assumed. The complete set of plasma chemical and surface reactions onto the substrate is given in Table 4.

The target surface had to have a different surface model due to the incoming energetic flux of ions. To simplify the simulation, target poisoning was not considered. Hence, to compare the simulation with experiments, we had to stay in the regime of reduced deposition on target compared to target sputtering, or keep plasma ignited for only short periods of time and perform etching between each measurement. With these precautions, it was assumed that the target remains pure graphite. The sputtering of carbon atoms was defined with a 0.03 yield for all ions impinging the target. This yield value comes from SRIM simulations [51] with argon ions impinging a graphite target at 200 eV with normal incidence. This energy was chosen based on typical discharge voltage at these low power densities. With the price of added complexity, different yields for each ion as well as energy and angular dependence could have been used. However, this is a reasonable approximation since Ar^+ is the dominant ionic species in most cases and the discharge voltage does not vary significantly. The sputtered particles energy follows a Thompson distribution [52] defined by a 7.41 eV

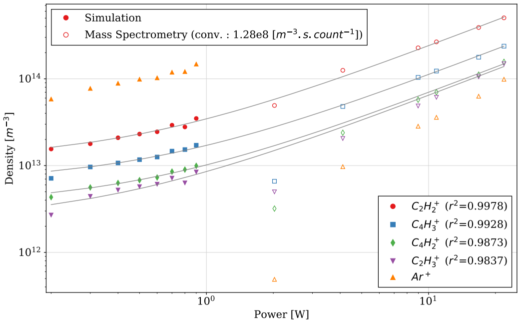

Fig. 2. Main ion intensities from mass spectrometry (empty marker), compared with simulated ion densities in front of the substrate (filled marker) for different currents. Both point sets correspond to a fixed ratio of 20% acetylene. The grey lines show linear fit applied to experimental and simulated values together (determination factors r^2 are shown in the legend). The spectrometer intensities in count s^{-1} where converted to densities by multiplying by an arbitrary conversion factor (1.28×10^8 [m^{-3} s count^{-1}]) chosen to give the best overall fits.

Table 2
Collisions involving electrons included in the model and their averaged rates between 30 and 40μs in the overall chamber for the S_1 simulation.

Reaction	Name	Rate $[m^{-3}\,s^{-1}]$
$e + Ar \rightarrow 2\,e + Ar^{+}$	Ionization	2.09×10^{19}
$e + Ar \rightarrow e + Ar^{*}$	Total excitation	2.01×10^{19}
$e + C_2H_2 \rightarrow 2\,e + {C_2H_2}^{+}$	Ionization	9.18×10^{18}
$e + C_2H_2 \rightarrow C_2H + H + e$	Dissociative excitation	3.72×10^{18}
$e + C_2H_2 \rightarrow 2\,e + C_2H^{+} + H$	Dissociative ionization	1.36×10^{18}
$e + C_2H_2 \rightarrow C_2 + H_2 + e$	Dissociative excitation	9.59×10^{17}
$e + C_2H_2 \rightarrow C + CH_2 + e$	Dissociative excitation	4.49×10^{17}
$e + C_2H_2 \rightarrow C_2 + 2\,H + e$	Dissociative excitation	3.17×10^{17}
$e + C_2H_2 \rightarrow 2\,CH + e$	Dissociative excitation	3.08×10^{17}
$e + {C_4H_2}^{+} \rightarrow C_4H + H$	Dissociative recombination	3.06×10^{17}
$e + C_2H_2 \rightarrow 2\,e + CH^{+} + CH$	Dissociative ionization	2.56×10^{17}
$e + C_2H_2 \rightarrow 2\,e + {C_2}^{+} + H_2$	Dissociative ionization	2.43×10^{17}
$e + C_2H_2 \rightarrow 2\,e + H^{+} + C_2H$	Dissociative ionization	2.34×10^{17}
$e + {C_4H_3}^{+} \rightarrow C_4H + H_2$	Dissociative recombination	1.88×10^{17}
$e + {C_4H_3}^{+} \rightarrow C_4H_2 + H$	Dissociative recombination	1.88×10^{17}
$e + C_2H_2 \rightarrow 2\,e + C^{+} + CH_2$	Dissociative ionization	1.07×10^{17}
$e + {C_4H_2}^{+} \rightarrow 2\,C_2H$	Dissociative recombination	1.03×10^{17}
$e + C_2H_2 \rightarrow e + {C_2H_2}^{*}$	Electronic excitations (sum)	1.07×10^{17}
$e + C_2H \rightarrow 2\,e + C_2H^{+}$	Ionization	4.44×10^{15}
$e + C_2H \rightarrow C_2 + H + e$	Dissociative excitation	1.42×10^{15}
$e + C_2H_2 \rightarrow C_2H^{-} + H$	Electron attachment	1.13×10^{15}
$e + {C_2H_2}^{+} \rightarrow C_2H + H$	Dissociative recombination	9.53×10^{14}
$e + C_2H_2 \rightarrow H^{-} + C_2H$	Electron attachment	6.17×10^{14}
$e + H_2 \rightarrow e + {H_2}^{*}$	Excitations (sum)	1.63×10^{15}
$e + {C_2H_2}^{+} \rightarrow C_2 + 2\,H$	Dissociative recombination	5.65×10^{14}
$e + {C_2H_2}^{+} \rightarrow 2\,CH$	Dissociative recombination	3.20×10^{14}
$e + C_2H \rightarrow C + CH + e$	Dissociative excitation	3.09×10^{14}
$e + C_2H \rightarrow 2\,e + {C_2}^{+} + H$	Dissociative ionization	3.08×10^{14}
$e + H_2 \rightarrow 2\,e + {H_2}^{+}$	Ionization	1.64×10^{14}
$e + C_2H_2 \rightarrow {C_2}^{-} + H_2$	Electron attachment	1.23×10^{14}
$e + C_2H^{+} \rightarrow C_2 + H$	Dissociative recombination	9.23×10^{13}
$e + C_2H^{+} \rightarrow CH + C$	Dissociative recombination	7.45×10^{13}
$e + C_2H \rightarrow 2\,e + C_2 + H^{+}$	Dissociative ionization	7.01×10^{13}
$e + C_2H \rightarrow 2\,e + CH^{+} + C$	Dissociative ionization	6.66×10^{13}
$e + C_2H \rightarrow 2\,e + C^{+} + CH$	Dissociative ionization	5.61×10^{13}
$e + C_2H^{+} \rightarrow 2\,C + H$	Dissociative recombination	3.60×10^{13}
$e + H_2 \rightarrow e + 2\,H$	Dissociative excitation	2.84×10^{13}

Table 3
Collisions that does not involve electrons included in the model and their averaged rates between 30 and 40μs in the overall chamber for the simulation S_1.

Reaction	Rate $[m^{-3}\,s^{-1}]$
$Ar^{+} + Ar \rightarrow \text{slow } Ar^{+} + Ar$	5.42×10^{18}
$H + C_2H_2 \rightarrow C_2H_3$	1.91×10^{18}
$C_2H_2 + Ar^{+} + \rightarrow Ar + {C_2H_2}^{+}$	8.30×10^{17}
$C_2H_2 + C_2H \rightarrow C_4H_2 + H$	6.06×10^{17}
${C_2H_2}^{+} + C_2H_2 \rightarrow {C_4H_3}^{+} + H$	4.85×10^{17}
${C_2H_2}^{+} + C_2H_2 \rightarrow {C_2H_3}^{+} + C_2H$	4.25×10^{17}
${C_2H_2}^{+} + C_2H_2 \rightarrow {C_4H_2}^{+} + H_2$	2.61×10^{17}
$C_2H_2 + C_2 \rightarrow C_4H + H$	2.15×10^{17}
${C_2H_3}^{+} + C_2H_2 \rightarrow {C_4H_3}^{+} + H_2$	1.52×10^{16}
$H + C_2H \rightarrow C_2H_2$	5.43×10^{14}
${C_2H_2}^{+} + C_2H \rightarrow {C_4H_2}^{+} + H$	9.47×10^{13}
$H_2 + H \rightarrow H + H_2$	6.10×10^{13}
${C_4H_3}^{+} + C_2H \rightarrow {C_6H_3}^{+} + H$	2.14×10^{13}
$H + CH \rightarrow C + H_2$	1.47×10^{13}
${C_4H_2}^{+} + C_2H \rightarrow {C_6H_2}^{+} + H$	1.42×10^{13}
$H + C_2H_3 \rightarrow C_2H_2 + H_2$	1.42×10^{13}
$C_4H_2 + {C_2H_2}^{+} \rightarrow {C_4H_2}^{+} + C_2H_2$	1.23×10^{13}
$C_4H_2 + C_2 \rightarrow C_6H + H$	1.23×10^{13}
$C_4H_2 + C_2H \rightarrow C_6H_3$	1.10×10^{13}
$C_2H_3 + C_2H \rightarrow 2\,C_2H_2$	7.89×10^{12}
$H_2 + C_2H^{+} \rightarrow {C_2H_2}^{+} + H$	4.21×10^{12}
${C_2H_2}^{+} + C \rightarrow C_3H^{+} + H$	2.10×10^{12}
$C_2H_3 + {C_2H_2}^{+} \rightarrow {C_4H_3}^{+} + H_2$	2.10×10^{12}
$C_2H + C \rightarrow C_3 + H$	1.58×10^{12}
$H + {C_4H_2}^{+} \rightarrow {C_4H_3}^{+} + H$	9.82×10^{11}
${C_4H_2}^{+} + C_4H_2 \rightarrow {C_6H_2}^{+} + C_2H_2$	8.77×10^{11}
$C_4H_2 + {C_2H_2}^{+} \rightarrow {C_4H_2}^{+} + C_2H_2$	8.77×10^{11}
$C_4H_2 + C \rightarrow C_5H + H$	5.26×10^{11}
${C_2H_3}^{+} + C_2H \rightarrow {C_4H_3}^{+} + H$	4.21×10^{11}
$C_2H^{+} + C \rightarrow {C_3}^{+} + H$	3.79×10^{11}
${C_2H_3}^{+} + C_2H \rightarrow {C_2H_2}^{+} + C_2H_2$	3.79×10^{11}
${C_2H_3}^{+} + C_2H \rightarrow {C_4H_2}^{+} + H_2$	1.75×10^{10}
$H + {C_2H_3}^{+} \rightarrow {C_2H_2}^{+} + H_2$	0
${C_4H_3}^{+} + C \rightarrow {C_5H_2}^{+} + H$	0
${C_4H_2}^{+} + C \rightarrow C_5H^{+} + H$	0
$H + {C_4H_3}^{+} \rightarrow {C_4H_4}^{+} + H$	0
${C_4H_3}^{+} + C_4H_2 \rightarrow {C_8H_5}^{+} + H$	0
${C_4H_2}^{+} + C \rightarrow {C_5}^{+} + H_2$	0
${C_4H_3}^{+} + C_4H_2 \rightarrow {C_6H_3}^{+} + C_2H_2$	0
${C_4H_3}^{+} + C \rightarrow C_5H^{+} + H_2$	0
$H_2 + C_2H \rightarrow C_2H_2 + H$	0
$H + C_4H_2 \rightarrow C_4H_3$	0
$C_2H_3 + {C_2H_2}^{+} \rightarrow {C_2H_3}^{+} + C_2H_2$	0
$H_2 + {C_2H_2}^{+} \rightarrow {C_2H_3}^{+} + H$	0
${C_4H_2}^{+} + C_4H_2 \rightarrow {C_8H_4}^{+} + H$	0
${C_4H_2}^{+} + C_4H_2 \rightarrow {C_8H_3}^{+} + H$	0
$H_2 + H \rightarrow H + H_2$	0
$C_4H_2 + C_2H \rightarrow C_6H_2 + H$	0
$H_2 + H \rightarrow H + H_2$	0
$CH + C \rightarrow C_2 + H$	0

binding energy. The SRIM calculations showed that ion backscattering is a rare event, so ions are set to be implanted upon impact. However, in order to avoid creating an artificial pressure gradient, the ${C_2H_2}^{+}$ and Ar^{+} were set to recombine on the target surface and be released with thermal energy. Upon impact, ions are known to yield secondary emitted electrons (SEE), which is an important mechanism sustaining plasma in magnetrons. The SEE yield was set to 0.11, and electron energies were chosen randomly from a uniform distribution within an energy interval of 0 to 10 eV. These values are standard for metallic targets, but they are unknown for a graphite target (to the authors' knowledge), and graphite probably has a lower SEE yield. According to Depla et al. [53], the SEE yield is reciprocal to the discharge voltage for a given current. The main impact of a higher discharge voltage would be to increase the energy of ions impinging the substrate, which would in turn slightly increase the electron and carbon yield. The energy gained by electrons traversing the sheath would also rise, which might affect the position of the sheath, as well as the electronic temperature in the plasma bulk [53].

3. Results

3.1. Experimental results

Mass spectrometry measurements were conducted on an argon-acetylene plasma for several flux ratios and imposed currents. To avoid possible bias due to the target pollution, measurements were limited to low powers and short times. Also, before most experiments, the target was etched with a plasma in pure argon at 0.66 Pa and 50 W for several minutes. Fig. 1b shows a typical residual gas analysis (RGA) spectrum obtained with 20% C_2H_2 at 0.02 A and 0.66 Pa. The acetylene ratio is defined as:

$$r = \frac{F_{C_2H_2}}{F_{Ar} + F_{C_2H_2}}, \tag{1}$$

where F_{Ar} and F_{C2H2} are the argon and acetylene injected flows. Several known cracking patterns (CPs) [54] are depicted in Fig. 1a to help the injected species and pollutants identification. The peaks associated with water vapor (16, 17, and 18 u), and with carbon monoxide (or nitrogen) and carbon dioxide (28, 44 u) were present even before any gas injection, and remained mostly unchanged for all pressures. Therefore, they probably resulted from the presence of residual gases in the chamber and detector. Many peaks can be attributed to acetone, which is used as an acetylene solvent and was present as impurity in the C_2H_2 bottle. Most peaks were unchanged after the plasma ignition (see Fig. 1b). The only changes are the lower intensity of acetylene and

Table 4
Surface reactions included in the model.

Surface before	Surface after	Impinging species	Released species	Probability
a-C	a-C:H	*H*	–	0.9
a-C:H	a-C	*H*	H_2	0.1
any	a-C	C_2	–	1
any	a-C	*C*	–	1
any	a-C:H	*CH*	–	1
a-C	a-C:H	C_2H	–	1
a-C	a-C:H	C_4H_2	–	1
a-C	a-C:H	C_4H_3	–	1
a-C	a-C:H	C_2H_3	–	1
a-C:H	a-C	C_2H	C_2H_2	0.1
a-C:H	a-C	*ions*	*H*	0.1
a-C:H	a-C:H	*ions*	–	0.9
any	any	Ar^+	*Ar, e*	1
any	any	*e*	–	1

acetone related peaks (26 and 58 u), and the higher intensity of hydrogen (1 u), dihydrogen (2 u) and diacetylene peaks (48, 49 and 50 u). Similar RGA measurements were conducted by increasing the power up to 200 W, and no additional peaks were found up to mass 60 u.

All peaks originating from the cracking of the acetylene and acetone molecules receded with plasma ignition, which indicates that the C_2H_2 and C_3H_6O molecules were consumed inside the plasma phase. It was found that subtracting the CPs relative peak intensities from both plasma-on and plasma-off spectrums as in [55] did not reveal remaining concentrations of those product species with more than 1×10^2–1×10^3 count s^{-1}. Some technics could have been used for circumventing these limitations, e.g., the use of triple differential pumping or Bayesian analysis (see for example [56]). However due to these low intensities and the fact that some peaks are common between the C_2H_2 and C_3H_6O molecules, it was impossible to extract reliable information on the generation of reactive dissociation products like C_2H.

It is clear that the decrease of the acetylene peaks (-1.4×10^5 count s^{-1}) cannot be counterbalanced by the increase of any other peaks ($< 3.4 \times 10^4$ count s^{-1}), even considering possible calibration error or sensitivity bias. This means that acetylene concentration in the chamber diminished significantly. This decrease has to be attributed to loss by ionization or loss by dissociation. Fig. 2 presents the main positive ions peaks (empty marker) for 20% acetylene and varying power, and shows that the main cations were singly-ionized acetylene, with other prominent ionic species being $C_4H_3^+$, $C_4H_2^+$, Ar^+ and $C_2H_3^+$. Interestingly, the relative peak intensities remained similar for all powers and their absolute values increased linearly with increasing power, this is probably due to the linear increase of the electron density with power as further explained in the simulation section. However, the measurements done at the lowest power (2 W) had a much lower intensity and reduced the linear fits quality. This is probably due to cathode pollution, which creates instability in plasma at such low powers, because the carbonated redeposited layer is dielectric and is not etched fast enough. The measured ion peak intensities were fitted together with the simulated densities, with the commonly made assumption that a quadrupole mass spectrometer gives intensities that are proportional to densities [56]. A common spectrometric intensity-to-density conversion factor for all species with value 1.28×10^8 m^{-3} s count^{-1} was chosen to get the best overall fits between the simulation and experimental lines for hydrocarbons. A good match was observed between simulated and experimentally observed slopes and relative densities for all hydrocarbon ions. However, the Ar^+ density and its spectrometric intensities differed a lot. The origin of that discrepancy is unclear, but it seems that it could be linked to the slight difference of pressure between the simulation and the experiment (see Fig. 5 and related discussion below). If the mass spectrometer response for each species was absolutely calibrated or if individual conversion factor were used, the argon ion intensity might be in fact in accordance with its simulated density. However, in the absence of absolute calibration choosing to have only one conversion factor for all spectral lines reduces the number of fitted parameters from 11 parameters in the first case to 15 in the latter.

The RGA measurements with a varying Ar/C_2H_2 ratio and fixed current are summarized in Fig. 3 next to corresponding neutral densities from simulations. The main peak intensities were obtained by subtracting the average values of every peak during the plasma-on and plasma-off phases for each Ar/C_2H_2 ratio at constant initial pressure and pumping speed. This subtraction reveals only the peaks whose intensity increased, hence it is possible that other neutral species were present in the chamber in abundance but masked by the cracking of acetylene and acetone in the detector as discussed above. The main peaks (threshold of 4000 count s^{-1}) were for H, H_2, C_4H_2, C_4H, and C_4H_4. According to [54], the cracking pattern for H_2 contains a peak at mass 1 u which corresponds to only 2% of the main peak; it therefore cannot explain the observed amount of atomic hydrogen observed (roughly 50% of H_2 intensity), so atomic hydrogen must be present in the chamber in the spectrometer vicinity. The main neutral species were in order of importance H_2, H and C_4H_2, whereas in the simulation they were C_2H, H, H_2 and C_4H_2. This discrepancy might stem from the short simulation times as explained further in the discussion. However, all measured peak intensities and simulated densities increased linearly

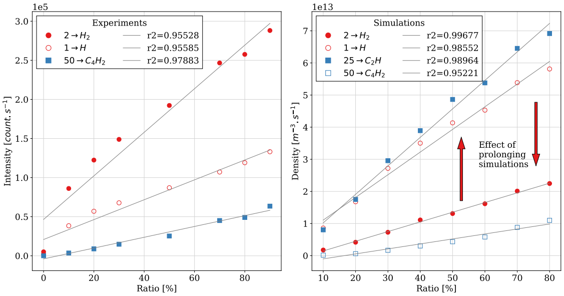

Fig. 3. (Left) Intensity difference ($I_{plasma\ on} - I_{plasma\ off}$) of main RGA mass spectrometric peaks at 0.02 A, 0.66 Pa, and 10 cm from the cathode with varying acetylene ratio. (Right) Simulation S_1 main radicals' densities after 16 μs for different acetylene ratios. The arrows represent the expected relative evolution of concentrations as the reactive H and C_2H get consumed in reactions producing C_4H_2 and H_2.

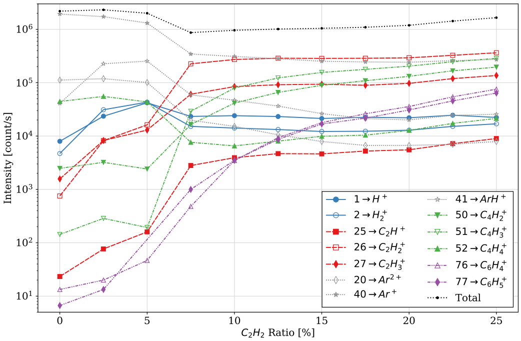

Fig. 4. Main ions intensities from mass spectrometry plotted against the acetylene ratio for a fixed current set at 0.016A with a distance of 18 cm between the mass spectrometer and the magnetron.

with acetylene content which is a sign that the origin of the observed species must be, as in the simulations, linked to the electron dissociations of acetylene hence proportional to the electron and the acetylene density.

The main positive ion peaks were measured in SIMS mode with a varying Ar/C_2H_2 ratio at 16 mA, and the resulting points are shown in Fig. 4. Since the detection of ions with a MS facing an unbalanced magnetron can saturate the detector, the distance between the MS and the magnetron were set to 18 cm instead of the 10 cm used for other experiments. At low acetylene content Ar, Ar^{2+} and ArH^+ where the dominant ionic species, but after only 12.5% acetylene, $C_2H_2{}^+$ became the dominant species. We observed a decrease of argon related ions intensities for increasing ratios, and an increase of all hydrocarbon ions intensities. The total ion intensity decreased initially with acetylene injection but then increased after a ratio of 7.5% acetylene, following the general increase of hydrocarbon ions. The main hydrocarbon ions were $C_2H_{2,3}{}^+$, $C_4H_{2,3,4}{}^+$, and $C_6H_{4,5}{}^+$, which all contained pair number of carbon atoms. Interestingly, this increase in intensity depended on ions' number of carbon atoms, with a small increasing rate for $C_2H_{2,3}{}^+$ a bigger one for $C_4H_{2,3,4}{}^+$, and an even steeper increase for $C_6H_{4,5}{}^+$. The initial decrease of total ion density, probably associated with a similar decrease in electronic density, could be attributed to several causes, for example: acetylene low ionization threshold and large cross-section compared to argon, cathode pollution, pressure variations. Indeed, while the initial pressure was kept constant at 5 mTorr before plasma ignition, the pressure systematically dropped when the plasma was ignited and when acetylene was present. This phenomenon is due to the fact that reactive species condensation on the chamber walls affects the total pressure more than the competing effect of acetylene splitting in the plasma, as shown by D. Thiry et al. [14].

Fig. 5 presents the intensity of main ion peaks for different initial pressures with a 4% ratio of acetylene and a current set to 100 mA. It suggests that the pressure had indeed a big impact on the measured ion peaks: for a small pressure variation of around 3 mTorr (or 0.133 Pa), a variation of more than one order of magnitude of the intensities is observed. One possible explanation of this phenomenon is that at higher pressure, ions have more probability to recombine with low energy electrons, or to react with acetylene creating new ionic species, thus diminishing the number of $C_2H_2{}^+$ and Ar^+ ions reaching the detector. The pressure change could also have an impact on the electron mean free path, reducing their energy and hence reducing the electronic temperature and ionization rate. Interestingly, Fig. 5 shows that $C_2H_2{}^+$ is promoted for high pressures and its concentration raises above that of Ar^+, even though acetylene represents only 4% of the background gas, which means that either acetylene gets ionized easier than argon or charge transfer reactions tend to promote acetylene ions over argon ones.

3.2. Simulation results

Several simulations were run with power setpoints ranging from 0.1 to 1.0 W (5×10^{-3} to 5×10^{-2} W cm^{-2}), and relative concentrations of argon and acetylene ranging from 0% to 90%, defined as:

$$r = \frac{P_{C_2H_2}}{P_{Ar} + P_{C_2H_2}}, \tag{2}$$

with P_{Ar} and P_{C2H2} being the initial partial pressures of argon and acetylene, respectively. A stable plasma ignition was obtained in all cases, with charge densities ranging from 1×10^{14} to 1×10^{16} m^{-3}, and with a maximum ionization degree of 1×10^{-4}. Typical computation time were as long as 50 h for a physical discharge simulation time of 50 µS. Drifting ionization zones or "spokes" were present on most of the simulations, and can be seen as an asymmetry in Fig. 6. For a typical simulation with a power of 0.8 W and an acetylene ratio of 20% the spoke was rotating in the opposite of the $\overrightarrow{E} \times \overrightarrow{B}$ drift direction with a period of around 30 µs. This phenomenon has been described in recent experimental articles [57] and reproduced with PIC-MC simulations [34]. However, since they were not the primary interest of this study, their effects on densities and other observables were minimized by averaging densities over time and space. The electron energy distribution functions (EEDF) were calculated across the chamber from electrons' velocity distribution and the results were fitted with Maxwellian or Bi-Maxwellian distribution functions. For the plasma bulk, the EEDFs were Bi-Maxwellian with $Te_1 \approx 2$ eV and $Te_2 \approx 10$ eV. This Bi-Maxwellian distribution is a known characteristic distribution for electrons in magnetron plasmas. One population of electrons is made highly energetic by the sheath-target potential difference, and another population resulting from ionization in the plasma bulk has a lower mean energy [32,58]. This feature together with the spokes are often missing from other models (e.g. fluid models) and justify the choice of the PIC-MC approach, as explained in Section 1.

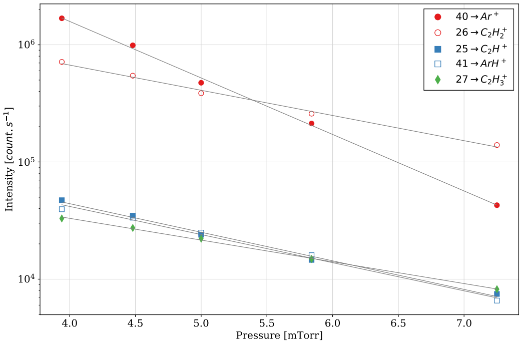

Fig. 5. Intensity of main ions peaks measured with the mass spectrometer vs the total chamber pressure in a discharge with 4% acetylene and a current set at 100 mA.

The simulation with 20% acetylene and 0.8 W has been chosen as an arbitrary representative simulation it will be referred as "S_1" in the following to ease discussion. Densities in this simulation were averaged inside cylindrical, 1 mm-thick slices across all the chamber. The resulting density profiles for each time step of S_1 from 0 to 50 µs are visible in Fig. 7. The equilibrium for charged species was reached faster than for neutrals, as the bulk density of electrons and main ions increased very slowly after 5 µs, whereas C_2H, H, C and CH kept increasing even after 20 µs. For most species, the maximum density was located in the plasma bulk, at the edge of the plasma sheath, around 5 mm away from the cathode. The main species in the bulk were the radicals C_2H and H, which accumulated gradually slower as their concentrations were approaching an equilibrium. The $C_2H_3{}^+$, $C_4H_2{}^+$ and $C_4H_3{}^+$ density profiles had a maximum outside of the plasma bulk because they were mainly produced by recombination of $C_2H_2{}^+$ ions with C_2H_2. The C_2H and H_2 species were distributed more homogenously than the other radicals because they were produced not only in the bulk but also during recombinations in the rest of the chamber. The density profile of C was nearly a straight line for all time steps, with a slope decreasing with the distance from target. This linear profile results from the fact that sputtered carbon atoms have a high kinetic energy, which induces a fast diffusion and a reduced loss of momentum via collisions with the background gas molecules. In addition to differences in longitudinal profiles, species had different lateral profiles: charged species formed a narrow beam throughout the chamber, due to the unbalanced magnetic field configuration, whereas the radicals

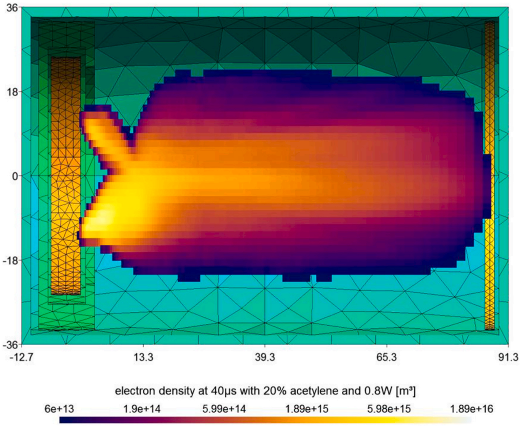

Fig. 6. Vertically clipped view of the electron density after 40 µs in a simulation with 20% acetylene in the 3D meshed chamber used in the simulation. Distances are in mm and density is color coded in m^{-3}. Each colored point corresponds to a simulation cell. Cells with electron density bellow 1×10^{13} m^{-3} were hidden. The bounding box axis is graduated in millimeters.

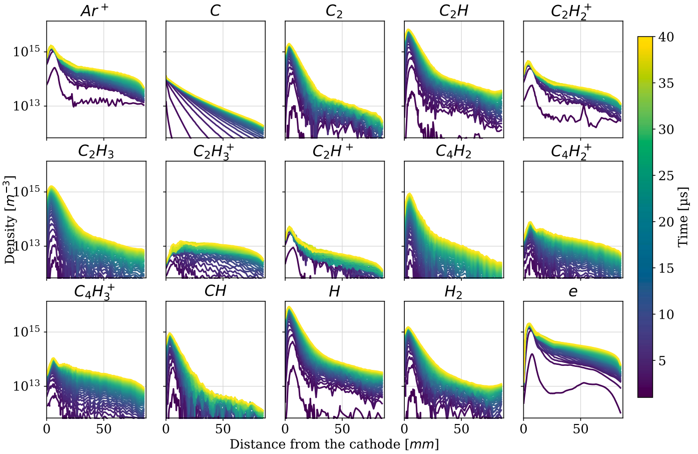

Fig. 7. Mean densities of several species' vs the distance from the cathode surface in millimeters in simulation S_1 (20% acetylene, and 0.8 W). Each curve corresponds to one time-step of 1 µs from 0 (blue) to 40 µs (yellow). (For interpretation of the references to color in this figure legend, the reader is referred to the web version of this article.)

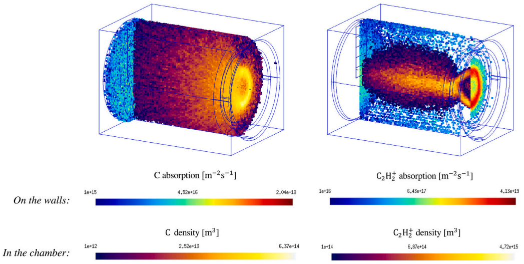

Fig. 8. Carbon and acetylene ion density in the chamber cut with a vertical plane and absorption profiles on the chamber walls in the S_1 simulation after 40 µs.

formed a wider beam because they diffused thermally from the bulk where they were created. The widest diffusion cone was the one of carbon atoms due to simulation's wide angular distribution for sputtered particles. Fig. 8 compares vertical cuts of the densities of C atoms and $C_2H_2^+$ cations and the profile of their respective absorptions onto surfaces. The aforementioned difference in diffusion spread of sputtered atoms and ions can be seen on this figure, as well as the impact it would have in terms homogeneity of the resulting substrate absorption.

Tables 2 and 3 contain all the reactions that were included in our model, as well as the observed reaction rates in S_1, averaged between 30 and 40 µs in the whole simulation volume. From these rates, some conclusions regarding the choice of reactions and species can be made. For example, the main reactions producing new species were indeed the DE and DI reactions, followed by DR ones, as discussed in Section 2.3. The DEA were non-neglectable with rates up to 1×10^{15} m^{-3} s^{-1} for the $e + C_2H_2 \rightarrow C_2H^- + H$ reaction. Adding them could indeed be interesting if, for example, more data on anions could be experimentally obtained, or if anions effects on deposition were to be considered. The fastest reactions not involving electrons were charge transfers and reactions between acetylene and C_2H, H or $C_2H_2^+$. In particular, the dissociative recombination of C_2H_2 and $C_2H_2^+$ was responsible for the production of the majority of the diacetylene species.

Fig. 9 shows a general view, built upon Fig. 7, of the species present in the chamber at a moderate acetylene ratio (i.e., 20%) 40 µs after

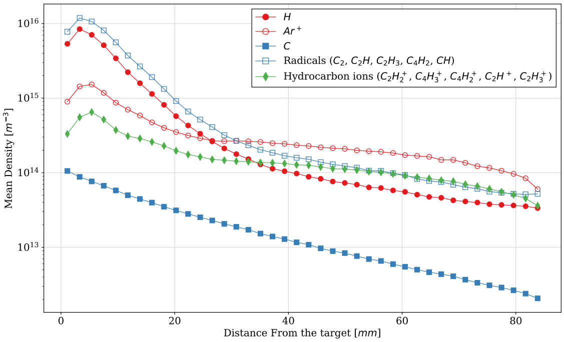

Fig. 9. Mean densities of principal species and species groups as a function of the distance from the cathode [mm] in simulation S_1 (20% acetylene, and 0.8 W) after 40 μs of simulation.

plasma ignition. The sputtered carbon flux was not among the dominant species as it was always two orders of magnitude less concentrated than the other species. Moreover, this difference increases with the distance. This means that the sputtered atoms contribution to deposition decreases relatively to the hydrocarbon ions and radicals' contributions if the substrate is set further away from the cathode. The sputtered carbon atoms did not participate much in the plasma chemistry since the fastest reaction involving C was $C_2H_2{}^+ + C \rightarrow C_3H^+ + H$ with a rate of 1×10^{12} m^{-3} (see Table 3). Since the production of sputtered atoms is proportional to the ions flux towards the cathode which is itself proportional to the electronic density and hence to the power, it would be rather simple to extrapolate the C flux towards the substrate for higher powers. The density profile of radicals was decreasing faster with distance than the one of ions, hence the contribution of radicals to film growth compared to the one of subplanted hydrocarbon ions should also depend on the distance from the target and get less important the further the substrate is set. This is an important result to improve film deposition as it shows that the growth precursor concentrations are non-homogenous in the chamber, and therefore the types of films produced via this deposition method will depend on the location of the substrate.

Fig. 10 shows the densities in the plasma bulk (defined as a cylindrical volume parallel to the target with a 20 mm radius and 20 mm height) for all species included in the simulation after 20 μs, for many simulations differing from S_1 only in power (right) or only in ratio (left). The averaged densities of all produced species inside the bulk evolved linearly with power and remained proportional to the electron density. In terms of ratio, two populations with constant relative concentrations could be distinguished in Fig. 10: the first order species ($C_2H_2{}^+$, C_2H^+, H, C_2, H_2, and CH), which originated mostly in direct reactions between electrons and acetylene, and the second order species ($C_4H_3{}^+$, $C_4H_2{}^+$, $C_2H_3{}^+$, C_2H_3, and C_4H_2), which were primarily generated in collisions between these first order species and the background acetylene (see Table 3). The second population was more sensitive to a change in C_2H_2, and this stems from the fact that the reaction rates depend on the density of both reactants. Hence, while the first order species varied linearly with the C_2H_2 ratio and the power (Fig. 2 and Fig. 10), the second order species varied linearly with power but in a quadratic manner with the acetylene ratio. The mean electron density in the bulk increased also linearly with the ratio of acetylene as can be seen in Fig. 10 and in the following linear regression fits:

$$n_e(ratio) = 2.84193 \times 10^{13} \times ratio + 4.83609 \times 10^{14}[m^{-3}](r^2 = 0.8765),$$
$$n_e(power) = 1.54640 \times 10^{15} \times power + 1.47808 \times 10^{14}[m^{-3}](r^2 = 0.9908), \quad (3)$$

with n_e the electron density. This could be explained by noticing that the lower ionization threshold of acetylene and larger ionization cross-section makes plasma ignition easier in an acetylene rich mixture, and more electrons are generated via ionization for the same power.

3.3. Discussion

In order to compare simulated densities with the mass spectrometric results, the densities were averaged in a cylindrical volume (10 mm height and 20 mm radius) located in front of the substrate in several simulations with parameters similar to S_1, but with different powers or ratios. The results compared with mass spectrometric measurements are shown in Fig. 2, Fig. 3 and Fig. 4. Despite the low power and the short simulation time, the simulated ion densities and the experimental ones were tightly correlated, as can be seen in Fig. 2. Indeed, the main hydrocarbon ions in the simulations were $C_2H_2{}^+$, $C_4H_3{}^+$, $C_4H_2{}^+$, and $C_2H_3{}^+$, respectively, and their densities varied linearly with power with similar relative concentrations. However, the Ar^+ densities were higher than the $C_2H_2{}^+$ one in the simulation, while the spectrometric measurements suggest that it should be the opposite.

Some reactions were more important away from the plasma bulk rather than close to it. For example, the dissociative recombinations have a high probability of occurring at lower energies, meaning they play a significant role far from the target, where the electron temperature remained around 2 eV. Similarly, reactions between ions, molecules and radicals occurred principally away from the plasma where they were generated, and hence the concentrations of the different species evolved differently across the chamber, as seen in Fig. 7. For example, due to the acetylene molecule polarizability, the charge transfer with the argon ion is a fast and even exothermic reaction [60] that will tend to promote the acetylene ions over the argon ones:

$$C_2H_2 + Ar^+ \rightarrow C_2H_2^+ + Ar + 4.86\ eV \quad (4)$$

Indeed, this reaction happened at a very fast rate in the simulations (around 8.3×10^{17} m^{-3} s^{-1}) as seen in Table 3.

The mass spectrometric measurements showed that the ions peaks intensities decrease with pressure, that the $C_2H_2{}^+$ ions get promoted at higher pressure over the Ar^+ ones and that an increased C_2H_2 ratio lead

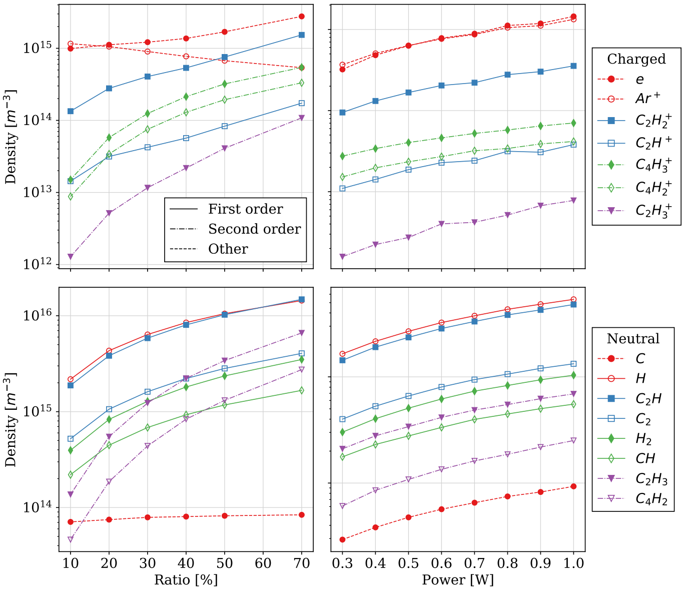

Fig. 10. Mean densities of all charged (Top) and neutral species (Bottom) in the plasma bulk of several simulations after 20 µs, with varying acetylene ratio (Left) and power (Right). The different line types are underlying the similar evolutions of several groups of species: the first order (plain), second order (dot-dashed), and other species (dashed).

to a decreased ion count. All these observations suggest that collisions like charge transfers and ions recombinations which happen on the ions' path towards the substrate (or detector) and that are amplified at higher pressure or higher C_2H_2 ratio are important and could explain for example the discrepancy observed between the simulated and measured Ar^+ density in Fig. 2. Indeed, if the simulation were run for longer times, or if the pressure in the simulation was higher, the charge transfer between Ar^+ and $C_2H_2{}^+$ would have favored $C_2H_2{}^+$ density over Ar^+ ones even more. Nonetheless, the good agreement of the slopes and relative densities of hydrocarbon ions between simulations and experiments in Fig. 2, is a validation of the simulated ions production in the plasma and of the latter reactions in the chamber as the observed hydrocarbon ion species depend on both mechanisms.

The evolution of ions densities with acetylene ratio, presented in Fig. 4 and Fig. 10, showed a good qualitative agreement between simulation and experiments. There were some discrepancies between the two figures, for example the point where the density of $C_2H_2{}^+$ crosses the one of Ar^+ is around 12.5% in the experiment, while it is closer to 50% in the simulations. However, we observed in both cases an increase of hydrocarbon ion densities proportional to the acetylene ratio. In particular, species identified in Fig. 10 as "First-order" and "Second order" are clearly identifiable on Fig. 4. A notable exception to this comparison is the $C_2H_3{}^+$ ions. They seem to follow the evolution of $C_2H_2{}^+$ and C_2H^+ on Fig. 4, placing them in the "First-order" group, even though they clearly belong to the "Second-order" group based on their evolution in the simulations, as seen on Fig. 10. This probably stems from the fact that $C_2H_3{}^+$ is produced mainly via the addition of H to $C_2H_2{}^+$ and, as explained earlier, radical densities did not reach equilibrium during simulations.

Fig. 3 shows the dependence of neutrals densities on the ratio in the simulations and experiments. It shows that the evolutions were still linear in both cases, but the main species in the simulations were C_2H and H whereas, experimentally, C_2H could not be observed, and the H intensity was smaller than that of H_2. However, as Fig. 7 reveals, the non-charged species did not attain an equilibrium and the concentrations of C_2H and H diminished in favor of C_4H_2 species and H_2, as most molecule-molecule reactions incorporated in the model tends to favor C_4H_2 and H_2 species over C_2H and H (see Table 3). As can be seen in Fig. 7, the accumulation of radicals was too slow to stabilize in several microseconds, even in this small chamber, and will require longer simulation times in the range of milliseconds to achieve stability. Some simulations were run for up to several hundred microseconds, but we found that the surface model has a decisive influence on the densities at equilibrium. Since the prime interest of this study was the plasma chemistry and not the deposition model, the simulation time were kept at several tenth microseconds which consequently allowed us to study a wider range of parameters in a realistic timeframe. This had an impact on the predictions given on neutrals' density in front the substrate (see

Fig. 3). However, even the radical seemed to be already at equilibrium in the plasma bulk region (see Fig. 7 and Fig. 10), which means that the "plasma source" would remain as presented, even for longer simulations.

One of the main limitations of the model presented here, common with most PIC-MC simulations, was the low power at which the simulations were run, with a maximum power of 1.2 W attained in this study, far from current applications with typical powers of several hundreds of watts. However, the main effect of a power raise was an increase of the electron density, followed by a proportional increase of all the plasma products (see Fig. 10). This is probably due to the fact that in magnetron reactors, electron density can directly be linked to the discharge power, whereas the electron temperature remains almost constant for a wide range of power [59]. According to [30] reaction rates can be calculated from the following equation:

$$R_{AB} = n_A n_B \iint \left[\overrightarrow{v_{rel}} \sigma_{AB}(v_{rel}) f_A(\overrightarrow{v_A}) f_B(\overrightarrow{v_B}) \right] d\overrightarrow{v_A}\, d\overrightarrow{v_B}, \tag{5}$$

with n_A, $\overrightarrow{v_A}$, and f_A the densities, velocities and density function of reactant A, $\overrightarrow{v_{rel}}$ the relative velocity, and σ_{AB} the cross section of the reaction. For all collisions between electrons and acetylene the only parameter from Eq. (5) that varies with power is the electron density. Hence, the first order reactions' rate, and consequently their products, will remain proportional to the electronic density and increase linearly with power. Therefore, the power scaling of the results should be possible as long as the produced species concentrations remain small with respect to the background gas. This is only true for low ionization degree.

4. Conclusions

The magnetron DC discharge with a graphite target in a mixture of acetylene and argon was simulated with a PIC-MC model and compared with mass spectrometric measurements, in order to gain insight on the otherwise difficult to observe reactive plasma chemistry of magnetron PECVD. The set of species and reactions was carefully chosen to include enough complexity to render most physicochemical mechanisms of actual discharges, but reduced to a minimal set to lower the computational cost. The influence of the acetylene and argon ratio and the power on the discharge was investigated. It was demonstrated that the injection of acetylene changes the electron density and consequently the concentration of plasma-generated products and sputtered particles even at very low concentrations. This model includes the hyperthermal sputtering of carbon from the target and all principal first order reactions. It also includes their products, and a set of fast secondary reactions that these species undergo on their way to the substrate. Simulations were run at low power due to inherent limitations of PIC-MC models, but it was shown that all densities in the plasma bulk evolved linearly with the discharge power. Good correspondence between simulations and experiments of mass spectrometry was obtained with respect to ions, as the densities of hydrocarbon ions arriving at the substrate grew with the discharge power with the same slopes and relative concentrations in both cases. Good qualitative agreement between simulations and experiments was obtained for density variations with the acetylene ratio. It was possible to identify groups of reactive species from the rate at which their density increased with the acetylene ratio; with primary reactions involving electrons and secondary reactions involving the products of first ones and the background acetylene,

One important results of this study is to show that the spatial distribution of different species can differ a lot: ions are concentrated in a beam due to the unbalanced magnetic field, radicals have surprisingly high concentrations and spread profiles due to their slow diffusion, and sputtered particles form a wide beam, the concentration of which weakens faster with distance than for other species. This implies that the growing film precursor fluxes could be very different depending on the location of the substrate within the chamber. A dynamic surface chemistry model, which relies on defining different sets of reactions on hydrogen-terminated sites and dangling bonds sites, was introduced to get more realistic absorption reactions at the substrate. However, the equilibrium of radical species was not yet attained despite simulating up to several hundred microseconds. The primary focus of this study was to properly define the plasma source and the chemistry inside the chamber. In order to give prediction on deposition speed and film quality, further refinements of the surface model as well as longer simulations would be required.

Despite the difficulty to get reliable mass spectrometric measurements in a PECVD reactor and to run simulations with comparable power and time scales as in experiments, it was possible to correlate simulated and measured species concentrations with varying power and ratio. To our knowledge, these PIC-MC simulations are the first to include this many species and reactions in a fully 3D and self-consistent kinetic plasma model.

Declaration of competing interest

The authors declare that they have no known competing financial interests or personal relationships that could have appeared to influence the work reported in this paper.

Acknowledgments

The authors M. Fauroux and S. Lucas gratefully acknowledge the financial support of the Walloon region under the FEDER and 3DCOATER-5: Convention N° 1610258, project 3215. The present research benefited from computational resources made available on the Tier-1 supercomputer of the Fédération Wallonie-Bruxelles, infrastructure funded by the Walloon Region under the grant agreement n°1117545. It was also part of the "DLC plus" project under the Convention SPW n°1710252, CORNET CALL.

References

[1] T. Melzig, M. Siemers, A. Pflug, R. Rank, 3D PIC-MC simulation of anode effects in dual magnetron discharges, Surf. Coatings Technol. 241 (2014) 30–32, https://doi.org/10.1016/j.surfcoat.2013.10.024.

[2] V. Ivanov, O.V. Proshina, T. Rakhimova, A. Rakhimov, D. Herrebout, A. Bogaerts, Comparison of a one-dimensional particle-in-cell-Monte Carlo model and a one-dimensional fluid model for a CH4/H2 capacitively coupled radio frequency discharge, J. Appl. Phys. 91 (2002) 6296–6302, https://doi.org/10.1063/1.1461895.

[3] O.V. Proshina, T.V. Rakhimova, A.T. Rakhimov, A particle-in-cell Monte Carlo simulation of an rf discharge in methane: frequency and pressure features of the ion energy distribution function, Plasma Sources Sci. Technol. 15 (2006) 402–409, https://doi.org/10.1088/0963-0252/15/3/015.

[4] M. Siemers, A. Pflug, T. Melzig, K. Gehrke, A. Weimar, B. Szyszka, Model based investigation of Ar ion damage in DC magnetron sputtering, Surf. Coatings Technol. 241 (2014) 50–53, https://doi.org/10.1016/j.surfcoat.2013.09.025.

[5] D. Tskhakaya, K. Matyash, R. Schneider, F. Taccogna, The particle-in-cell method, Contrib. to Plasma Phys. (2007), https://doi.org/10.1002/ctpp.200710072.

[6] S. Mathioudaki, C. Vandenabeele, R. Tonneau, A. Pflug, S. Lucas, Characterization of a pulsed low pressure argon discharge in a cylindrical magnetron reactor by plasma diagnostic and 3D plasma modeling, J. Vac. Sci. Technol. A 37 (2019) 031301, , https://doi.org/10.1116/1.5064690.

[7] R. Tonneau, P. Moskovkin, A. Pflug, S. Lucas, TiOx deposited by magnetron sputtering: a joint modelling and experimental study, J. Phys. D. Appl. Phys. 51 (2018) 195202, https://doi.org/10.1088/1361-6463/aabb72.

[8] J. Robertson, Diamond-like amorphous carbon, Mater. Sci. Eng. R Reports. 37 (2002) 129–281, https://doi.org/10.1016/S0927-796X(02)00005-0.

[9] J. Vetter, 60 years of DLC coatings: historical highlights and technical review of cathodic arc processes to synthesize various DLC types, and their evolution for industrial applications, Surf. Coatings Technol. 257 (2014) 213–240, https://doi.org/10.1016/j.surfcoat.2014.08.017.

[10] J. Robertson, Diamond-like carbon films, properties and applications, Compr. Hard Mater. 3 (2014) 101–139, https://doi.org/10.1016/B978-0-08-096527-7.00043-X.

[11] S. Neuville, New application perspective for tetrahedral amorphous carbon coatings, QScience Connect (2014), https://doi.org/10.5339/connect.2014.8.

[12] C. Lopez-Santos, J.L. Colaux, J.C.C. Gonzalez, S. Lucas, Investigation of the growth mechanisms of a-CHx coatings deposited by pulsed reactive magnetron sputtering, J. Phys. Chem. C 116 (2012) 12017–12026, https://doi.org/10.1021/jp300697s.

[13] V. De Vriendt, S.M. Miladinovic, J.L. Colaux, F. Maseri, C.L. Wilkins, S. Lucas,

Growth mechanisms involved in the synthesis of smooth and microtextured films by acetylene magnetron discharges, Langmuir 27 (2011) 8913–8922, https://doi.org/10.1021/la2003035.

[14] D. Thiry, A. De Vreese, F. Renaux, J.L. Colaux, S. Lucas, Y. Guinet, L. Paccou, E. Bousser, R. Snyders, Toward a better understanding of the influence of the hydrocarbon precursor on the mechanical properties of a-C:H coatings synthesized by a hybrid PECVD/PVD method, Plasma Process. Polym. 13 (2016) 316–323, https://doi.org/10.1002/ppap.201500050.

[15] A. Grill, B. Meyerson, V. Patel, Interface modifications for improving the adhesion of a-C:H films to metals, J. Mater. Res. 3 (1988) 214–217, https://doi.org/10.1557/JMR.1988.0214.

[16] D. Sheeja, B.K. Tay, K.W. Leong, C.H. Lee, Effect of film thickness on the stress and adhesion of diamond-like carbon coatings, Diam. Relat. Mater. 11 (2002) 1643–1647, https://doi.org/10.1016/s0925-9635(02)00109-7.

[17] J. Zelez, Low-stress diamondlike carbon films, J. Vac. Sci. Technol. A Vacuum, Surfaces, Film. 1 (1983) 305–307, https://doi.org/10.1116/1.572119.

[18] A. Grill, V. Patel, B.S. Meyerson, Optical and tribological properties of heat-treated diamond-like carbon, J. Mater. Res. 5 (1990) 2531–2537, https://doi.org/10.1557/JMR.1990.2531.

[19] Y. Hirata, J. Choi, Deposition of a-C:H films on inner surface of high-aspect-ratio microchannel, J. Appl. Phys. 120 (2016) 065305, , https://doi.org/10.1063/1.4960694.

[20] Y.Y. Wang, Y. Ye, H. Li, L. Ji, Y.Y. Wang, X. Liu, J. Chen, H. Zhou, Microstructure and tribological properties of the a-C:H films deposited by magnetron sputtering with CH4/Ar mixture, Surf. Coatings Technol. 205 (2011) 4577–4581, https://doi.org/10.1016/j.surfcoat.2011.03.120.

[21] M. Mao, J. Benedikt, A. Consoli, A. Bogaerts, New pathways for nanoparticle formation in acetylene dusty plasmas: a modelling investigation and comparison with experiments, J. Phys. D. Appl. Phys. 41 (2008) 225201, , https://doi.org/10.1088/0022-3727/41/22/225201.

[22] K. De Bleecker, A. Bogaerts, W. Goedheer, Detailed modeling of hydrocarbon nanoparticle nucleation in acetylene discharges, Phys. Rev. E - Stat. Nonlinear, Soft Matter Phys. 73 (2006) 1–16, https://doi.org/10.1103/PhysRevE.73.026405.

[23] C. Deschenaux, A. Affolter, D. Magni, C. Hollenstein, P. Fayet, Investigations of CH4, C2H2 and C2H4 dusty RF plasmas by means of FTIR absorption spectroscopy and mass spectrometry, J. Phys. D. Appl. Phys. 32 (1999) 1876–1886, https://doi.org/10.1088/0022-3727/32/15/316.

[24] D.A. Ariskin, I.V. Schweigert, A.L. Alexandrov, A. Bogaerts, F.M. Peeters, Modeling of chemical processes in the low pressure capacitive radio frequency discharges in a mixture of Ar/C2H2, J. Appl. Phys. 105 (2009) 1–11, https://doi.org/10.1063/1.3095760.

[25] M. Mao, A. Bogaerts, Investigating the plasma chemistry for the synthesis of carbon nanotubes/nanofibres in an inductively coupled plasma enhanced CVD system: the effect of different gas mixtures, J. Phys. D. Appl. Phys. 43 (2010) 205201, , https://doi.org/10.1088/0022-3727/43/20/205201.

[26] Y. Miyagawa, H. Nakadate, M. Tanaka, M. Ikeyama, S. Nakao, S. Miyagawa, PIC simulation of N2 and C2H2 plasma behavior around plural objects, Surf. Coatings Technol. 201 (2007) 8414–8419, https://doi.org/10.1016/j.surfcoat.2006.03.067.

[27] F.J. Gordillo-Vázquez, J.M. Albella, Influence of the pressure and power on the non-equilibrium plasma chemistry of C2, C2H, C2H2, CH3 and CH4 affecting the synthesis of nanodiamond thin films from C2H2(1%)/H2/Ar-rich plasmas, Plasma Sources Sci. Technol. 13 (2004) 50, https://doi.org/10.1088/0963-0252/13/1/007.

[28] A. Baby, C.M.O.O. Mahony, P.D. Maguire, Acetylene-argon plasmas measured at a biased substrate electrode for diamond-like carbon deposition: I. Mass spectrometry, Plasma Sources Sci. Technol. 20 (2011) 015003, https://doi.org/10.1088/0963-0252/20/1/015003.

[29] J.R. Doyle, Chemical kinetics in low pressure acetylene radio frequency glow discharges, J. Appl. Phys. 82 (1997) 4763, https://doi.org/10.1063/1.366333.

[30] J. Benedikt, Acetylene Chemistry in Remote Plasmas: Implications for the a-C:H Growth Mechanism, (2004), https://doi.org/10.6100/IR581182.

[31] C. Hopf, T. Schwarz-Selinger, W. Jacob, A. Von Keudell, Surface loss probabilities of hydrocarbon radicals on amorphous hydrogenated carbon film surfaces, J. Appl. Phys. 87 (2000) 2719–2725, https://doi.org/10.1063/1.372246.

[32] A. Bogaerts, E. Bultinck, I. Kolev, L. Schwaederlé, K. Van Aeken, G. Buyle, D. Depla, Computer modelling of magnetron discharges, J. Phys. D. Appl. Phys. 42 (2009) 194018, , https://doi.org/10.1088/0022-3727/42/19/194018.

[33] A. Bogaerts, E. Bultinck, M. Eckert, V. Georgieva, M. Mao, E. Neyts, L. Schwaederlé, Computer modeling of plasmas and plasma-surface interactions, Plasma Process. Polym. 6 (2009) 295–307, https://doi.org/10.1002/ppap.200800207.

[34] A. Pflug, M. Siemers, T. Melzig, L. Schäfer, G. Bräuer, Simulation of linear magnetron discharges in 2D and 3D, Surf. Coatings Technol. 260 (2014) 411–416, https://doi.org/10.1016/j.surfcoat.2014.09.042.

[35] A.B. Langdon, Effects of the spatial grid in simulation plasmas, J. Comput. Phys. (1970), https://doi.org/10.1016/0021-9991(70)90024-0.

[36] M.-Y. Song, J.-S. Yoon, H. Cho, G.P. Karwasz, V. Kokoouline, Y. Nakamura, J. Tennyson, Cross sections for electron collisions with hydrogen molecules, J. Phys. Chem. Ref. Data 37 (2008) 913–931, https://doi.org/10.1063/1.2838023.

[37] R.K. Janev, D. Reiter, Collision processes of C2,3Hy and C2,3Hy+ hydrocarbons with electrons and protons, Phys. Plasmas. 11 (2004) 780–829, https://doi.org/10.1063/1.1630794.

[38] T.J. Bartel, S. Plimpton, M.A. Gallis, Icarus: A 2D Direct Simulation Monte Carlo (DSMC) Code for Multi-Processor Computers User's Manual-v10.0, (2001).

[39] P.M. Mul, J.W. McGowan, Dissociative recombination of C2+, C2H+, C2H2+ and C2H3+, Astrophys. J. 237 (1980) 749, https://doi.org/10.1086/157921.

[40] T. Shirai, T. Tabata, H. Tawara, Y. Itikawa, Analytic cross sections for electron collisions with hydrocarbons: CH4, C2H6, C2H4, C2H2, C3H8, and C3H6, At. Data Nucl. Data Tables 80 (2002) 147–153, https://doi.org/10.1006/adnd.2001.0878.

[41] R. Engeln, K.G.Y. Letourneur, M.G.H. Boogaarts, M.C.M. van de Sanden, D.C. Schram, Detection of CH in an expanding argon/acetylene plasma using cavity ring down absorption spectroscopy, Chem. Phys. Lett. 310 (1999) 405–410, https://doi.org/10.1016/S0009-2614(99)00810-6.

[42] D. Thirumalai, K. Onda, D. Truhlar, Elastic scattering and rotational excitation of a polyatomic molecule by electron impact: acetylene, J. Chem. Phys. (1981) 526, https://doi.org/10.1063/1.440804.

[43] V. Sushkov, A.-P. Herrendorf, R. Hippler, Metastable argon atom density in complex argon/acetylene plasmas determined by means of optical absorption and emission spectroscopy, J. Phys. D. Appl. Phys. 49 (2016) 425201, , https://doi.org/10.1088/0022-3727/49/42/425201.

[44] A. Fridman, Plasma Chemistry (2008), https://doi.org/10.1017/CBO9780511546075.

[45] F.J. Gordillo-Vázquez, J.M. Albella, Distinct nonequilibrium plasma chemistry of C2 affecting the synthesis of nanodiamond thin films from C2H2(1%)/H 2/Ar-rich plasmas, J. Appl. Phys. 94 (2003) 6085–6090, https://doi.org/10.1063/1.1617362.

[46] J. Benedikt, Plasma-chemical reactions: low pressure acetylene plasmas, J. Phys. D. Appl. Phys. 43 (2010) 43001, , https://doi.org/10.1088/0022-3727/43/4/043001.

[47] J.E. Butler, R.L. Woodin, L.M. Brown, P. Fallon, Thin film diamond growth mechanisms, Philos. Trans. R. Soc. A Math. Phys. Eng. Sci. 342 (1993) 209–224, https://doi.org/10.1098/rsta.1993.0015.

[48] C. Hopf, A. von Keudell, W. Jacob, Chemical sputtering of hydrocarbon films by low-energy Ar ion and H atom impact, Nucl. Fusion. 42 (2002) L27–L30, https://doi.org/10.1088/0029-5515/42/12/101.

[49] A. Von Keudell, M. Meier, C. Hopf, Growth mechanism of amorphous hydrogenated carbon, Diam. Relat. Mater. 11 (2002) 969–975, https://doi.org/10.1016/S0925-9635(01)00553-2.

[50] Y. Lifshitz, S.R. Kasi, J.W. Rabalais, W. Eckstein, Subplantation model for film growth from hyperthermal species, Phys. Rev. B 41 (1990) 10468–10480, https://doi.org/10.1103/physrevb.41.10468.

[51] J.F. Ziegler, M.D. Ziegler, J.P. Biersack, SRIM – the stopping and range of ions in matter (2010), Nucl. Instruments Methods Phys. Res. Sect. B Beam Interact. with Mater. Atoms. 268 (2010) 1818–1823, https://doi.org/10.1016/j.nimb.2010.02.091.

[52] M.W. Thompson, Physical mechanisms of sputtering, Phys. Rep. 69 (1981) 335–371, https://doi.org/10.1016/0370-1573(81)90106-X.

[53] D. Depla, G. Buyle, J. Haemers, R. De Gryse, Discharge voltage measurements during magnetron sputtering, Surf. Coatings Technol. 200 (2006) 4329–4338, https://doi.org/10.1016/j.surfcoat.2005.02.166.

[54] William E. Wallace, NIST Chemistry webBook, NIST Standard Reference Database Number 69, National Institute of Standards and Technology, Gaithersburg MD, 2020, https://doi.org/10.18434/T4D303.

[55] M. Buddhadasa, C.R. Vandenabeele, R. Snyders, P.-L. Girard-Lauriault, Single source precursor vs. precursor mixture for N-rich plasma polymer deposition: plasma diagnostics and thin film analyses, Plasma Process. Polym. 14 (2017) 1700030, , https://doi.org/10.1002/ppap.201700030.

[56] J. Benedikt, A. Hecimovic, D. Ellerweg, A. Von Keudell, Quadrupole mass spectrometry of reactive plasmas, J. Phys. D. Appl. Phys. 45 (2012), https://doi.org/10.1088/0022-3727/45/40/403001.

[57] A. Anders, P. Ni, J. Andersson, Drifting ionization zone in DC magnetron sputtering discharges at very low currents, IEEE Trans. Plasma Sci. 42 (2014) 2578–2579, https://doi.org/10.1109/TPS.2014.2334601.

[58] N. Brenning, J.T. Gudmundsson, D. Lundin, T. Minea, M.A. Raadu, U. Helmersson, The role of Ohmic heating in dc magnetron sputtering, Plasma Sources Sci. Technol. 25 (2016) 65024, , https://doi.org/10.1088/0963-0252/25/6/065024.

[59] S.Z. Wu, Dependence of plasma characteristics on dc magnetron sputter parameters, J. Appl. Phys. 98 (2005), https://doi.org/10.1063/1.2112177.

[60] M. Tsuji, H. Kouno, K. Matsumura, T. Funatsu, Y. Nishimura, H. Obase, H. Kugishima, K. Yoshida, Dissociative charge-transfer reactions of Ar+ with simple aliphatic hydrocarbons at thermal energy, J. Chem. Phys. 98 (1993) 2011–2022, https://doi.org/10.1063/1.46423.

4.1 Complements

4.1.1 Mass spectrometer biases

One problem commonly faced when doing mass spectrometry, is that unless the vacuum is extreme there is most often water vapor and other pollutant like oxygen, carbon dioxide/monoxide and nitrogen, present in a vacuum chamber and entering in the detector. In our case this is problematic because carbon mono/dioxide and water molecules have masses close to some hydrocarbon molecules produced in the plasma. In order to reduce this noise, the chamber was heated overnights before experiments to get a better vacuum and the ionizer filament was powered for several hours prior to MS measurements. Another source of pollution came from the gas injections and this created problems when changing the injection flux of Ar and C_2H_2 or operating the gas valves (see Figure 4.1).

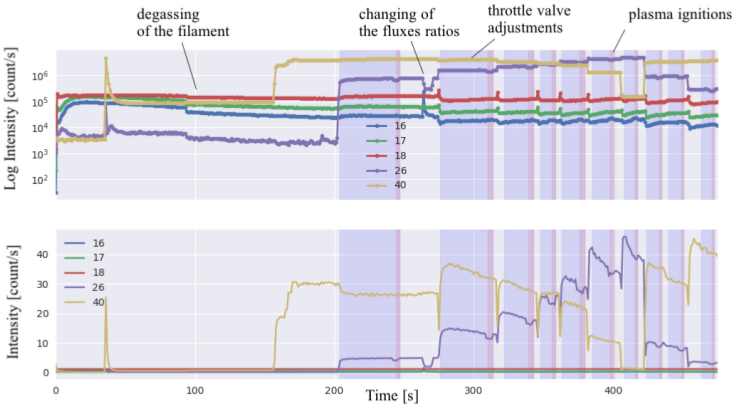

Figure 4.1 Evolution of some mass spectrometry lines during several plasma discharge with varying C_2H_2 ratio. Between each plasma ignition (red ranges), the flux where adjusted, then the pressure was stabilized to 5 mTorr by adjusting the turbopump throttle valve (blue range). A long period of degassing of the MS ionizing filament (beginning of the plot until 200). This figure demonstrates that the water lines (m/z = 16, 17, 18 u) where diminishing with filament degassing but that gas injection brought more water vapor.

Another issue with the MS measurements was the proximity and interaction between the end cap of the detector (the 100µm inlet) and the plasma. In fact, in presence of acetylene and only 10 cm away from the discharge the fluxes of radicals, ions and electrons were quite important and it created several issues: (i) the end-cap could get cluttered by the deposition of a-CH changing the size of the hole and thus the throughput (microscope observations showed afterward that this seems to not have happened) ; (ii) the dielectric film could mask the end-cap potential (a-CH is dielectric) which could have an effect on the discharge itself since it acted as an anode [132,133], (iii) lastly the charged particle bombardment might also have had an effect on the end-cap's potential. Figure 4.2 show the effect of moving the detector closer or further from the cathode on the mean intensity of several spectral lines. When the magnetron was far from the MS then the signal was proportional to the distance but when the MS was closer than 10 cm then the signal would abruptly disappear. The observed variation of the signal when the distance was large could easily be explained by a conjunction of: (i) the decrease in density of charged particles with distance observed in simulations (see Figure 9 of Article 1), (ii) and the decrease of the solid angle of the end-cap hole with the distance[24].

---

[24] *Logical argument: since charged particles are generated close to the target's surface the signal will diminishes with distance due to a decreased probability of reaching the end-cap hole.*

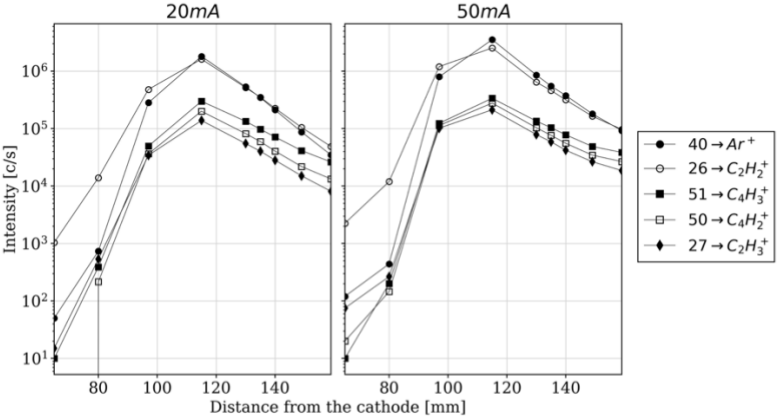

Figure 4.2 Average intensity of several MS lines vs the distance between the spectrometer and the magnetron for a discharge with C_2H_2 *and Ar at 20 mA and 50 mA.*

Lastly, the ignition of a plasma in C_2H_2 creates a lot of reactive compound which can have very short lifespan and be hard to detect, but the filament ionizer which is required for RGA can also dissociate the C_2H_2 molecules in similar compounds, making the detection of species like C_2H very tricky[25]. Since those species also gets deposited inside the chamber and since the pumping speed was fixed the ignition of a discharge changed the chamber pressure slightly which affected the intensity of MS measures. Additionally, the acetylene bottle used to inject gas contained an acetone solvent which created some additional

---

[25] *Those other sources of uncertainty are discussed in more details in the article presented in Chapter 4.*

peaks as already explained in the article (see Figure 5 of Article 1 and associated discussions).

4.1.2 EEDF

One advantage of PIC-MC simulation is that the energy transport of electrons and other charge particles is simulated in a self-coherent and realistic manner. One way to study the behaviour of electrons is to look at the electron energy density function (EEDF) in various places within the chamber. This give valuable insights to the plasma generation mechanisms and allows prediction of the reaction rates of all electron-collision reactions (see section 2.1.3). This also allow direct comparisons with EEDFs obtained with Langmuir probe measurements. Unfortunately, in the case of reactive plasma with an high deposition rate of a dielectric film like with acetylene Langmuir measurement are hard to obtain and less reliable [131].

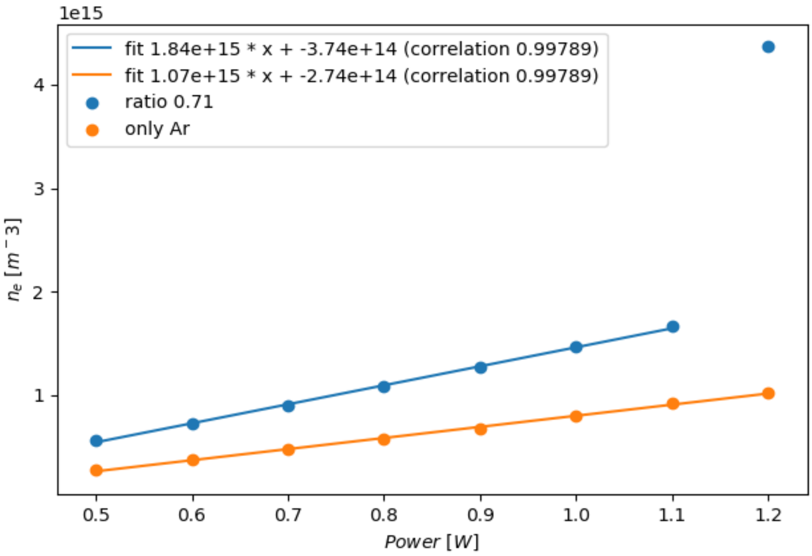

Figure 4.3 Electronic density vs power for pure Ar and a mixture of 71% Ar and 29% C_2H_2.

As explained in Chapter 2, many studies of acetylene plasma rely on Monte-Carlo or PIC-MC simulations of the plasma ignition and the charged particle behaviour with only the noble gas (Ar in most cases) to simplify the simulations. Then the EEDF and the charged particle behaviour can be coupled with chemistry simulations to get the full picture. The idea being that the spatial behaviour of charged particle and their energy will be simulated correctly only with Ar, and that the chemistry model only needs the EEDF as an input. However, the energy of electrons in a plasma depends on the nature of the gas present in the chamber and thus cannot be accurately reproduce without adding C_2H_2 and all its possible collisions with electrons to the simulations. This is well demonstrated by the Figure 4.3, which shows the difference in electron density between a simulation of a pure argon plasma and one ignited with 29% C_2H_2 at various power.

One characteristic trait of plasma discharges in DC magnetrons at low pressure (<16 mTorr [134]) is the fact that the EEDF appears to be bi-Maxwellian [134–136] in the vicinity of the magnetic trap. Which means that there are at least two population of electrons with different mean energies: (i) High energy electrons coming from the secondary emitted electrons (SEE) that are emitted from the target surface on ion impact and accelerated through the shield, (ii) low energy ones created by ionisation within the bulk and thermalizing through collisions with other particles or electrons. Even though, that is the common explanation, there is still some debate about the nature of those population and the possible existence of a third population accelerated through the pre-shield through what is called ohmic heating. In [137], Brenning et al. demonstrated that ohmic heating might actually be the main source of electron energisation in DCMS (DC Magnetron Sputtering) when the SEEY (Secondary Emitted Electron Yield) is bellow 0.1[26].

The two simulation approaches to study the electron energisation mechanisms are both limited: (i) with Boltzmann 2-terms

---

[26] *In our simulation the SEEY was set to 0.11 as it is a typical value for Ar ions on metallic targets however the exact value in our case with Ar and hydrocarbon ions on a graphite target is not known.*

approximation models the electron collisions are all included but the confinement and electron dynamics are not considered, (ii) with PIC-MC models the e-e collisions are neglected. However, at low pressure or with low ionisation degree the role of the e-e collisions is less important [138].

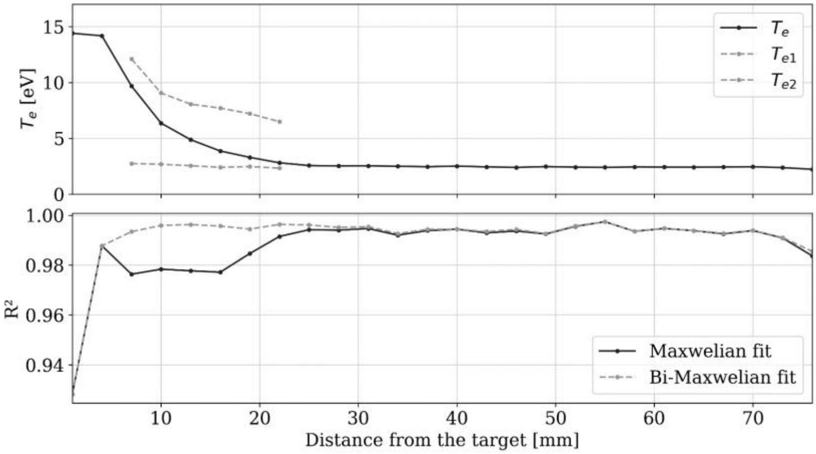

Figure 4.4 Electronic temperature in the chamber, fitted with a Maxwellian distribution function (plain) and bi-Maxwellian (dashed). Bellow: Fits' accuracy (r^2).

In Figure 4.4, the mean energies of the electrons throughout the chamber is presented with a Maxwellian and a bi-Maxwellian fit for a typical simulation. It is clear from that the fit with bi-Maxwellian is better suited in the bulk region and gives a population with around 6-10 eV of energy, and another one, which span throughout the chamber, with a mean energy of around 2 eV. The exact origin of those two population is unclear and a more detailed analysis of the individual trajectories of electrons could give us more information. Due to the lack of experimental data on the EEDF complete study of this aspect could not be done and the EEDFs obtained from simulation are the only window on the electron energisation that we have. The fact that the mean energy of this second population is around 10 eV which is close to the ≈ 10 V of the plasma potential before the presheath would tend to favour the explanation of Brenning et al. [137] of role of the Ohmic heating from the potential drop in the pre-sheath.

Chapter 5 *Simulation of the film growth (Article 2)*

This work focuses on the film deposition mechanisms in a low-pressure argon-acetylene magnetron assisted plasma via Particle-in-Cell Monte-Carlo simulation in combination with a chemical surface model including saturated and dangling bond sites to account for the film growth mechanisms involving reactive radical species. A main point of interest was to find out whether the film growth is dominated by ions, by radicals or by target sputtering. Predictions were made regarding the equilibrium coverage and the deposition profile at equilibrium for various acetylene ratios by varying the initial surface coverage of dangling bonds, fitting its evolution with time and extrapolating predictions to discharge powers. These predictions were tested against experimental a-CH film characterizations, including RBS/ERDA, XPS, Raman, and profilometer measurements. Even if high uncertainty remains, we demonstrated that films deposited on a grounded substrate facing the target have Gaussian deposition profiles which can be reproduced quantitatively for various C_2H_2 *ratios. This model could be used to accelerate the search for optimal deposition parameters for more complex deposition configurations without relying on costly trial-and-errors, and to get a clearer understanding on the underlying processes which is hard to obtain with in-situ experiments for PECVD.*

Surface & Coatings Technology 421 (2021) 127472

Contents lists available at ScienceDirect

Surface & Coatings Technology

journal homepage: www.elsevier.com/locate/surfcoat

Experimental and theoretical study of a magnetron DC-PECVD acetylene discharge: Identification of the deposition precursors and film growth mechanisms

A. Fauroux [a], A. Pflug [b], S. Lucas [a,*]

[a] *Laboratoire d'Analyse par Réactions Nucléaires (LARN), Namur Institute of Structured Matter (NISM), University of Namur, 61 Rue de Bruxelles, 5000 Namur, Belgium*

[b] *Fraunhofer Institute for Surface Engineering and Thin Films IST, Bienroder Weg 54e, 38108 Braunschweig, Germany*

ARTICLE INFO

Keywords:
PIC-MC
Magnetron
DLC
a-C:H
PECVD
Simulation
C_2H_2

ABSTRACT

This work focuses on the film deposition mechanisms in a low-pressure argon-acetylene magnetron assisted plasma via Particle-in-Cell Monte-Carlo simulation in combination with a chemical surface model including saturated and dangling bond sites to account for the film growth mechanisms involving reactive radical species. A main point of interest was to find out whether the film growth is dominated by ions, by radicals or by target sputtering. Predictions were made regarding the equilibrium coverage and the deposition profile at equilibrium for various acetylene ratios by varying the initial surface coverage of dangling bonds, fitting its evolution with time and extrapolating predictions to discharge powers. These predictions were tested against experimental a-CH film characterizations, including RBS/ERDA, XPS, Raman, and profilometer measurements. Even if high uncertainty remains, we demonstrated that films deposited on a grounded substrate facing the target have Gaussian deposition profiles which can be reproduced quantitatively for various C_2H_2 ratios. This model could be used to accelerate the search for optimal deposition parameters for more complex deposition configurations without relying on costly trial-and-errors, and to get a clearer understanding on the underlying processes which is hard to obtain with in-situ experiments for PECVD.

1. Introduction

Amorphous hydrogenated carbon (a-CH) is a popular coating type which confers many interesting properties to surfaces, such as chemical inertness, IR transparency, wear resistance, or hardness [1]. For this reason, scientific and industrial communities have developed many techniques through the years to deposit such coatings on various substrates. A common trade-off is that the approaches using Plasma-Enhanced Chemical Vapor Deposition techniques (PECVD) with acetylene or other precursors tend to be fast, but they create more polymeric-like films, whereas the methods involving higher energy ions producing more tetrahedral amorphous-hydrogenated carbon (ta-CH) are usually slower. Thus, the aim is usually to maximize the deposition rate while keeping enough sp^3 bonds and lowering the H content of films in order to obtain hard a-CH. Several problems might also need to be circumvented: stress-induced film delamination [2,3], non-homogeneous films on high aspect-ratio substrates [4], cathode pollution with PECVD based deposition methods, difficulty to obtain films of the same quality in different chambers or on various substrates [5].

Simulating a deposition process and predicting the film properties is of great interest for the community. This is the purpose of this work. As a starting point, our case study selection was a deposition method based on a mixed PVD/PECVD process at low pressure (below 1 Pa) which uses an unbalanced magnetron with a graphite target and acetylene (C_2H_2) as precursor. Even though this technique does not produce the strongest coatings or achieve the fastest deposition rates, it is still widely used by industrials since it can be easily upscaled in large batch coaters [6] and it is a simpler version of many deposition techniques which produce state-of-the-art coatings like e.g. multilayers [7–10], or doped films [11–14]. Additionally, various techniques like e.g. complex substrate motions, substrate bias and temperature control, can be used to improve films quality and to produce more homogenous films on 3D substrates [4,15]. In a previous study [16], the authors showed that PIC-MC simulation was a suitable method to reproduce most of the discharge mechanisms,

---

* Corresponding author.
E-mail address: stephane.lucas@unamur.be (S. Lucas).

https://doi.org/10.1016/j.surfcoat.2021.127472
Received 30 April 2021; Received in revised form 20 June 2021; Accepted 26 June 2021

including the complex plasma chemical reactions (PCR) in a simplified but self-coherent manner. The simulations were tested through the comparison of the predicted ion and radical concentrations with mass spectrometric (MS) measurements for various C_2H_2/Ar ratios and discharge powers. Linear dependency of the reactive species densities on power was observed in both simulations and experiments. The advantage of having a 3D representation of the plasma chamber became apparent with the geometrical differences between the fluxes of different species, which enabled us to predict how the film deposition condition might vary throughout the chamber. Interestingly, we observed that, similarly to the case of expanding thermal plasmas (ETP) [17], the reactive species produced inside the plasma were likely to interact with the background acetylene on their way to the substrate, producing yet more reactive and sometimes heavier species.

This new study aims at looking further into the PIC-MC model predictions regarding the deposited films by using experimental film characterization technics like Elastic Recoil Detection Analysis (ERDA) and Rutherford Backscattering Spectroscopy (RBS), X-ray Photoelectron Spectroscopy (XPS), Raman spectroscopy, or profilometry. For this purpose, a refined deposition model had to be implemented. Surface reaction probabilities are difficult to obtain because atomistic deposition models like Molecular Dynamics (MD) give results which depend on the surface state, the species orientations, internal energies and so on. Similarly, experiments can only give partial and empirical information on the deposition precursors and the particular surface reactions. Therefore, we tried to identify the most probable deposition precursors, to clarify the respective roles of the radicals, the sputtered carbon and the ion bombardment, with the intent to check if the different deposition conditions described in Fauroux et al. [16] induce differences in film properties, which could be verified experimentally. The description of the simulation model and the experimental apparatus can be found in Fauroux et al. [16]. Furthermore, we provide more details on the characterization experiments and the simulations: the experimental setups for film deposition and for substrate characterization are presented in Sections 2.1 and 2.2, while several simulation modifications along with the improved deposition model are described in Sections 2.3 and 2.4. The results are presented in three parts: the characterization of the nature of the films in Section 3.1, followed by a comparative study of deposition rates and film profiles in both experiments and simulations in Section 3.2. Lastly, the validity of these results and what can be learned from them is discussed in Section 3.3.

2. Method description

2.1. Deposition setup

For this work, a research reactor already described in Tonneau et al. [18] and in Fauroux et al. [16] was used. In order to accelerate the simulations, its shape was simplified to a small box, as schematically represented in Fig. 1. Like in Fauroux et al. [16], the plasma was generated with an unbalanced circular magnetron sputter source in DC mode with a 2 in. graphite target of 99.9% purity (Kurt J. Lesker) at a pressure of 5 mTorr (0.66 Pa) in argon and acetylene. The current was imposed to 100 mA for all depositions and the resulting discharge powers remained close to 50 W or 1.25 W cm^2, but slowly increased due to cathode pollution. To circumvent the effect of cathode pollution, etching with pure argon and protecting shutters was performed prior to any deposition, and deposition times were chosen shorter for higher deposition rates conditions. The pressure was kept constant by adjusting the throttle valve angle of the turbomolecular pump. When varying the acetylene/argon ratio, the total mass flow was kept constant at around 16 sccm. A rectangular substrate holder was placed in the middle of the chamber, parallel to the target's face at a distance of 86.35 mm, as can be seen on Fig. 1. Several a-CH films were deposited on 60 mm-long and 12 mm-wide silicon strips (P doped silicon, <100>, 1–10 Ω cm^{-1} resistivity, polished finish, native oxide layer), placed vertically and parallel to the cathode and on square glassy carbon samples of 12 mm width and 3 mm thickness for the ion beam analysis (the location of the glassy carbon sample can be seen in Fig. 1). Kapton tape was used to cover samples and create a step for profilometry.

2.2. Film characterization

The thickness profiles along the vertical axis were measured by profilometry on partly masked substrates (Dektak). Mass spectrometry (MS) measurements of the neutrals and ions at the substrate position were already reported in Fauroux et al. [16] using a quadrupole mass spectrometer connected to the deposition chamber by a 100 µm in diameter extraction orifice, facing the magnetron target at distance of 10 cm. However, in this study the MS was set to scan the ion count for

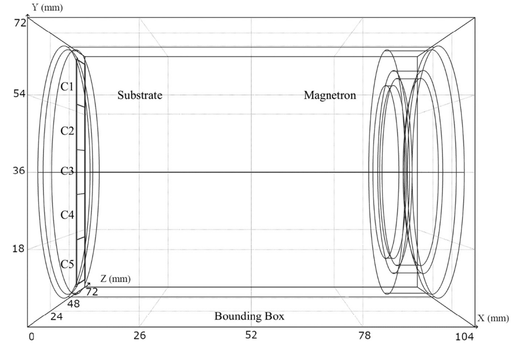

Fig. 1. Scheme of the deposition chamber used for simulations, with samples from C1 to C5 used for experimental a-CH film depositions. Coordinates are given in millimeters. The magnetron target surface is at x = 91.35 mm, and the substrate surface is at x = 5 mm.

several energy bins of 0.05 eV width from 0 to 10 eV for every mass in [1, 60 u], thus providing information about the energy of all main ion species (as can be seen in the supplementary material, Appendix A). Atom compositions were obtained by ion beam analysis (IBA) through the combination of ERDA and RBS with the use of a tandem accelerator (High Voltage Engineering, 2 MV terminal voltage). An impinging beam of $4He^+$ at 3.5 MeV of about 1.5 mm in diameter with a typical current of 10 nA was used, and the sample surface was tilted by an angle of 70° with respect to the incident beam direction. The detectors were placed at 135° (RBS) and 30° (ERDA). The film densities were obtained by comparing the surface mass density (atom count per surface unit) from ERDA with the profilometer-measured thickness. Raman shifts were measured with a DXR SmartRaman microscope (ThermoFisher, USA) using an 8 mW power and 532 nm laser with a 2.1 μm wide beam as the excitation source. XPS measurements were performed on the a-CH samples in an Escalab 250Xi machine (ThermoFisher Scientific, England) with a 1486.7 eV monochromatic Al Kα X-ray source and a 400 μm wide spot. Soft etching with 1000 Ar atoms clusters at 6 kV were performed for 200 s on 2 × 2 mm^2 areas before each measure.

2.3. Simulation parameters

The simulations presented here mostly used similar parameters as those in the authors' previous study [16]. However, several improvements were made. Firstly, the angular distribution of sputtered carbon atoms from the target was refined according to the findings of a study by Oyarzabal et al. [19]. In this study, the authors measured, with an MS, the angular distribution and yield of sputtered carbon from graphite targets bombarded with different noble gases (including Ar) at energies ranging from 75 to 225 eV. They noticed that this angular distribution follows a flattened cardioid with higher probability for wider angles. In order to use this distribution in the simulations, it was fitted using an approach given in Yamamura et al. [20]:

$$f(\theta) = cos(\theta)\left(1 + \alpha cos^2(\theta)\right), \tag{1}$$

where θ is the sputtered particle angle, and $\alpha = -0.94$ the fitted variable. Interestingly, Oyarzabal et al. [19] found that the sputtering of carbon clusters (C_2, C_3) is highly probable for Ar^+ bombarding leading to a fraction of around 30% of the carbon clusters in the sputter flux at 125 eV of energy. However, since sputtered C particles do not react much with the other PCR products or C_2H_2 in our model, those clusters would have the same behaviour as C with a much lower concentration, and therefore they were not included. Another interesting result of that work [19] is that the sputtered carbon density decreases linearly when averaged along an axis normal to the target – exactly as shown in our simulations [16]. Secondly, C_2H_2 vibrational excitation collisions with cross sections given in Song et al. [21] were added to the simulations. These additional reactions turned out to have a small impact on the electron temperatures inside the plasma and enabled some ionisation of excited C_2H_2 to occur far from the plasma bulk by low-energy electrons.

Another change in the PCR model concerns the exothermic reactions. Several reactions included in our model had an exothermic part [16]. For example, the charge transfer between Ar^+ and C_2H_2 has 4.36 eV excess energy [22] (and not 4.86 eV as was previously erroneously written in our previous article [16]). By default, the exothermic part of the collisions in the simulation software is released as kinetic energy of the reactions product. However, Tsuji et al. [22] stated that for this charge transfer reaction, the most probable state of $C_2H_2^+$ is a near-resonant high vibrationally excited energy level, which means that only a tiny fraction of this energy is converted into kinetic energy and the rest would be released by spontaneous or stimulated photoemission, which is not tracked by the simulation [22,23]. This additional kinetic energy appeared as a broad peak around 4 eV in the $C_2H_2^+$ energy distribution in the simulations but was not present in the IEDF obtained with the MS. Hence these reactions were kept, but all exothermic parts were removed from the new simulations. Charged and neutral species are represented by super-particles, which usually comprise a larger number of real particles via a statistical weight factor. In order to optimize simulation time and keep an accurate representation of the PCR, these weight factors were slightly modified in comparison to Ref. [16]. A summary of the simulation parameters is given in Table 1.

2.4. The surface model

In this work the surface model, which is already described briefly in Fauroux et al. [16], is improved towards a more realistic description of the deposition process with better accuracy. The resulting film-growth model is depicted in Fig. 2. The substrate surface consists of two material types symbolised by the terminology "a-C" and "a-CH", which represent the dangling bonds (DB) where radicals can attach easily, and H-terminated sites, respectively. In practice, only the ratio of a-C and a-CH bonds, or coverage, in each 1 mm^2 cells of the substrate is defined, and the surface reaction probabilities are calculated from this value.

The bond density of amorphous carbon should be in the order of 1×10^{19} m^{-2}. However, in order to speed things up, a smaller value of 1×10^{15} m^{-2} was chosen. This only affects the evolution of the coverage but does not play any role in equilibrium since the deposition rate is calculated from the balance between particle absorption and desorption, using the experimental film density to get a thickness evolution.

According to [24], C_2H_2 has a very low sticking coefficient even on DB as its triple bond is very hard to break and it is a closed shell neutral. This means that the film deposition is mainly caused by ions or radicals produced in the plasma, as shown in Fauroux et al. [16]. Several models for the deposition of a-CH coexist in literature, depending on the deposition methods and types of films. When hydrocarbon or pure carbon ions with energies up to several 100 eV are the main source for growth, an ion subplantation model is used as in Lifshitz et al., Miyagawa et al., and Robertson [25–27]. The range at which the ions can be subplanted is in direct correlation with their energy and the sp^3

Table 1
Physical and numerical parameters of the simulations.

Simulation volume size	$104 \times 72 \times 72$	[mm]
Target diameter	50.8	[mm]
Input power	$0.6 - 1.0$	[W]
Input power density	$2.9 \times 10^{-2} - 4.9 \times 10^{-2}$	$[W \cdot cm^{-2}]$
Temperature	300	[K]
Species	$Ar, Ar^+, C_2H_2, C_2H_2^+, H, C_2H, C_2H^+, CH, C_2,$ $H_2, C, C_4H_2, C_2H_3, C_4H_2^+, C_4H_3^+, C_2H_3^+$	
Pressure	0.6	[Pa]
Magnetron radius	25.4	[mm]
Magnets remanence	1.4	[T]
Cell size	$0.5 - 1.84 \times 1.5 \times 1.5$	[mm]
Arrangement of simulation volume segments	$5 \times 2 \times 2$	
Time step	3×10^{-11}	[s]
Maximum physical simulation time	1×10^{-3}	[s]
CPU cores used	21	
Weight factors Ar, C_2H_2	$1 \times 10^{10} \times$ ratio	
Weight factors e, Ar^+, $C_2H_2^+$	$1.3 \times 10^5 - 4.6 \times 10^3$	
Weight factors for all other species	$6 \times 10^2 - 1.7 \times 10^4$	
Sampling for the power dissipation	1×10^{-7}	[s]
Carbon Yield from Ar^+	0.03	
Carbon Yield from $C_2H_2^+$	0.14	
Secondary electron emission Yield	0.11	
C_2H_2 ratios simulated	4, 10, 15, 20	[%]
Surface bond density	1×10^{15}	$[m^{-2}]$

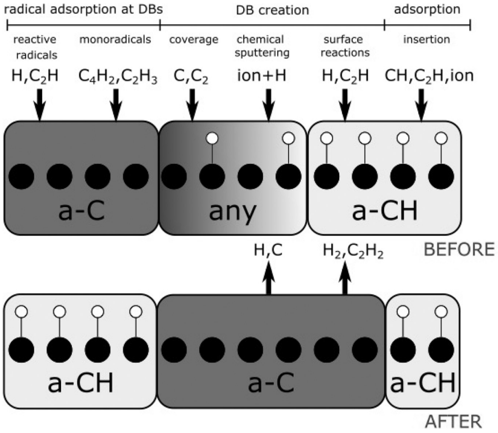

Fig. 2. Representation of the a-C:H film growth model used in the simulations of this study. The white circles represent H atoms, and the black circles mark C atoms. The surface state is defined by the percentage of coverage of the two materials named "a-CH" and "a-C" at every points of the substrate. These names stand for hydrogen terminated sites and dangling bonds respectively. The surface reactions probability depends on the state of the surface at the location of the particle impingement.

formation originates from film subsurface densification, which can revert to sp^2 phase when the ion energy is too high or after annealing [27]. For magnetron sputtering, subplantation of ions deep into the film, and physical sputtering can only occur if a bias is applied to the substrate. However, without bias, ions can still cause knock-on implantation, chemical sputtering, and get implanted close to the substrate surface [28,29]. In the case where the deposition mainly originates from reactive neutrals (PECVD), the film growth models [24,30,31] involve the adsorption via a two-step mechanism in which the reactive species attach to the surface and diffuse until they reach a DB site, or are pushed into the film by impinging ions. This phenomenon is sensitive to temperature and dependant on the DB availability, which are mainly created from reactions between radicals and the surface hydrogen. Lastly, in the case of magnetron PVD, sputtered material is generated at the cathodes with high energies and condenses onto the substrate with a high sticking coefficient but a low flux [32–34].

The sticking coefficients (SC) of all species are not known to the authors' knowledge, but some general conclusions can be drawn from literature. Hopf et al. [35] shows that the surface loss probability of C_2H (identified as the most probable precursor) is around 0.9 on a-CH, and can be decomposed into the sticking coefficient of 0.9 and a loss of 0.1 by the reaction $C_2H + \text{a-CH} \rightarrow C_2H_2 + \text{a-C}$. The authors also explain that the sticking coefficients of C_2H and C_2H_3/C_2H_5 are predicted to be respectively 0.8 and 0.3 because of their hybridization. It is also possible to evaluate sticking coefficients (SC) from simulation. The most common method is Molecular Dynamics (MD), and Neyts et al. [36,37] conducted a comprehensive study of this kind on the reactivity of hydrocarbon radicals on a-CH. They found the sticking coefficients of CH, C_2, and C_2H to be between around 0.8 and more than 0.9 at 0.026 eV of internal energy, going down to around 0.5 at 2 eV. They also correlated the H content of films with the sticking coefficients of H, C, CH, C_2, and C_2H diminishing from above 0.8 to less than 0.5 for H content between 0% and 35%. MD simulation revealed that surface reactions are sensitive to particular atomic arrangement, which is irrelevant at the scale of the substrate, and also that they are sensitive to the internal energies, which cannot easily be taken into account in PIC-MC/DSMC simulations. They also concluded that the SCs of reactive hydrocarbon radicals depend on the number of available electrons; for example, the SC of C_2 approaches 1 on a-CH because it can insert directly into C—C or C—H bonds, whereas closed shell radicals like C_4H_2 or monoradicals like C_2H_3 will have a low SC on hydrogenated surface and a chance to deposit only on dehydrogenated surfaces or DBs [36,38].

Hydrogen also plays a very important role in this type of surface chemistry as it is quite reactive and can either bond to the surface or etch bonded hydrogen from the surface, creating non-reactive H_2 molecules. The probability of these two reactions to occur can be found in Meier and Von Keudell [39], where a simple growth model for the deposition of a-CH by a flux a CH_3 and H is described, based on the set of balance equations which takes into account the creation of DB by H reacting with a cross section of $\sigma_{desor} = 0.05$ Å^2, and the closing of a H bond with a cross section of $\sigma_{adsor} = 1.3$ Å^2. These cross-sections have been converted to probabilities in our model by assuming that the probability of the reaction $H + \text{a-CH} \rightarrow H_2 + \text{a-C}$ is P and the one of $H + \text{a-C} \rightarrow \text{a-CH}$ is 1-P, with $P = \sigma_{desor}/\sigma_{adsor}$. Another important role of hydrogen atoms, shown by Hopf et al. [29], is that they can diffuse up to 2 nm deep within the film and close DBs created by ion impingement [17], which results in synergistic effects on chemical desorption between ion bombardment and the presence of an H flux. The study shows that, in the presence of H, the desorption caused by impinging ions has a very low threshold and a high yield. For example, a yield of 0.6 at only 20 eV in the presence of a H flux was observed. The authors provided the following model of this phenomenon:

$$Y(Ar^+|H)_{model} = Y_{phys} + r/(r+s) \times \left(Y_{chem} - Y_{phys}\right), \quad (2)$$

with $Y_{phys} = 0.1$, $Y_{chem} = 3$, $s = 200$, and $r = j_H/j_{Ar}^+$ the flux ratio. We used this model with values found in a simulation: a ratio of $r = 1/3398$, an average energy for Ar^+ of 0.6 eV, and obtained a probability of chemical sputtering of 0.00797. Due to the lack of a better approximation, this value was applied to all the ions in our simulation. Even though the C—H bond is stronger than the C—C one, and the sputtering of particles with the same mass is always more efficient than between two atoms of different mass, the H atoms are linked to only one carbon atom whereas carbon is linked to up to 4 other carbon atoms. This means that the displacement energy of hydrogen is much smaller than the one of carbon. In fact, a study of the surface reactions during the erosion of a-CH films from ion bombardment [40] used with 25 eV and 2.5 eV for the values of the displacement energy of C and H respectively had good correspondence with experiments. It is hence assumed that the sputtering yield of H is ten times higher compared to the one of C.

As discussed above, most studies of a-CH deposition with acetylene plasmas show the importance of the radicals contribution to deposition. However, since the selected process has a lower working pressure than typical PECVD deposition, the ions may play a more significant role. As already seen in Fauroux et al. [16], ions reached densities comparable to radicals but their flux towards the substrate was more important, and more focused. Indeed, due to the unbalanced magnetic field, the electrons followed magnetic field lines passing through the center of the substrate; and due to ambipolar diffusion, ions were dragged in a beam after them [16,41]. Moreover, the plasma sheath surrounding the substrate accelerated ions to higher energies. Hence, the deposition mechanism in our process involves three parallel phenomena of a priori unknown relative importance: (i) reactive species created within the C_2H_2 rich plasma are bonding with the growing a-CH film preferably on available DB, (ii) ions impinging the substrate get absorbed at the films surface and can create DBs via chemical sputtering (iii) carbon atoms are sputtered to high energies towards the growing film and get deposited with high probability.

The aim of this study is to better understand the role of each surface reaction and deposition precursor, and to verify, if the model is generally coherent with observations. Based on all the above observations, we derived a set of the surface chemical reactions listed in Table 2 that are implemented in our simulation cases.

3. Results

3.1. Experimental results

Table 3 resumes the chemical composition obtained with ERDA/RBS measurement of five a-CH glassy carbon sample films deposited with 3.73% C_2H_2, at 100 mA for 90 min at different locations in the chamber.

As it can be seen, the composition of the films deposited on samples C1–C5 are quite similar and consist of around 66% carbon, 31% hydrogen, 2.5% oxygen impurity and 0.03% argon. These values of density and the composition are typical for films deposited with this technique and place these films in the “hard a-CH” category, as defined in Table 1 of Robertson [34]. Amorphous hydrogenated carbon films with this density and hydrogen content usually have a sp^3/sp^2 ratio of around 40%. Table 3 also reveals that there seems to be less hydrogen and more argon in the center sample than on the side ones; the differences are around 3% for hydrogen and 0.016% for argon, greater than the experimental errors of around 1.2% and 0.002% respectively. No significant variation of the density was observed.

Table 2
The surface reactions included in the model. The two surface states, a-C and a-C:H, represent the hydrogen-bounded amorphous carbon and the amorphous carbon with dangling bonds.

Surface before	Surface after	Impinging species	Released species	Probability
a-C	a-C:H	H	–	0.96154
a-C:H	a-C	H	H_2	0.03846
Any	a-C	C_2	–	0.7
Any	a-C	C	–	1
Any	a-C:H	CH	–	0.7
a-C	a-C:H	C_2H	–	1
a-C	a-C:H	C_4H_2	–	1
a-C	a-C:H	C_2H_3	–	1
a-C:H	a-C	C_2H	C_2H_2	0.1
a-C:H	a-C:H	C_2H	–	0.8
a-C:H	a-C	Ions	H/C	0.00797
Any	Any	Ions	–	1

Table 3
Elastic recoil detection analysis (ERDA) and Rutherford backscattering spectroscopy (RBS) of five a-CH glassy carbon sample films deposited with 3.73% C_2H_2, at 100 mA for 90 min. The samples vary in Y-position with C3 centered and each sample separated by 12 mm. The thicknesses were measured with a profilometer with uncertainties given by the standard deviation.

Sample	C (at. %)	H (at. %)	O (at. %)	Ar (at. %)	Thickness (nm)	Density (g/cm^3)
C1 (18, 30 mm)	62.5 ± 2.6	35.1 ± 1.5	2.4 ± 0.2	0.022 ± 0.002	415 ± 38	1.59 ± 0.06
C2 (6, 18 mm)	67.2 ± 2.6	30.4 ± 1.2	2.4 ± 0.1	0.033 ± 0.003	497 ± 49	1.57 ± 0.06
C3 (0mm)	66.4 ± 2.6	31.1 ± 1.2	2.5 ± 0.1	0.037 ± 0.001	593 ± 19	1.52 ± 0.06
C4 (−6, −18 mm)	67.6 ± 2.5	30.0 ± 1.1	2.4 ± 0.1	0.039 ± 0.002	508 ± 56	1.60 ± 0.06
C5 (−18, −30 mm)	64.8 ± 2.3	32.2 ± 1.3	2.9 ± 0.1	0.030 ± 0.004	434 ± 46	1.47 ± 0.05

In order to assess the sp^3 content, several Raman spectra were taken on one a-CH film deposited on a silicon substrate exposed under similar deposition conditions as for the C1-C5 samples. The baseline background signal was fitted with a quadratic polynomial and removed from the spectrum, and the spectrometer was calibrated on a diamond 1332 cm^{-1} sharp peak. Following the method recommended by Ferrari and Robertson [42], two peaks around 1580–1600 cm^{-1} and 1350 cm^{-1}, commonly referred to as the G and D peak, were fitted with two Gaussian functions for all spectra taken at different distances from the sample center. Fig. 3 shows the values obtained for the G peak shifts and the I_D/I_G ratios as filled ranges compared to the data points from Ferrari and Robertson [42], which correlate these two derived parameters to the corresponding sp^3/sp^2 ratio of a-CH films via electron-energy-loss spectroscopy (EELS) and to nuclear magnetic resonance (NMR) data from other works. For all spectra, the measured G peak shifts and the I_D/I_G ratios correspond to samples with between 40 and 50% of sp^3 bonds. The G peak shift decreases along with the distance from the sample center, as can be seen on Fig. 3a. This could be an indication that the nature of the film measured at different position differs, with relatively more sp^3 bonds at the center. However, this evolution was not observed for the I_D/I_G ratios, which did not vary that much.

Lastly, XPS measurements were performed at various positions of a silicon sample placed at position 5. Spectra for the C1s bonds and O1s were obtained before and after etching away the topmost surface layer (Fig. 4). No significant differences were found on the C1s spectra obtained at different positions on the sample. A typical C1s spectrum after etching is shown on Fig. 4a, together with the deconvolution obtained by assuming, as in Filik et al and Dwivedi et al. [43,44], that sp^2 and sp^3 bonds produce peaks at around 284.5 and 285.5 eV, respectively. Fitting the two peaks gave a ratio of 13% sp^3 and 87% sp^2 carbon bonds (Fig. 4a). Since a flood gun was used and the films are nonconductive, there could be an energy shift that would bias the spectrum fits and thus give an erroneous ratio. A third peak corresponding to the C—O bonds at an energy of around 287 eV was present as in Filik et al. [43], as there is a significant amount of oxygen in the films. The XPS technique only gives information on the surface layers of films which might be significantly different from the bulk structure. However, a similar proportion of oxygen was observed in the sample after Ar^+ bombardment with around 2.4%, according to ERDA/RBS measures (Table 3), and between 1% and 2% O1s bonds (Fig. 4b). The fact that the sp^3 and sp^2 bonds peak are really close and broad makes deconvoluting XPS spectra very

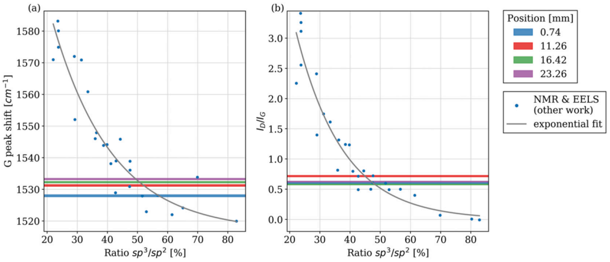

Fig. 3. G peak shift and I_D/I_G ratio vs sp^3 fraction for as-deposited a-C:H (data points taken from Ferrari and Robertson [42] and obtained via NMR and EELS measures) fitted with a decreasing exponential function (blue points and gray lines, respectively), as compared to the G peak shifts and I_D/I_G ratios measured on Si27 at different distances from the substrate center (colored ranges with widths corresponding to the fits standard error).

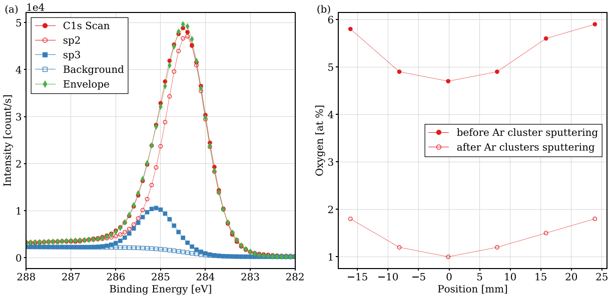

Fig. 4. Deconvoluted XPS C1s spectrum after 200 s of soft etching with Ar clusters from the middle of a sample a-CH deposited film (Si27) made with 3.73% C_2H_2, 100 mA and 90 min of deposition (a). XPS measure of the O1s bonds before and after soft etching with Ar clusters at various positions on the sample (b).

sensitive to experimental errors, and makes it a particularly unreliable test for the structure of amorphous carbon films [43]. Interestingly, as seen in Fig. 4b, a variation of the surface oxygen contamination with the position was noticed before and after soft etching of the sample surface with Ar^+ clusters.

In order to better understand of the deposition process, the deposition rate was measured at different positions, acetylene ratios, and powers, and compared with simulations predicted deposition rate for the same locations and conditions. The deposition rate versus location on the sample holder was evaluated by surface profilometry on a silicon sample for various acetylene ratios. Results are presented in Fig. 5, and the profiles were fitted with a centered scaled Gaussian distribution (A: amplitude, σ: standard deviation). The standard deviation decreases and the amplitude increases with the acetylene ratio.

3.2. Simulation results

The film deposition was simulated by defining two surface types along with several reactions, which can occur on each (Table 2). Four simulations with 20%, 15%, 10%, and 4% of C_2H_2 and a power of 0.8 W, and three simulations with a power of 0.6 W, 0.7 W and 0.9 W and 20% C_2H_2 were run for up to 750 μs. To reach an equilibrium for faster radical density, the simulations were all started from the final state of a previous simulation that had a C_2H_2 ratio of 4% and a power of 0.8 W, and a simulation time of 900 μs. Special simulation strategies were put in place to reduce the simulation time as described already in Fauroux et al. [16], like for example: (i) the simulation volume was partitioned in quads with different cell-sizing, run on individual CPUs in parallel, (ii) the number of real particles represented by one super-particle was optimized for each species and each quad, (iii) the final states of previous simulations was used as an initial state for other conditions, in order to bootstrap simulations. As an example, computation time for 670 μs of the 20% C_2H_2 and 0.8 W cases took around 500 h of calculations on a Tier-1 super-computer node using 21 CPUs and around 23 Gb of memory.

The film growth dynamics is modeled by defining two surface species, namely a-C and a-CH, which represent H terminated carbon sites and dangling bonds (DB) respectively (see Fig. 2). Each cell of the substrate surface contains a dynamic a-C coverage variable, which influences the adsorption of species and the probabilities of surface reactions. When the simulations were started with 0% DBs, the average a-C coverage increased linearly with time (Fig. 6a) with more DBs in substrate center. However, when started from 35% DBs on all the substrate, the average coverage decreased linearly (Fig. 6b). As seen in

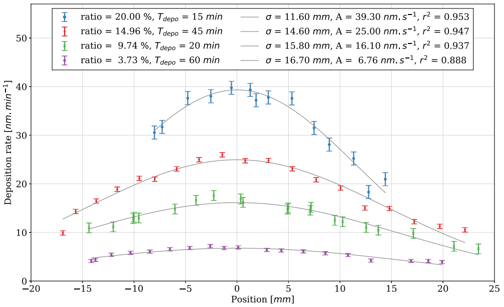

Fig. 5. Deposition profiles from profilometer measurements of a-CH films deposited on silicon substrates placed on a substrate holder placed 89 mm away from the cathode with various acetylene ratios, a fixed current of 100 mA, a graphite target, and an unbalanced magnetic field in DC mode at 0.6 Pa (5 mTorr).

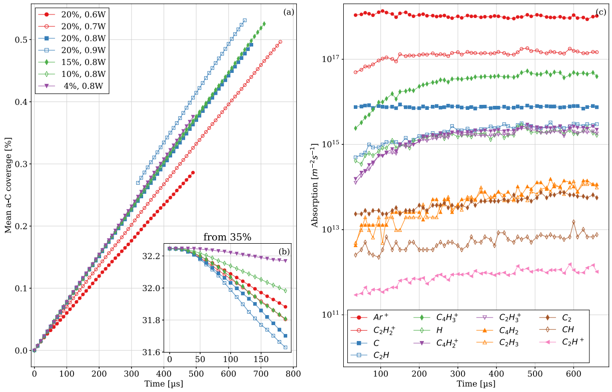

Fig. 6. Time evolution of the mean a-C coverage started from 0% in simulations with varying C_2H_2 ratio and discharge power (a) compared to simulations with the same parameters but started from 35% a-C (b). Time evolution of the maximum adsorption of all species onto the substrate for the simulation with 20% C_2H_2 and 0.8 W of power (c).

Fig. 6a, the discharge power seems to have more influence on the rate of evolution of the a-C coverage than the acetylene ratio when started from 0%. This observation is probably due to the fact that for a low surface density of DBs, the dominating effect on the a-C coverage is the chemical sputtering induced by the ion bombardment, whereof the flux is proportional to the discharge power as seen in the authors' previous study [16]. This dominant effect of the power is not seen in Fig. 6b, because in this case the main surface reaction affecting the a-C coverage is the attachment of radicals, which depends on the radical density, which itself depends on the discharge power but also on the C_2H_2 ratio. Due to the fact that the coverage evolves slowly, it was not possible to attain this equilibrium in a reasonable computation time. However, two competing mechanisms have been identified and since they do not directly affect each other, a surface state equilibrium must exist for every acetylene ratio and discharge power in between 0% and 35%.

Fig. 6c represents the adsorption of every species averaged over the entire substrate along time for one simulation with 20% C_2H_2 and 0.8 W. For most species, the adsorption stabilized after several hundred microseconds. However, the C_4H_2 and C_2H_3 species adsorption seemed to be linearly increasing in all simulation at a constant rate. In fact, C_4H_2 and C_2H_3 are mono-radicals which are able to deposit only on DB sites, thus their adsorption evolves due to the increase availability of DBs, which also evolve at a constant rate (Fig. 6a and c). Extrapolating the adsorption of those species to predict their contribution to film growth when the surface state would have stabilized, made their contribution comparable to that of the sputtered carbon (around 10^{15}–10^{16} m^{-2} s^{-1}), thus non-neglectable. For more precision on the extrapolation procedure see supplementary material, Appendix B.

To obtain the deposition rates, the total C and H absorption was calculated by summing up the atomic compositions of all the adsorbed and desorbed species. The conversion from an adsorption in $m^{-3} s^{-1}$ to a deposition rate in nm s^{-1} was performed assuming a density of the deposited films of 1.55 g cm^{-3} (Table 3). Fig. 7 represents the predicted deposition rate for all simulations with and without the correction due to C_4H_2 and C_2H_3 adsorption. There is a linear relationship between the deposition rate and the discharge power, as well as with the C_2H_2 ratio. The effect of including the correction due to the mono-radicals is small but non-neglectable, with a variation of nearly 40% for the simulation with 0.9 W and 20% of C_2H_2. In Fauroux et al. [16] we demonstrate that there is a linear relationship between the reactive species concentration next to the substrate and the discharge power as long as the density of reactive species remains small compared to the background C_2H_2 density. Based on the fit of the deposition rate relation to power at a fixed ratio (Fig. 7a), deposition rates were extrapolated to the experimental discharge power (around 50 W for every film of Fig. 5). Despite high uncertainty, the resulting deposition rates are close in absolute values to the experimental ones and they show a similar dependency on the C_2H_2 ratio (Fig. 7c).

The relative contribution to the deposition profile of every species is shown in Fig. 8a for a simulation with 20% acetylene at 0.8 W after 670 μs of simulation with a substrate initially covered with 0% a-C coverage. To obtain these profiles, the adsorption and desorption of every species were averaged over time, and over half circles of 1 mm thickness with a radius going from 0 to 30 mm, with a sign given by the sign of the y-axis coordinate (vertical axis as given in Fig. 1). The main source of carbon and hydrogen atoms for the film deposition, $C_2H_2^+$ exhibit a V-shaped profile with a maximum at the center of the sample, aligned with the center of the cathode. The second contributor, $C_4H_3^+$ with around 10 times less flux, has a flatter profile. This flatter profile comes from the fact that the $C_4H_3^+$ mostly originates from the recombination of $C_2H_2^+$ with the background acetylene, which means that it is created within the chamber and thus propagates in a less focused manner than the ions originating from the plasma bulk. Similar profiles can be seen for the $C_4H_2^+$, and $C_2H_3^+$ ions. Following in importance is the atomic carbon, emerging from the target sputtering. Even though there is around 50 times less C adsorbed in the center of the substrate than $C_2H_2^+$, the C adsorption profile is much flatter as was already noticed in Fauroux et al. [16], and thus becomes more important relative to $C_2H_2^+$ further from the center. All the other species contribution to the film deposition are less than 100 times smaller in magnitude. The C_4H_2 and C_2H_3 adsorption profiles in Fig. 6 correspond to the predicted adsorption profiles at equilibrium, as they have been multiplied by 367 and 540 respectively, according to the calculated correction for the coverage discussed above and detailed in the supplementary material, Appendix B.

The desorption profiles of particles from the substrate, obtained in a similar manner as the adsorption one, is presented in Fig. 8b. The desorption of H_2 and C_2H_2 originates from the recombination at the surface of H and C_2H and thus follows the adsorption profiles of these two species. The desorbed C and H atoms are the consequence of chemical sputtering, which in our model occurs on ion impingement without requiring the presence of a simultaneous H flux. This is why they follow the profile shape of the ions (in particular the one of Ar^+). In reality, the chemical sputtering probably does not produce C and H but hydrocarbon molecules. However, as explained in the description of the surface deposition model, the chosen 1/10 ratio between the chemical sputtering of C and H was based on their displacement energy, as a similar assumption was made with success in another study [40]. The desorption profiles were relatively small compared to adsorption ones, and the predicted deposition rates were important in all cases.

Another available test for the deposition model is the hydrogen content of the produced films. A sum of all adsorbed and desorbed hydrogen and carbon atoms from a simulation with 4% C_2H_2 and 0.8 W was compared to the film compositions measured in the ERDA/RBS experiment (Table 3), and the resulting hydrogen ratios are shown in

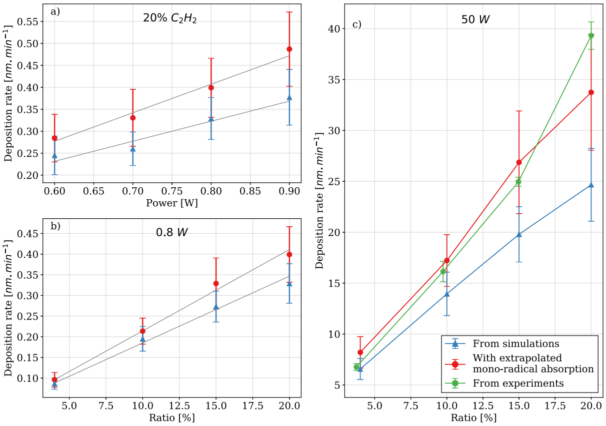

Fig. 7. Predicted maximum deposition rates (blue triangles), without and with extrapolated radicals' contribution (red circles) for: (a) simulations with 20% C_2H_2 and varying power, (b) simulations at 0.8 W and varying C_2H_2 ratio, (c) and deposition rates extrapolated for 50 W, compared with experimental deposition rates. The error bars are the standard deviations of the averaged deposition rates for the simulation and of the roughness of films for the profilometer measurements.

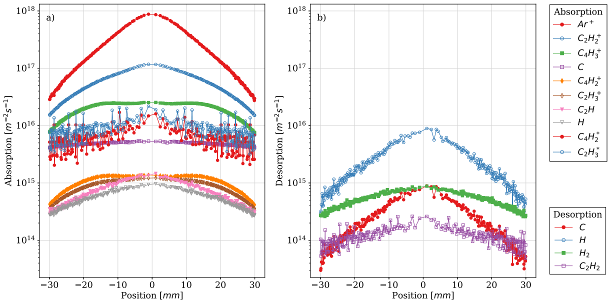

Fig. 8. Mean adsorption (a) and desorption (b) profiles of the main species onto and from the substrate in a simulation with 20% acetylene at 0.8 W with a substrate initially covered with a-CH after 1300 μs of simulation. The star (*) in C_4H_2* and C_2H_3* marks that their adsorption has been extrapolated at the a-C coverage equilibrium.

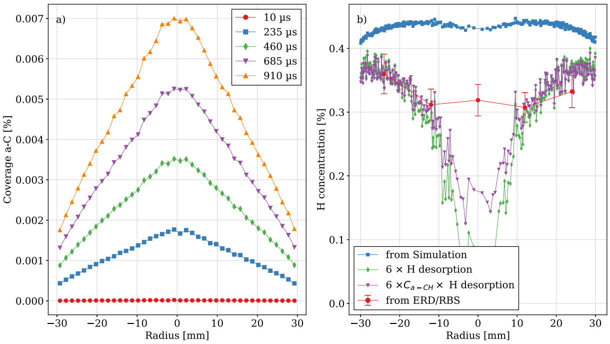

Fig. 9. a-C Coverage (or ratio of DBs) at different timesteps (a) and hydrogen concentration in the simulation with 4% C_2H_2 at 0.8 W (b) with: the average H content in the simulation (blue squares), the hydrogen content in experimentally deposited films from ERDA/RBS measurements (red circles), the hydrogen concentration if the removal of hydrogen from ion impact had a probability multiplied by 6 (green diamonds), and the hydrogen concentration considering the effect of the diminished probability of H desorption in substrate center (purple triangles).(colors online).

Fig. 9. The ratio of hydrogen was around 45% in the simulation, with a slight increase in concentration towards the substrate's center, whereas it seemed lower (around 35%) in the ERDA/RBS measures and had a lower H content in the center than on the sides. This difference cannot be explained by the difference in discharge power since the ion and H fluxes were demonstrated to scale linearly in Fauroux et al. [16]. A possible source of this discrepancy is the fact that the model used for the calculation of the probability of desorption of hydrogen from low-energy ion bombardment within hydrogen rich gas, taken from Hopf et al. [29], was made for higher ion energies (from 20 eV to 800 eV) and higher hydrogen flux ($j_H/j_{Ar+} > 100$). The value given by the model is therefore a rough approximation since the ions mean energy varies in the simulation from 2 eV to 4 eV, and the j_H/j_{Ar+} flux ratio from 0.002 to 0.014. Additionally, these reactions had a fixed probability of 0.00797 in the simulations, but our model could be refined by having this relation to depend on the dynamically calculated j_H/j_{Ar+} ratio and the impinging ions energy. In fact, adjusting the hydrogen chemical sputtering a posteriori by multiplying the H desorption by 6 (green diamonds in Fig. 9) gives an H concentration closer to the experimental one for most data points, except for the central one. Another thing to take into consideration is the fact that the equilibrium for the coverage was far from being reached, and the desorption of H depends on the a-C/a-CH ratio. According to the extrapolations showed in Figs. 6 and 7, the mean a-C coverage should be around 18% in this simulation, and the a-C coverage varies strongly with the distance from the center, with more a-C in the center (Fig. 9a). This means that the desorption of hydrogen would be lower in the substrate center if the simulations could be run until the equilibrium for the coverage was reached. Hence, if we assume that the

probability of H to be desorbed from the film due to ion bombardment is 6 times higher, and take into account the effect of reduced desorption in the substrate's center due to the high a-C coverage, an H concentration that better matches the one from the ERDA/RBS measurements could be obtained (downward pointing triangles in Fig. 9b).

Finally, the resulting predicted deposition profiles at equilibrium were normalized and compared with profilometers given deposition rate profiles (Fig. 10). Interestingly, all relative deposition rate profiles match regardless the acetylene ratio and discharge power.

3.3. *Discussion*

This work is focused on clarifying the questions of the composition, density and structure of the films in order to better refine a deposition model of a-C:H and its predictions. Variations of the precursor fluxes across the substrate were observed in the authors' previous study [16], thus the corresponding variations of the structure were expected at different distances from the sample center. Indeed, we observed both the variation in the hydrogen and argon content from the ERDA/RBS result and the variation of the surface oxygen contamination from the XPS measurements, as well as a possible sp^2/sp^3 variation from the Raman analysis. The oxygen contamination varied in both the XPS and ERDA measurements, with less oxygen in the substrate center. It could be linked to a variation in the film structure with, for example, less porosity in the center due to the higher ion flux. The oxygen absorption of a-CH films was measured by Yun et al. [45] and they found that the oxygen uptake at atmospheric pressure in air is around 6% but that the films are relatively inert from oxidation with only a $\sim 10^{-6}$ sticking coefficient for O_2. However, no significant variation of the density was observed within the error, which was mainly due to roughness and thickness variation over 12 mm wide samples.

With our simulations, we demonstrate that the most important film growth mechanisms are related to $C_2H_2^+$ and $C_4H_3^+$ ions fluxes. This observation is quite unusual since most a-CH deposition processes as described in literature primarily rely either on the radical adsorption or on the hydrocarbon ions subplantation which can occur, and is mainly due to the application of substrate bias [25,28]. However, since the predicted ions densities have been confirmed experimentally in Fauroux et al. [16] and since no other flux can explain the observed high deposition rate, one must conclude that the most important deposition precursor is probably $C_2H_2^+$. Another confirmation of this hypothesis is the fact that the radical adsorption profiles have a different shape across the substrate than the triangular shape of the ions adsorption profile in the simulation and the observed film thickness profiles (see Figs. 8 and 10). One possible explanation of the $C_2H_2^+$ high sticking is the fact that molecular ions in reactive plasmas can carry a lot of internal energy, which can ease the adsorption process [46]. It is interesting to note the high contribution of $C_4H_3^+$ to the deposition process; the importance of heavy ions carrying high internal energy has already been reported by Michelmore et al. [46]. Another interesting feature is the density/flux profiles difference between various species, with a flat profile for sputtered carbon, a Gaussian for first-order radicals and ions, and a double-hump shape for second order radicals and ions. These differences have already been discussed in Fauroux et al. [16], but the relative profile of the deposition rate match in Fig. 10 is yet another confirmation of the role of $C_2H_2^+$. Other species like the lighter ions C^+, C_2^+, H^+, H_2^+, CH^+ and the C_2H^- anion, as well as the highly reactive C_3H^+ and C_3^+, not included in our model may play a role, but in much smaller quantities than the C_2H^+ or $C_2H_3^+$ ions. The CH_2 as well as all hydrocarbons with more than four carbon atoms where ignored, but their effect should have been comparable to that of the included radicals, like the C_2H or C_4H_2. Most studies of PECVD systems with an acetylene precursor consider the C_2H radical as the most important species for deposition, but due to the lower pressure, its role in our simulation was minor. The quantity of C_2H was probably slightly underestimated as the reaction $e + C_2H_2 \rightarrow C_2H + H^+ + 2e$ was impossible to include without also including H^+. But even doubling the C_2H density would not change its impact on deposition. However, the principal distinctiveness of the method of deposition we used are the usage of an unbalanced magnetic field and the very low pressure (<1 Pa), which causes the ions to come towards the substrate in a high flux.

At higher pressures, we would have a higher number of radicals, and also a higher frequency of polymerization reactions and the creation of higher-order molecules finally leading to dust formation. Therefore, the fact that this low-pressure process does not have much issues with dust formation and produces smooth a-CH films [47] could be explained by the fact that most ions ($C_2H_2^+$, etc.…) get adsorbed at walls (thereby performing deposition) before they can create a high number of higher-order molecules.

Besides the deposition rate variability, the highest source of inaccuracy was the extrapolation made on the DB coverage and its consequence on the deposition rate. Unfortunately, simulation times of tenths

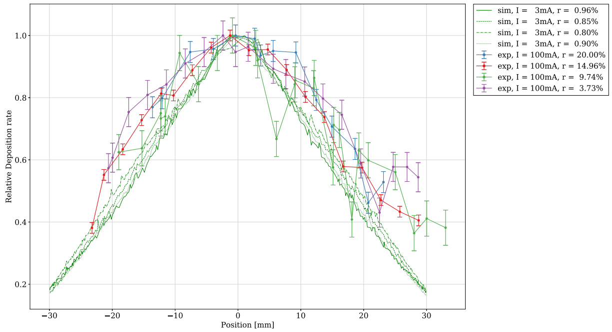

Fig. 10. Relative deposition rate of a-CH for various ratio from experiments (markers) and simulations (green curves) with respect to the distance from the sample center. The values given in the legend are respectively: (i) the data source, (ii) the discharge current, (iii) the acetylene ratio.

of milliseconds are very hard to reach with the PIC-MC simulations, and the speed at which the coverage can evolve is bounded by the size of surface bonds, which cannot be too large for numerical correctness. Two hypotheses were made to bypass these limits: (i) that the principal effect of the increasing a-C coverage was the increasing adsorption of the mono-radicals like C_4H_2 and C_2H_3, (ii) that the a-C coverage which increased from 0% and decreased from 35% would reach an equilibrium precisely where the two fitted lines cross (see Appendix B). The first hypothesis neglects the impact of the a-C coverage on other species like H. The second hypothesis introduced, as already discussed, an important error for the extrapolated deposition of mono-radicals. However, the effect of including this correction was relatively small compared to the ion contribution, hence the error was still dominated by the deposition rate variability, stemming from plasma fluctuations fueled by the rotation of "spokes" [16,48,49].

The hydrogen concentration in the simulated films was around 45%, whereas the ERDA/RBS revealed concentrations around 35% in experimental conditions. This result does not contradict the deposition mechanisms included in the model, as a slight variation of the probability of hydrogen to be sputtered by ion impact (multiplying it by 6, Fig. 9b) already improves the match significantly. In fact, as explained in Section 2.4, the value for this probability was obtained by using an extrapolation of an empirical model, which was tested in Hopf et al. [29] with only Ar^+ from 20 eV to 800 eV and with a J_H/J^+_{Ar} of 0.5 up to 500. But in our simulation, the energy is around 2 to 4 eV and the ratio close to 1×10^{-2}. Additionally, this probability was used for every ion, which is questionable. However, to the authors' knowledge, the exact value of this reaction probability is not available in literature, especially since it probably depends on the particular film structure and ions kinetic and internal energies. Only direct measurement of the H yield in similar conditions could give more precise information on this probability. Nonetheless, the advantage of having such a model is that it is now possible to apply the same technique as demonstrated in Fig. 9b, and fine-tune the parameters by experimentally comparing deposited films with simulated ones, and incrementally tend towards more precise reaction probabilities.

The crucial physical parameters which determine the physical properties of amorphous hydrogenated carbon films are their hydrogen content, density and ratio of carbon atoms bond hybridization (sp^2/sp^3) [8]. The deposition of a-CH from reactive plasmas with an acetylene precursor can produce hard films if the sp^3/sp^2 ratio is high and the H-content is low. Otherwise, the films have a polymeric nature, which is often less suitable for industrial applications. A simple way to ensure that the deposited films are of a hard DLC nature is to apply an adjusted bias to the substrates. The ions with more energy will be subplanted, raising the density and lowering the H-content through sputtering [9]. However, no bias was applied in our simulation and experiments to simplify simulations and promote higher variability since biased deposition tends to produce more homogenous films [5]. Nonetheless, the ERDA/RBS, XPS, and Raman analyses confirmed that the films produced with this particular technique are indeed hard a-CH with around 40% hydrogen and 50% sp^3 hybridized carbon, as defined by Robertson [34]. The average ion energy impinging on the substrate was around 2–4 eV (see the Appendix) in the simulations, which was close to the plasma potential in the vicinity of the substrate. At such energies, only the presence of dangling hydrogen bonds can explain the formation of tetrahedral carbon [36]. These two bonds formation mechanisms, included in our simulations, were the hydrogen chemical etching and the ions chemically enhanced etching, as described by Hopf et al. [29], which can operate even at low energy. The latter reaction played the most significant role as the densities of ions reaching the substrate dominate in a unbalanced magnetron PECVD deposition at very low pressure (below 1 Pa), as previously shown in Fauroux et al. [16].

4. Conclusions

In this study, we setup a PIC-MC simulation model which describes the PECVD of a-CH from a low pressure Ar/C_2H_2 gas mixture in a magnetron plasma reactor. We used a small 3D chamber, a self-coherent but simplified PCR, and several numerical optimizations (presented in Fauroux et al. [16]). Many simulations with varying C_2H_2 ratio, power and initial a-C coverage were run with a highly optimized and parallelized code [50] on a Tiers-1 cluster. It was possible to run the PIC-MC simulations for sufficiently long times to reach an equilibrium for all products densities and for extrapolating the evolution of the DB coverage. This enabled us to predict the radicals contribution to the deposition at equilibrium. This extrapolation, together with the power scaling, enabled us to qualitatively and quantitatively predict the deposition rates at several locations of the substrate holder and their evolution with the C_2H_2 ratio. We showed that there are three main contributions to the film deposition, which are, sorted by importance: (1) the ion bombardment, (2) the reactive radicals' surface reactions, (3) the carbon atom sputtering. Our simulations reproduced several results of previous experimental studies [6,51], including the linear increase of the deposition rate and of the hydrogen content with the acetylene ratio. Our results could explain the experimental observations of the decrease in hardness and sp^3 content with increasing C_2H_2 ratio, as it corresponds to the passage from an ion-dominated to a radical-dominated deposition.

The good agreement observed between the measured and simulated deposition rates for different acetylene ratios and discharge powers in Figs. 7c and 10, means that our model satisfactorily describes the plasma phase and film growth. This method of comparing the predicted deposition rates and film structures to experimental ones on long samples (6 cm) for many different discharge conditions in a small chamber is an innovative way to test PIC-MC simulations. It enabled us to get more insight on the species involved and to validate the discharge behaviour, charged particle transport, and C_2H_2 PCR; and it could be transposed easily to similar or more complex deposition processes.

These simulations are, to the authors' best knowledge, the first 3D PIC-MC ones to be run until equilibrium is reached for all species densities with this many species in a self-coherent PECVD chemistry and a dynamic surface model, and one of the few able to give quantitative predictions for relevant experimental conditions. However, the problem of high uncertainty in surface reaction probabilities remains, and more comparisons between the simulation predictions and the experiments are needed to improve our knowledge of these reactions. Another approach to refine the model would be to use the fluxes of particles extracted from these simulations as inputs for the atomistic film growth simulations, like molecular dynamics (MD) or kinetic Monte-Carlo (kMC).

CRediT authorship contribution statement

A. Fauroux: Conceptualization, Methodology, Investigation, Writing – original draft, Visualization. **A. Pflug:** Conceptualization, Supervision, Writing – review & editing, Project administration, Funding acquisition. **S. Lucas:** Conceptualization, Writing – review & editing, Supervision, Project administration, Funding acquisition.

Declaration of competing interest

The authors declare that they have no known competing financial interests or personal relationships that could have appeared to influence the work reported in this paper.

Acknowledgments

The authors A. Fauroux and S. Lucas gratefully acknowledge the financial support of the Walloon region under the FEDER and

3DCOATER-5: Convention N° 1610258, project 3215. The present research benefited from computational resources made available on the Tier-1 supercomputer of the “Fédération Wallonie-Bruxelles”, infrastructure funded by the Walloon region under the grant agreement n°1117545. It was also part of the “DLCplus” project (IGF 230 EN) under the Convention SPW n°1710252, CORNET CALL. The authors gratefully acknowledge the contribution of J. Colaux and the SIAM platform, who performed the ERDA/RBS measurements and the contribution of A. Felten from the LISE laboratory from the University of Namur for the XPS measures. The authors would also like to thank the Diarotech company for the usage of their Raman spectrometer.

Appendix A. Supplementary data

Supplementary data to this article can be found online at https://doi.org/10.1016/j.surfcoat.2021.127472.

References

[1] J. Robertson, Diamond-like carbon films, properties and applications, Compr. Hard Mater. 3 (2014) 101–139, https://doi.org/10.1016/B978-0-08-096527-7.00043-X.

[2] M. Joe, M.W. Moon, K.R. Lee, Atomistic simulations of diamond-like carbon growth, in: Thin Solid Films, Elsevier, 2012, pp. 239–244, https://doi.org/10.1016/j.tsf.2011.11.060.

[3] D. Sheeja, B.K. Tay, K.W. Leong, C.H. Lee, Effect of film thickness on the stress and adhesion of diamond-like carbon coatings, Diam. Relat. Mater. 11 (2002) 1643–1647, https://doi.org/10.1016/s0925-9635(02)00109-7.

[4] Y. Hirata, J. Choi, Deposition of a-C:H films on inner surface of high-aspect-ratio microchannel, J. Appl. Phys. 120 (2016), 065305, https://doi.org/10.1063/1.4960694.

[5] A. Grill, B. Meyerson, V. Patel, Interface modifications for improving the adhesion of a-C:H films to metals, J. Mater. Res. 3 (1988) 214–217, https://doi.org/10.1557/JMR.1988.0214.

[6] D. Thiry, A. De Vreese, F. Renaux, J.L. Colaux, S. Lucas, Y. Guinet, L. Paccou, E. Bousser, R. Snyders, Toward a better understanding of the influence of the hydrocarbon precursor on the mechanical properties of a-C:H coatings synthesized by a hybrid PECVD/PVD method, Plasma Process. Polym. 13 (2016) 316–323, https://doi.org/10.1002/ppap.201500050.

[7] P. Yang, C.C. Sung, Y.K. Fuh, C.L. Chu, C.H. Lo, Ti-containing hydrogenated carbon films fabricated by high-power plasma magnetron sputtering, Trans. Nonferrous Met. Soc. China (English Ed. 22 (2012) 1381–1386, https://doi.org/10.1016/S1003-6326(11)61329-0.

[8] P. Yi, L. Peng, T. Zhou, J. Huang, X. Lai, Composition optimization of multilayered chromium-nitride-carbon film on 316L stainless steel as bipolar plates for proton exchange membrane fuel cells, J. Power Sources 236 (2013) 47–53, https://doi.org/10.1016/j.jpowsour.2013.02.034.

[9] E. Bertran, C. Corbella, A. Pinyol, M. Vives, J.L. Andújar, Comparative study of metal/amorphous-carbon multilayer structures produced by magnetron sputtering, Diam. Relat. Mater. 12 (2003) 1008–1012, https://doi.org/10.1016/S0925-9635(02)00303-5.

[10] P. Patsalas, S. Logothetidis, P.C. Kelires, Surface and interface morphology and structure of amorphous carbon thin and multilayer films, Diam. Relat. Mater. 14 (2005) 1241–1254, https://doi.org/10.1016/J.DIAMOND.2004.12.039.

[11] K. Nygren, M. Samuelsson, A. Flink, H. Ljungcrantz, Å. Kassman Rudolphi, U. Jansson, Growth and characterization of chromium carbide films deposited by high rate reactive magnetron sputtering for electrical contact applications, Surf. Coat. Technol. 260 (2014) 326–334, https://doi.org/10.1016/j.surfcoat.2014.06.069.

[12] V. Singh, P. Dowben, I. Ketsman, J. Colon-Santana, Y. Losovyj, V. Palshin, Chromium doped Diamond-Like carbon, 12/590,524, 2009.

[13] L. Yang, A. Neville, A. Brown, P. Ransom, A. Morina, Friction reduction mechanisms in boundary lubricated W-doped DLC coatings, Tribol. Int. 70 (2014) 26–33, https://doi.org/10.1016/J.TRIBOINT.2013.09.020.

[14] D. Zhang, P. Yi, L. Peng, X. Lai, J. Pu, Amorphous carbon films doped with silver and chromium to achieve ultra-low interfacial electrical resistance and long-term durability in the application of proton exchange membrane fuel cells, Carbon N. Y. 145 (2019) 333–344, https://doi.org/10.1016/j.carbon.2019.01.050.

[15] Y. Miyagawa, H. Nakadate, M. Tanaka, M. Ikeyama, S. Nakao, S. Miyagawa, PIC simulation of N2 and C2H2 plasma behavior around plural objects, Surf. Coat. Technol. 201 (2007) 8414–8419, https://doi.org/10.1016/j.surfcoat.2006.03.067.

[16] A. Fauroux, C. Vandenabeele, A. Pflug, S. Lucas, Experimental and theoretical study of a magnetron DC-PECVD acetylene discharge: determination of the main species and reactions taking place in the plasma, Surf. Coat. Technol. 400 (2020), 126195, https://doi.org/10.1016/j.surfcoat.2020.126195.

[17] J. Benedikt, Plasma-chemical reactions: low pressure acetylene plasmas, J. Phys. D. Appl. Phys. 43 (2010) 43001, https://doi.org/10.1088/0022-3727/43/4/043001.

[18] R. Tonneau, P. Moskovkin, A. Pflug, S. Lucas, TiOx deposited by magnetron sputtering: a joint modelling and experimental study, J. Phys. D. Appl. Phys. 51 (2018), 195202, https://doi.org/10.1088/1361-6463/aabb72.

[19] E. Oyarzabal, R.P. Doerner, M. Shimada, G.R. Tynan, Carbon atom and cluster sputtering under low-energy noble gas plasma bombardment, J. Appl. Phys. 104 (2008), https://doi.org/10.1063/1.2968549.

[20] Y. Yamamura, T. Takiguchi, M. Ishida, Energy and angular distributions of sputtered atoms at normal incidence, Radiat. Eff. Defects Solids 118 (1991) 237–261, https://doi.org/10.1080/10420159108221362.

[21] M.-Y. Song, J.-S. Yoon, H. Cho, G.P. Karwasz, V. Kokoouline, Y. Nakamura, J. Tennyson, Cross sections for electron collisions with hydrogen molecules, J. Phys. Chem. Ref. Data 37 (2008) 913–931, https://doi.org/10.1063/1.2838023.

[22] M. Tsuji, H. Kouno, K. Matsumura, T. Funatsu, Y. Nishimura, H. Obase, H. Kugishima, K. Yoshida, Dissociative charge-transfer reactions of Ar + with simple aliphatic hydrocarbons at thermal energy, J. Chem. Phys. 98 (1993) 2011–2022, https://doi.org/10.1063/1.464234.

[23] R.K. Janev, D. Reiter, Collision processes of C2,3Hy and C2,3Hy+ hydrocarbons with electrons and protons, Phys. Plasmas 11 (2004) 780–829, https://doi.org/10.1063/1.1630794.

[24] E.D. De Rooij, A.W. Kleyn, W.J. Goedheer, Sticking of hydrocarbon radicals on different amorphous hydrogenated carbon surfaces: a molecular dynamics study, Phys. Chem. Chem. Phys. 12 (2010) 14067–14075, https://doi.org/10.1039/c0cp00637h.

[25] Y. Lifshitz, S.R. Kasi, J.W. Rabalais, W. Eckstein, Subplantation model for film growth from hyperthermal species, Phys. Rev. B. 41 (1990) 10468–10480, https://doi.org/10.1103/physrevb.41.10468.

[26] Y. Miyagawa, H. Nakadate, M. Ikeyama, S. Nakao, S. Miyagawa, Dynamic MC simulation for a-C:H deposition in methane plasma based on subplantation model, Diam. Relat. Mater. 12 (2003) 927–930, https://doi.org/10.1016/S0925-9635(02)00223-6.

[27] J. Robertson, The deposition mechanism of diamond-like a-C and a-C: H, Diam. Relat. Mater. 3 (1994) 361–368, https://doi.org/10.1016/0925-9635(94)90186-4.

[28] J. Benedikt, Acetylene Chemistry in Remote Plasmas: Implications for the a-C:H Growth Mechanism, 2004, https://doi.org/10.6100/IR581182.

[29] C. Hopf, A. von Keudell, W. Jacob, A. Von Keudell, W. Jacob, A. von Keudell, W. Jacob, Chemical Sputtering of Hydrocarbon Films by Low-Energy Ar Ion and H Atom Impact, IOP Publishing, 2002, https://doi.org/10.1088/0029-5515/42/12/101.

[30] A. Von Keudell, M. Meier, C. Hopf, Growth mechanism of amorphous hydrogenated carbon, Diam. Relat. Mater. 11 (2002) 969–975, https://doi.org/10.1016/S0925-9635(01)00553-2.

[31] A. Von Keudell, Surface processes during thin-film growth, Plasma Sources Sci. Technol. 9 (2000) 455–467, https://doi.org/10.1088/0963-0252/9/4/302.

[32] J.T. Gudmundsson, D. Lundin, Introduction to Magnetron Sputtering, 2019, https://doi.org/10.1016/B978-0-12-812454-3.00006-1.

[33] I. Solomon, M. Bhatnagar, K. Shukla, B. Sarma, M. Ranjan, A. Sarma, Correlation of structural and optical properties of PVD grown amorphous carbon thin films, Diam. Relat. Mater. 75 (2017) 69–77, https://doi.org/10.1016/j.diamond.2017.01.015.

[34] J. Robertson, Diamond-like amorphous carbon, Mater. Sci. Eng. R. Rep. 37 (2002) 129–281, https://doi.org/10.1016/S0927-796X(02)00005-0.

[35] C. Hopf, T. Schwarz-Selinger, W. Jacob, A. Von Keudell, A. Von Keudell, Surface loss probabilities of hydrocarbon radicals on amorphous hydrogenated carbon film surfaces, J. Appl. Phys. 87 (2000) 2719–2725, https://doi.org/10.1063/1.372246.

[36] E. Neyts, Mathematical Simulation of the Deposition of Diamond-Like Carbon (DLC) Films, Antwerpen University, 2006.

[37] E. Neyts, A. Bogaerts, R. Gijbels, J. Benedikt, M.C.M. Van De Sanden, Molecular dynamics simulation of the impact behaviour of various hydrocarbon species on DLC, Nucl. Instruments Methods Phys. Res. Sect. B Beam Interact. with Mater. Atoms. 228 (2005) 315–318, https://doi.org/10.1016/j.nimb.2004.10.063.

[38] R. Mohan, A. Bogaerts, E. Neyts, M. Mao, M. Eckert, A. Bogaerts, M. Mao, M. Eckert, R. Mohan, A. Bogaerts, E. Neyts, M. Mao, M. Eckert, A. Bogaerts, M. Mao, M. Eckert, Plasma Processing of Nanomaterials, 2011, https://doi.org/10.1201/b11473.

[39] M. Meier, A. Von Keudell, Hydrogen elimination as a key step for the formation of polymerlike hydrocarbon films, J. Appl. Phys. 90 (2001) 3585–3594, https://doi.org/10.1063/1.1397285.

[40] W. Jacob, Surface reactions during growth and erosion of hydrocarbon films, Thin Solid Films 326 (1998) 1–42, https://doi.org/10.1016/S0040-6090(98)00497-0.

[41] A. Fridman, Plasma Chemistry, 2008, https://doi.org/10.1017/CBO9780511546075.

[42] A. Ferrari, J. Robertson, Interpretation of Raman spectra of disordered and amorphous carbon, Phys. Rev. B - Condens. Matter Mater. Phys. (2000), https://doi.org/10.1103/PhysRevB.61.14095.

[43] J. Filik, P.W. May, S.R.J. Pearce, R.K. Wild, K.R. Hallam, XPS and laser Raman analysis of hydrogenated amorphous carbon films, Diam. Relat. Mater. 12 (2003) 974–978, https://doi.org/10.1016/S0925-9635(02)00374-6.

[44] N. Dwivedi, S. Kumar, H.K. Malik, C.M.S. Rauthan Govind, O.S. Panwar, Correlation of sp 3 and sp 2 fraction of carbon with electrical, optical and nano-mechanical properties of argon-diluted diamond-like carbon films, Appl. Surf. Sci. 257 (2011) 6804–6810, https://doi.org/10.1016/j.apsusc.2011.02.134.

[45] Y. Yun, X. Ma, J. Gui, E. Broitman, A.J. Gellman, Oxidation kinetics of hydrogenated amorphous carbon (a-CHx) overcoats for magnetic data storage media, Langmuir. 23 (2007) 5485–5490, https://doi.org/10.1021/la062104e.

[46] A. Michelmore, J.D. Whittle, J.W. Bradley, R.D. Short, Where physics meets chemistry: thin film deposition from reactive plasmas, Front. Chem. Sci. Eng. 10 (2016) 441–458, https://doi.org/10.1007/s11705-016-1598-7.

[47] V. De Vriendt, S.M. Miladinovic, J.L. Colaux, F. Maseri, C.L. Wilkins, S. Lucas, Growth mechanisms involved in the synthesis of smooth and microtextured films

by acetylene magnetron discharges, Langmuir. 27 (2011) 8913–8922, https://doi.org/10.1021/la2003035.

[48] R. Tonneau, A. Pflug, S. Lucas, Magnetron sputtering: determining scaling relations towards real power discharges using 3D Particle-In-Cell Monte Carlo models, Plasma Sources Sci. Technol. (2020), https://doi.org/10.1088/1361-6595/abb3a0.

[49] A. Anders, P. Ni, J. Andersson, Drifting ionization zone in DC magnetron sputtering discharges at very low currents, IEEE Trans. Plasma Sci. 42 (2014) 2578–2579, https://doi.org/10.1109/TPS.2014.2334601.

[50] C. Schwanke, A. Pflug, M. Siemers, B. Szyszka, Parallel Particle-in-Cell Monte-Carlo Algorithm for Simulation of Gas Discharges under PVM and MPI, Lect. Notes Comput. Sci., Springer, Berlin, Heidelberg, 2012, pp. 213–219, https://doi.org/10.1007/978-3-642-28151-8_21.

[51] V. De Vriendt, S.M. Miladinovic, J.L. Colaux, F. Maseri, C.L. Wilkins, S. Lucas, Growth mechanisms involved in the synthesis of smooth and microtextured films by acetylene magnetron discharges, Langmuir. 27 (2011) 8913–8922, https://doi.org/10.1021/la2003035.

Appendix A: Extracted fluxes

One of the advantages of having a self-contained 3D simulation of the whole plasma reactor is that fluxes of all species impinging surfaces can be extracted with great details. In general, information on the nature of the deposition precursor, their energy and angular distributions are quite complex to obtain experimentally and often only partial information can be obtained. The effect of the power on the angular and energetic distributions of the particles impinging the substrate was quite mild within the range of this study, and the differences came mainly from the specificities of the species themselves and the position of the sampling. In order to understand how the deposition conditions varied across the substrate, the impinging particles were counted inside a 10 mm thick disk in front of the substrate and divided in three groups: with C1, C2, and C3 corresponding to $r \in [0,6]$, $[6,18]$, $[18,30]$ mm respectively (Figure 11). The angular distribution of most species tended to be predominantly going outward as the brightest angular sectors are with $\theta > 0$ and $\varphi \in [-90, 90]$ (with θ and φ the incidence and orientation angles respectively). This is more visible for ions since their angular distribution are more focused. Additionally, the incidence angles of most species augment with the distance from the center, probably because most of the reactive are focused within a beam towards the substrate due to the unbalanced magnetic field, and thus particles reaching the edges of the substrate are coming from the beam at a greater angle.

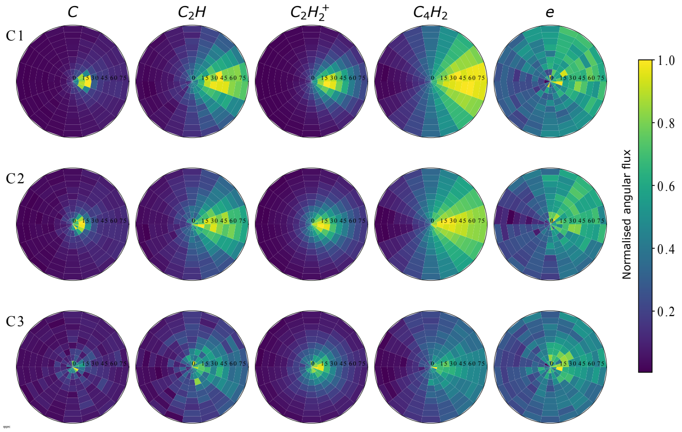

Figure 11 Angular distribution of several species' substrate impinging flux normalized on solid angles (in particles sr^{-1}), onto three zones defined by their distance from the center with A, B, and C corresponding to r$\in$ [0,6], [6,18], [18,30] mm respectively. The fluxes' orientation angle is defined relative to the outward direction (rotational symmetry).

This angle of incidence also depends on the species as can be seen by comparing the angle of sputtered C atoms (around 15°) to the angle of the $C_2H_2^+$ ions (around 30°) onto the outermost zone (the zone "C"). The widest angles have been found for neutral species created within the beam like the C_4H_2 molecule (around 60°), and even between neutral species angular distributions could differ, as one can see by comparing the C_2H and C_4H_2 distributions. The electron angular distribution is also shown on Figure 11, as it demonstrates a particularity of the electron flux in unbalanced magnetrons. One can see on those distributions an asymmetry with more electrons having a positive φ angle. This comes from the fact that electrons rotate around the magnetic field lines which are stronger close to the axis passing by the center of the substrate. The magnetic field is around 0.02 T close to the substrate center and the electron temperature is around 2.4 eV, which means that the Larmor Radius of electrons [1] should be around 7.1 mm, and indeed, the gyration of electron is most visible on zone “B”, so for electrons with a distance from the center between 6 and 18 mm.

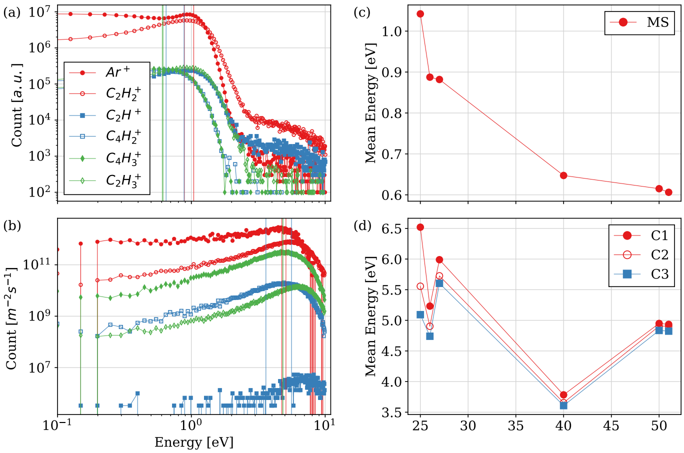

Figure 12 Ion Energy Distribution Function (IEDF) of several species measured by the mass spectrometer (a), and sampled from a simulation (b) with 20% acetylene and 0.8 W and with a substrate placed at 10 cm from the target. Mean energy of those ions from the experiment (c) and from the simulation (d) taken has a weighted average sum of intensities over the energy bins (from 0 to 10 eV by steps of 0.25 eV). The vertical lines on (a) and (b) shows the positions of the average energies.

The angular distribution of impinging species is hard to measure experimentally; however, it is possible with a mass spectrometer to measure ion energy distribution function (IEDF). The mass spectrometer described in section 2.1 was placed to this effect in front of the magnetron at 10 cm distance in a discharge with a current set to 100 mA and 20% C_2H_2 and the MS intensity was sampled in SIMS mode for energy bins of 0.05 eV width from 0.05 to 10 eV, the results for the main ions are shown Figure 12a. A simulation with similar C_2H_2 ratio and distance between substrate and target was run for 120 µs and the energy of ions was sampled onto membranes which positions and sizes correspond to the detector C1, C2, C3 of Figure 11 and of Table 3. The resulting IEDFs from the sampling on the central membrane averaged on time from 10 μs to 120 μs is shown in shown Figure 12b. On Figure 12c and on Figure 12d the mean energy of ions from respectively the experimental and simulation result, calculated as the weighted mean of the intensity count summed over all energy bins. The average energy in the simulations was around 5 eV whereas it was at only around 1 eV in the MS measures. It is not clear what could be the reason of the discrepancy. From the simulation this energy is explained by the fact that the plasma potential in the vicinity of the substrate is around 4-5 eV. As it is well known [1,2] the charged particles in a low pressure plasma discharge gain energy proportional to the plasma potential without losing much energy to collisions when impinging grounded surfaces due to the formation of a sheath. This means that either: (i) the plasma potential in the experiments was actually around 1-2 eV, (ii) the MS was not at ground potential, or (iii) the measured energy suffered other instrumental biases like anode effects [3,4] or the shielding of the MS end-cap potential due to the deposition of a dielectric a-CH film. The third option (iii) is deemed the most probable as this method of IEDF measurement would require more calibrations with a proper hydrocarbon ion source at set energies.

Studying the IEDF with the MS revealed some high energy particles (on the right side of Figure 12a) that could only be explain by either instrumental error or backscattering of ions. Some SRIM calculations gave the probability of 0.0042 for the backscattering of two C^+ ions at 100 eV, which can serve as a general approximation for the backscattering of $C_2H_2^+$ at 200 eV. Given that for the same ion flux the yield of sputtered carbon is around 0.14, the resulting flux of high energy C_2H_2 coming from backscattering should be around two orders of magnitude smaller than that of the sputtered carbon, to that must be added the probability of the backscattered ions to be ionised on their way to the substrate, resulting in at least 3 orders of magnitude below the maximum $C_2H_2^+$ count. This is approximatively what is observed but the difference in sensibility is still quite high between 10^7 count s^{-1} and 10^4 count s^{-1}. Additionaly, Ar^+ did not produce any backscattered ions in the SRIM calculations so its presence in the high energy range even in lower relative quantity, adds to the doubts regarding the fiability of this interpretation.

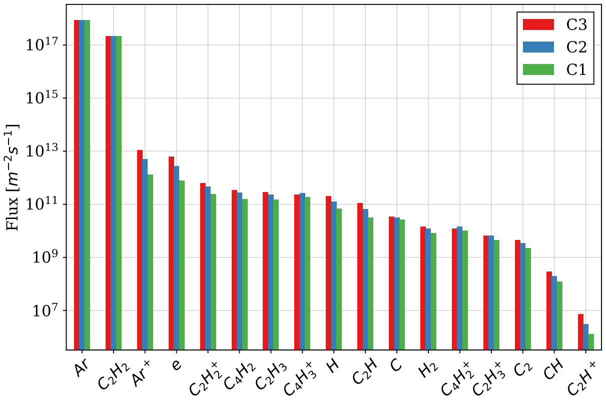

Figure 13 Fluxes of all species through the three membranes C1, C2 and C3 in a simulation with 20% C_2H_2 and 0.8 W after 600µs of simulation.

Finally, the composition of the flux on the three membranes defined higher is shown in Figure 13, as it could be useful for as a reference for film growth simulation. It is interesting to note that as discussed earlier the $C_4H_3^+$ and $C_4H_2^+$ ions had their highest fluxes on the C2 membrane and not the C3 as all other species. This is due to the fact that they are produced on collisions between the background C_2H_2 and the $C_2H_2^+$ ions coming in a focused beam. Hence, the longer the path of the $C_2H_2^+$ ions the more $C_4H_3^+$ and $C_4H_2^+$ are produced, which explains the previous observation on the quantity of those heavier ions away from the substrate center.

References:

[1] A. Fridman, Plasma Chemistry, 2008. https://doi.org/10.1017/CBO9780511546075.

[2] A. Von Keudell, C. Hopf, T. Schwarz-Selinger, M.C.M. Van De Sanden, R.J. Severens, A.M. Gielen, R.A. Langley, J. Bohdansky, W. Eckstein, K. Bera, B. Farouk, P. Vitello, M. Meier, W. Jacob, G. Federici, C.H. Skinner, J.N. Brooks, Surface processes during thin-film growth, Plasma Sources Sci. Technol. 9 (2000) 455–467. https://doi.org/10.1088/0963-0252/9/4/302.

[3] A. Belkind, F. Jansen, Anode effects in magnetron sputtering, Surf. Coatings Technol. 99 (1998) 52–59. https://doi.org/10.1016/S0257-8972(97)00409-X.

[4] T. Melzig, M. Siemers, A. Pflug, R. Rank, 3D PIC-MC simulation of anode effects in dual magnetron discharges, Surf. Coatings Technol. 241 (2014) 30–32. https://doi.org/10.1016/j.surfcoat.2013.10.024.

Appendix B: Extrapolation of the DB coverage

The dangling bonds (DB) availability evolves slowly during simulations due to the unavoidable mismatch between the timescale of PIC-MC plasma simulations (few µs) and the timescale of film deposition (few ms). In order, to predict the correct radical absorption at equilibrium it was necessary to extrapolate the mean DB surface density (or a-C coverage). Seven simulations were run with various acetylene ratio and discharge power starting from 0% a-C coverage (no DB) and seven other simulations with similar parameters but starting from 35% a-C coverage. All simulation started from 0% a-C coverage had a linearly increasing mean a-C coverage, and all simulations starting from 35% had a linearly decreasing mean coverage as can be seen in Figure 6a. From fits of those data points, we obtained the equilibrium coverage and the equilibrium time according to:

$$Cov_{eq} = a_0 \times t_{eq} + b_0 = a_{35} \times t_{eq} + b_{35}, \qquad (B.1)$$

$$t_{eq} = \frac{b_{35} - b_0}{a_0 - a_{35}} \qquad (B.2)$$

With a_0, b_0 the fit coefficient of the mean a-C coverage from simulation starting at 0% and a_1, b_1 for the ones starting at 35%. Then we fitted the evolution of the adsorption of C_4H_2 and C_2H_3 which are the two radicals whose adsorption depends the most on the availability of DBs as can be seen in Figure 6b and in Table 2. The adsorption of those two species at equilibrium, and the adsorption multiplication coefficient is then given by:

$$Corr_{C_4H_2} = \frac{Adso_{C_4H_2}(t_{eq})}{Adso_{C_4H_2}(t_f)}, \qquad (B.3)$$

$$Adso_{C_4H_2}(t) = A \times t + B \qquad (B.4)$$

With t the time, A and B the adsorption fit coefficients, $Adso_{C_xH_y}$ the adsorption of species C_xH_y and $Corr_{C_xH_y}$ the multiplication coefficient of species C_xH_y. A summary of the radical contribution calculation is shown in Table 4, with each column corresponding to 2 simulations (from 0% and from 35%). The important error of these coefficients is balanced by the relatively small importance of C_2H_3 and C_4H_2 adsorption to the total deposition. The biggest source of error remains the standard deviation of the deposition rates (error bars in Figure 7).

Table 4 Summary of the radical contribution calculations.

Power [W] Ratio	0.60 20%	0.70 20%	0.80 20%	0.80 15%	0.80 10%	0.80 4%	0.90 20%
Equilibrium time [ms]	11.27	9.39	7.51	8.76	13.18	23.84	6.63
Error [ms]	2.30	2.47	9.96	8.80	2.39	5.82	9.92
Equilibrium coverage [%]	0.07	0.06	0.06	0.06	0.10	0.18	0.05
C_2H_3 coefficient	1162.58	1457.29	540.15	574.77	168.67	514.37	598.17
C_2H_3 coefficient error	4.88	5.58	5.01	4.79	471.62	135.92	31.25
C_4H_2 coefficient	341.94	314.31	366.61	436.62	224.19	264.50	445.85
C_4H_2 coefficient error	6.27	7.27	6.93	5.88	90.30	75.85	69.56
Error due to radical correction [nm.min^{-1}]	0.002	0.006	0.005	0.003	0.016	0.003	0.074
Standard deviation of the deposition rate [nm.min^{-1}]	0.054	0.064	0.066	0.061	0.032	0.018	0.084
Deposition rate without radical correction [nm.min^{-1}]	0.2451	0.26	0.329	0.273	0.195	0.087	0.377
Deposition rate with radical correction [nm.min^{-1}]	0.2838	0.3295	0.397	0.328	0.213	0.096	0.486

5.1 Complements

5.1.1 QCM Measurements

In order to get a better understanding of the deposition process the deposition rate was measured at different positions, acetylene ratios, and powers and compared with simulations' predicted deposition rate for the same locations and conditions. Firstly, the deposition rate was sampled at different position in the chamber (parallel to the target at 80 mm distance and with varying distance from the x-axis) with a quartz crystal microbalance (QCM) in a discharge with 20% acetylene and a current set to 20 mA (Figure 5.1a), and also at different currents for a fixed central position (Figure 5.1b).

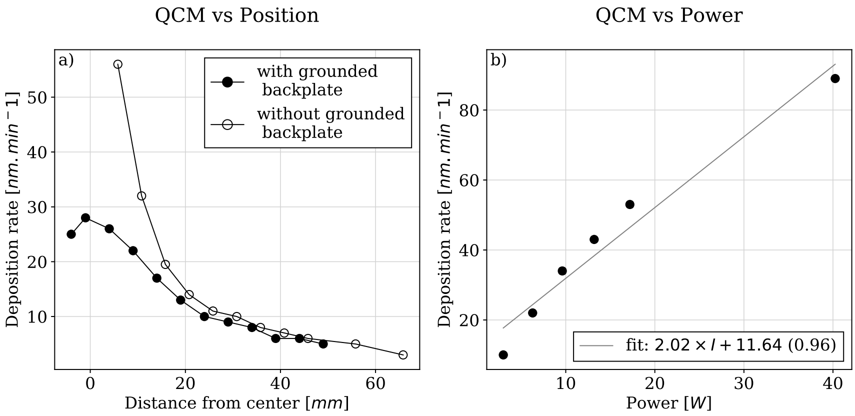

Figure 5.1. Quartz crystal microbalance measurements of the deposition rate vs the sideway distance from the centre of the chamber (a) and vs the power with a linear fit (b). The measurements of the deposition rate with position was affected by the presence or absence of a grounded backing plate behind the detector (full/empty markers).

The measured deposition rate was in the range of several tenth nm min^{-1} which is coherent for this particular deposition process. The principal observations are that the deposition rate decreased with the distance from the centre of the chamber with a gaussian profile, and that there is a linear relationship between the discharge power and the deposition rate. It was found that the presence or absence of a metallic grounded plate behind the quartz had a great influence on the measured deposition rate. Since the quartz mount was itself grounded one possible explanation is that in the case where the quartz is alone in the chamber it acts as an anode for the magnetron which collects electrons from a wide area and possibly creates secondary ionised particles in the vicinity of the QCM or at least augments the number of charged particles impinging the quartz. This anode effect is well described in Belkind et al. [132] and was demonstrated with PIC-MC simulations in magnetron [133]. QCM are very sensitive to temperature and a flux of charged particles can raise their temperature which would results in erroneously high deposition rate measurement. A similar effect could have impacted the measures even for the case where a grounded plate was added, however both set of measures tends to agree for measures far from the centre where the charged particle bombardment was probably lower. The linear fit of the deposition rate in respect to the discharge current is made less accurate with the point at 100 mA which is lower than expected if extrapolating from low-current points. However, it is hard to say if this observation means that the deposition rate dependency with power is more complex or if this is due to the quartz sensitivity to charged particle flux or other biases.

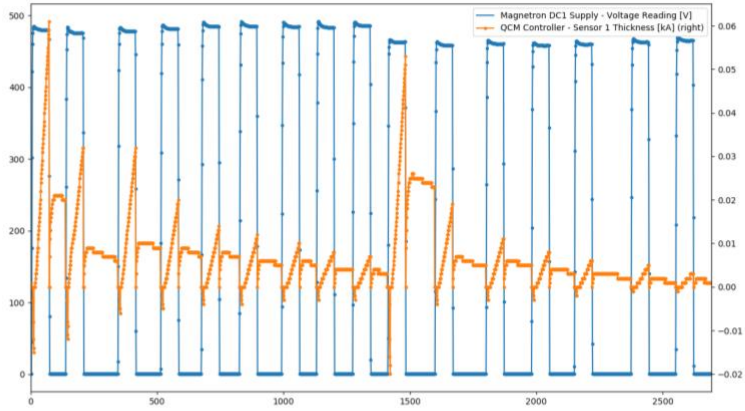

Figure 5.2 Deposition rate at various position of the quartz moved in a plan parallel to the substrate (orange), and voltage (blue). The distances from the middle are respectively (in cm): [0, -1, -2, -3, -4, -5, 0, -0.5, -1, -1.5, -2, -2.5, -3, -3.5]. The absolute thickness measurement on the QCM was reset to 0 at every magnetron ignition and shutdown.

Another interesting observation, is that deposition occurred even after the magnetron was shut down. As can be seen in Figure 5.2, when the magnetron is powered, the film thickness increased linearly; but, it also kept increasing for up to 10 s after the magnetron power supply was cut off. Based on PIC-MC simulations we know that the equilibrium for charged species is quite fast to obtain (in the order of 5-10 µs), so this deposition is probably due to reactive neutral species thermally diffusing and condensing onto the substrate. It seems in Figure 5.2 that the deposition rate before the shutdown decreased with the distance from the centre (as is also shown in Figure 5.1), and that the deposition rate after the shutdown also decreased with distance but with less variation. This observation, if confirmed with a more rigorous protocol[27] would validate the absorption profile given by our simulations since we showed in Figure 8 of the article presented in Chapter 5 that the profile of radicals is flatter than the one of ions.

5.1.2 Cathode pollution

One common issue with DC reactive magnetron deposition of a non-conductive films like a-CH is that if the deposition rate is higher than the target sputtering rate, an insulating film can form on the target. This affects the voltage and creates instabilities like arcs, and it would eventually result in the discharge shutting down after a thick enough film is formed. To start the discharge in similar conditions between each measurement it is necessary to perform etching of the target in pure noble gas atmosphere prior to any introduction of a reactive gas in order to clean the target's surface. However, other phenomenon might affect the electrical conductivity of the target like a change in structure due to the ion bombardment, a change of target's thickness, a change in the shape of the racetrack[13], and various thermal effects. This all makes the target's voltage evolve in sometimes unpredictable ways.

Since the current was fixed during film deposition, and since the voltage evolved due to the aforementioned target pollution, the discharge input power was not fixed. This is an issue, especially since we tried to compare discharges with different powers to get an idea of

---

[27] *As explained earlier, the QCM measurements suffered from a possible bias due to not being thermally stabilised.*

the power scaling of various plasma parameters. Figure 5.3 shows the magnetron DC voltage measured during deposition of several a-CH film with various C_2H_2 ratios. We can see on this figure that the voltage dropped significantly during the first minute of the discharges then raised gradually in most experiments; apart from the one with the lowest C_2H_2 concentration were the voltage slowly decreased. This increase seems to be more pronounced for discharges with higher C_2H_2 concentrations. Several peaks coming from arcing are also visible.

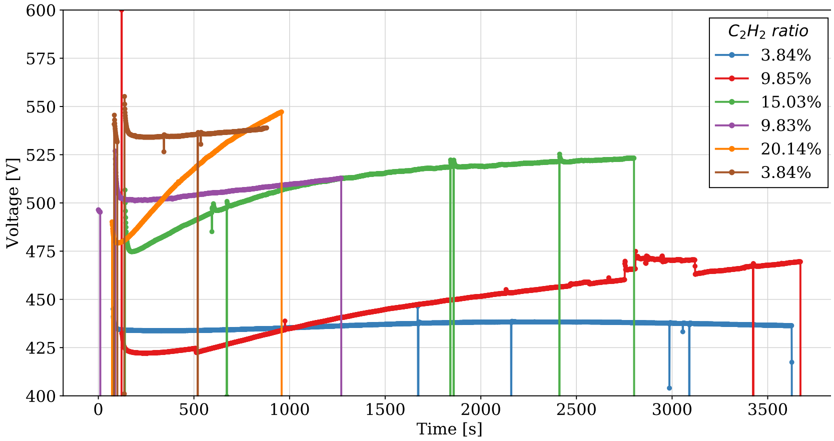

Figure 5.3 Evolution of the voltage during a-CH deposition in the Mantis reactor with various ratios of C2H2

In the experiment with 9.85% of C_2H_2 the magnetron voltage increased by approximatively 25 V in 1000 s. If we assume a resistivity of a-CH of 1e7 $\Omega\ cm^{-1}$ as in [21], then:

$$\Delta \mathrm{D} = \frac{\Delta \mathrm{U}}{\rho \mathrm{I}} \qquad \text{(Eq. 5.1)}$$

With ΔU the voltage increase, I the current, ρ the linear resistivity, and ΔD the target pollution thickness increase. We found that the film should have increased by 250 nm in 1000 s, which gives a deposition rate of 15 nm min^{-1}, which is very close to the deposition rate of a-CH in DC magnetron with 10% C_2H_2 on the substrate side (see Figure 7 of article 2).

Of course, the deposition rate onto the substrate might be different than the one on the target, since the species flux are different. The ions bombardment is much more energetic (around 200 eV) so the sputtering is much higher, but also the deposition of $C_2H_2^+$. Moreover, the radical concentration is much higher close to the magnetron as seen in Chapter 4. Since both differences (more deposition and more sputtering) compete against each other, and since the voltage evolution is in good correspondence with the deposition rate of a-CH on the substrate; the slow voltage evolution is indeed a direct consequence of cathode pollution alone.

This means that even if the voltage of the DC generator increased throughout experiments this had probably a minor effect on the plasma discharge itself. Indeed, since the pollution acted as a resistance the potential “seen” by the plasma is not the one delivered by the generator but the one on the target’s surface. Furthermore the voltage of a magnetron discharge is in direct correlation with the electronic density which depends mainly on the SEEY [134], which is probably quite similar between a-CH and graphite and certainly similar for a-CH films of various thickness.

In conclusion, the discharges were probably effectively at fixed powers but the generator had to increase voltage to maintain a constant current and a constant voltage on the target's surface, despite the deposition of a dielectric a-CH film.

5.1.3 The substrate bias

In most state-of-the-art DLC deposition processes a substrate bias is used with the ideas that the bias will accelerate the ions and will raise the density, raise the amount of sp^3 bonds, and diminish the amount of hydrogen in the films. Another benefit of using biases is to have more homogeneous films on wider or more complex substrates. In this study bias was never applied experimentally because the inhomogeneity of the films was useful to better constraint the simulation correctness. However, to verify that this model could be applicable to cases with a substrate bias, several simulations were run with various biases. Figure 5.4 shows that the substrate bias had an effect in the simulations on the voltage of the magnetron[28]. Indeed, the voltage increased in simulations from 250 V to 450 V with biases from 0 to 200 V. Two simulations

---

[28] *The discharge power was fixed in the simulations via a feedback loop controlling the magnetron voltage and letting the current freely evolve.*

were run with a 300 V bias and both reached an instability around 18 μs.

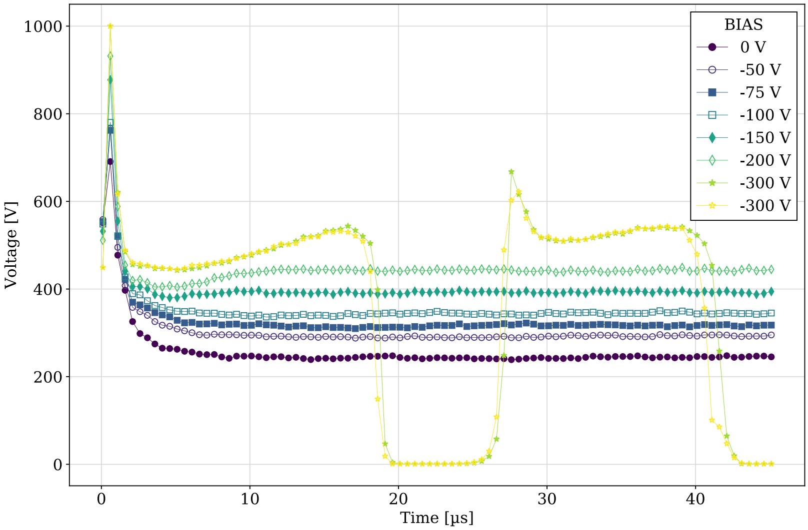

Figure 5.4 Variation with time of the DC voltage of the magnetron, in several simulations with various substrate biases.

We can see in Figure 5.5 that the evolution of the discharge voltage was in fact linearly evolving with the substrate bias. The fact that the substrate potential has any effects on the discharge is surprising at first. However, to understand this result we must note that the grounded substrate plays in our set-up the role of the anode since it is facing the magnetrons surface only 10cm away from it. Moreover, due to the unbalanced magnetic field, the electrons are spiralling around magnetic lines and directed in a beam towards the substrate. DC magnetron sputtering is similar to the classical Townsend discharge (see 1.1), and near the target a positive sheath is created which accelerate electrons outward and repeals the slow ions. In a similar manner a sheath is created near every surface embedded in the plasma due to the higher mobility of electrons. However, when a bias is applied to the substrate it repeals more strongly the electrons which then require a higher kinetic energy or a higher density to maintain a constant current.

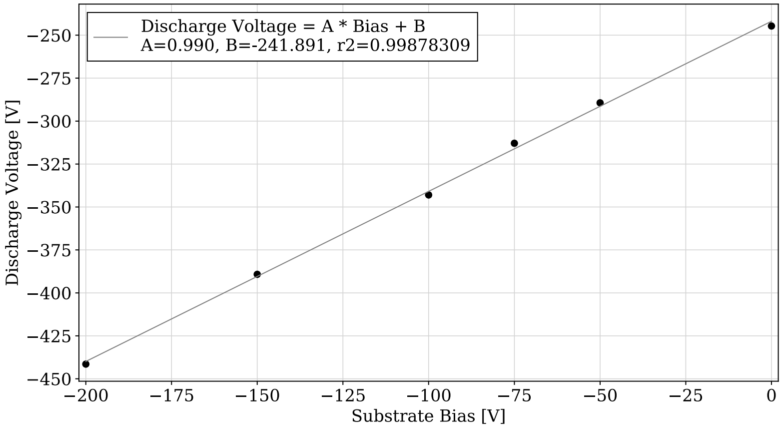

Figure 5.5 Discharge voltage of the magnetron in simulations with different substrate bias, fitted with a line which parameters and coefficient of determination are given in the legend.

Since in our simulations the voltage was controlled to keep the discharge power constant[28 above], the most probable explanation of this observation is that the voltage had to become more negative in order to accelerate electrons faster and create more ions and secondary electrons, and thus keep the current from diminishing. This also explains why reaching a substrate bias voltage of -300 V destabilised the discharge: the electron density raised too much in those simulation and reach the numerical limit (around 1× 10^{15} m^{-3}) around were electrons are skipping cells and not properly confined. This effect of the substrate bias on the electronic density is shown in Figure 5.6.

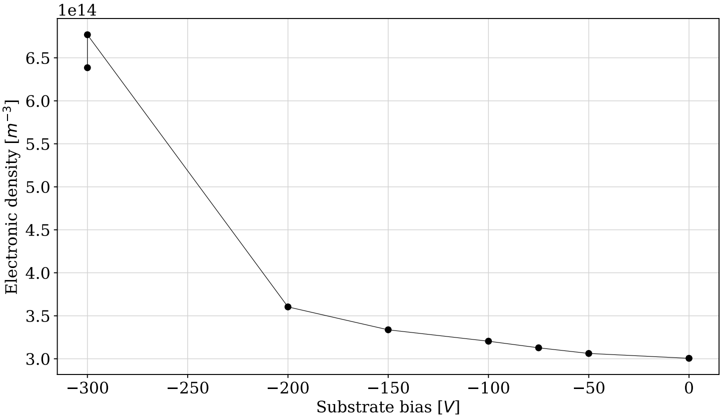

Figure 5.6 Influence of the substrate bias on the maximum electronic density in the chamber.

Those simulations that included bias also increased ion bombardment and ion energy; however, the effect of ion energy on the surface reaction should have been included in order to be able to understand the effect of the bias on the film structure. Nevertheless, the results would most probably show, as in [24], a decrease in H%, and an increase in sp^3/sp^2 ratio and hardness, as more energetic ions are likely to increase the hydrogen etching and the film density, which are parameters linked to the sp^3/sp^2 ratio and hardness by [20,106].

5.1.4 The Hydrogen discrepancy

The main discrepancy observed between the simulations and experiments was that of the hydrogen concentration predicted from the adsorption and desorption profiles of the simulation, and the measured hydrogen content of films obtain with ERDA measurements illustrated by the Figure 9b of the second article. From the measurements we showed that there was around 35% of hydrogen in the samples with a clear decrease (from 35% to 30% with 1% of error) of the H concentration near the centre of the substrate. Whereas from the simulation the H concentration was around 43% and with a different profile. The main argument advanced in the article's discussion was that the probability of H desorption from chemical sputtering was calculated from an extrapolation of an empirical law in Hopf et al. [15], and that by adjusting this value *a posteriori* it was possible to obtain an average H concentration around 35%. However, the shape of the H profile was still unreconcilable with less hydrogen in the centre of the sample in the simulation.

This means that some physical effects must have been neglected in our current surface deposition model. The first two issues of the model to investigate would be: (i) only the surface state of the growing film is considered, but in reality, lot of reactions (ion subplantation, chemical sputtering, H-diffusion) happen below the surface, (ii) the impact of ions kinetic and internal energy, as well as the angular distribution of the precursor flu are not considered. One way to study those two effects would be to use the calculated fluxes obtained here from PIC-MC simulations as inputs for dedicated film growth simulation using for example kinetic Monte-Carlo (kMC) of Molecular Dynamics (MD) methods. Initial test performed by colleagues at the LARN with kMC simulations based on the same surface reaction probability showed that without changing the probability of chemical sputtering but only thanks to the more detailed incorporation of energy and angles and of the whole thickness of the growing film the H concentration tended to be closer to the experimental one. However, those results are really preliminary and this kMC software that includes amorphous films and chemical reactions needs more tests prior to this one to be validated. Nonetheless, those results are encouraging and if confirmed will be the object of a separate publication.

Another possible explanation of this discrepancy could come from the neglected thermal effects [139–141]. Indeed, we know that a substrate can be heated by ion bombardment, especially with unbalanced magnetrons; hence in our case, especially at the centre of the sample. In fact, the QCM measurements (see section 5.1.1), showed that the flux of charged particles in the centre of the chamber could have an impact on QCM measures via heating of the quartz. It is also known that when heating DLC after deposition for annealing, hydrogen is being desorbed above 390 °C and only sp^2 bonded carbon is observed after annealing at 590 °C [141]. It is then possible that during the film deposition the higher heat in the centre of the sample caused more hydrogen desorption which would reconciliate the hydrogen concentration profile with modification of the chemical sputtering (green diamonds) and the ERDA measures (red dots) of Figure 9b of article 2.

Chapter 6 *Conclusions*

After laying down the theoretical background, we reviewed the literature related to the PCR of acetylene and the plasma simulation methods, focusing on finding the reactions and methods that are relevant in our case. We then constructed and optimised a numerical model in order to perform fast simulations and explore the parameter space. The two main parameters which effects were analysed, were the discharge power and the acetylene/argons ratio. Injecting more of a molecular gas like acetylene inside a plasma reactor affects not only the amount of reactive that will be produced from dissociating the acetylene molecule but it also affects the plasma in several ways. We showed in a first publication (Chapter 4) that injecting acetylene even in very small quantity had an important effect on e.g. the electronic density, the shape of the plasma bulk, or the flux of sputtered particles and ions. Due to the high computational cost of PIC-MC simulations, it is rare to see in the literature simulations that include more species than just the background gases and the main ionic species, and it is even less frequent to include some radical species. However, in our case the addition of more species was required since we showed in section 3.2.1 that radicals must be created in high quantities and that they would most probably undergo at least one reaction with acetylene on their way to the substrate, creating new species with higher carbon content (e.g. C_4H_2) thus participating in the deposition. It was interesting to show the linear increase of first order species produced via the dissociation of acetylene from collisions with electron with power, and with acetylene ratio, and we also demonstrated the presence in relatively important quantities of second order species like e.g. $C_4H_3^+$, C_4H_2, or C_2H_3 via the simulations and via mass spectrometric measurements.

One of the main results of Chapter 4 is the match between the experimental and simulated $C_2H_2^+$, C_4H_3+, $C_4H_2^+$, $C_2H_3^+$ and Ar^+ flux at the location of the substrate with a linear fit that goes from the low powers of the simulations around 0.5-1 W to the lowest experimentally attainable powers around 2 W and up to 22 W. We understood from the simulation that the effect of increasing the discharge power was mainly to increase the electronic density (and not the electronic temperature which remained fairly constant in the studied range), and with it the densities of all first order species. This led us to think that the power-scaling of simulations' results is possible as long as the density of reactive species remained small compared to the background acetylene.

The densities of the second order species was interestingly quadratic in respect to the acetylene ratio since the reaction rates depended of both the acetylene and the first order species concentration. This means that a small variation of the acetylene influx could potentially have a big impact on the produced films. The agreement with experiment was only qualitative for the neutral species' densities since the simulation could not be run long enough for the radical to reach equilibrium, and since the spectrometer gave results that are hard to interpret in RGA (neutral) mode due to the dissociation of molecules in the MS ionizer. However, in the second article simulations were further optimized and run for longer (up to 1.2 ms) and an equilibrium was obtained for all densities. They confirmed what was expected from the discussions around the Figure 3 of the first article: that the concentration of C_2H and H will be lower but the concentrations of C_4H_2 and H_2 higher at equilibrium.

Another interesting observation done in Chapter 4 was the fact that the concentrations varied throughout the chamber in such a way that the film deposition on the substrate must have been different at different locations. Indeed, we identified several groups of species with different behaviours: (i) the ions where focused in a beam towards the substrate due to the unbalanced magnetic field and ambipolar diffusion, (ii) the radicals created within the plasma bulk expanded in a wide cone since they were thermally diffusing, (iii) the sputtered carbon was going in an even wider cone of diffusion with rapidly dropping concentration and high kinetic energy, (iv) the ions and radicals created outside of the plasma bulk from collisions of ions with acetylene where mostly concentrated within a ring around the centre probably because the first order species with higher concentrations in the centre have more time and thus higher probability to collide with the background acetylene on oblique trajectories.

Based on this observation, new simulations with an improved deposition model were performed with the idea of comparing simulated films to experimentally deposited ones, characterised using NISM (Namur Institute of Structured Matter) advanced film characterisation techniques and knowledge. We deposited several films on silicon strips and on vitreous carbon samples and performed several analyses e.g. ERDA, profilometry, XPS, RAMAN. Those experimental results were compared to new longer and improved simulations and this new study was published in a second article presented in Chapter 5. We identified three main contribution to film deposition which were in order of importance: (i) the ions, (ii) the radicals, (iii) the sputtered carbon. The fact that the ion contribution was more important than the radical ones is surprising as most studies of the PECVD of acetylene focuses on the radical contribution. However, this result does not contradict those studies since we used an unbalanced magnetic field and since the type of discharge studied here have a lower working pressure than most.

We were able to reproduce results from previous experimental studies from a similar mixed PVD/PECVD magnetron discharge: the increase in deposition rate and H concentration in the films with C_2H_2 ratio [36,142], and the decrease in hardness and sp^3 bonds could be explained from our results as a passage from a ion dominated deposition to a radical dominated one. We obtained a good quantitative agreement for the evolution of the deposition rate with C_2H_2 ratio between experiment and simulation. To compare the results for the deposition rates, it was necessary to extrapolate results by fitting their power dependency. Additionally, the radical contribution was still evolving due to the slow rate of evolution of the dangling bond coverage, and it was necessary to extrapolate the contribution to deposition of the radicals which depend the most on the coverage (the C_4H_2 and C_2H_3 radicals). Despite these two extrapolations and the uncertainty they introduced, the fact that we were able to obtain quantitative predictions with PIC-MC simulations of a PECVD discharge is notable.

Another good indication of the validity of the simulations was obtained by comparing the deposition profiles of films on wide silicon substrates. The triangular shapes of the film thickness profile were shown to be characteristic of the contribution of the ions to deposition and the relative shape of those profiles matched quite well between the experiments and simulations. This is not only a sign that the simulations presented here are giving realistic results, but also a sign of the relevance of the method of comparing purposely very inhomogeneous films deposited on wide strips to PIC-MC simulations with a deposition model. However, the deposition model developed and presented here, showed some limitations. In particular, there is high uncertainty on most surface reactions and the predictions regarding the hydrogen stoichiometry were unreconcilable with experiments in the centre of the substrate. This is probably an indication that there is room for improvements, in particular we suspect that the kinetic and internal energy of the ions should be considered, and the dangling bond coverage evolution should be optimised more.

This work certainly brought a clearer view of the acetylene low-pressure magnetron discharges, and proved that PIC-MC simulations of a PECVD discharge at very low-pressure could be made in a self-consistent manner with predictions than can be extrapolated to experimental conditions. Now that a first model of the complete discharge from the gas injection to the film deposition was developed several perspectives for continuations of this work are opening.

Firstly, it would be interesting to restrain the number of species even more by for example combining groups of species together and combining the cross sections of reactions leading to their creation. This would reduce the computational cost and allow simulating bigger chambers with one or more magnetrons in diverse magnetic configurations, or more diverse power generation settings (e.g. higher powers, pulsed discharges, variable substrate bias) which is interesting for developing state-of-the-art films.

Secondly, the surface model presented here could be developed further by considering additional effects (e.g. kinetic and internal energy of the ions, evolving structure of the film at deeper depth) and refining the surface reaction probability via for example novel dedicated experiments or film growth simulations. In fact, first kMC simulations were performed based on the output of the currently presented simulations and they showed promising results.

References

[1] G.J.M. Hagelaar, L.C. Pitchford, Solving the Boltzmann equation to obtain electron transport coefficients and rate coefficients for fluid models, Plasma Sources Sci. Technol. 14 (2005) 722–733. https://doi.org/10.1088/0963-0252/14/4/011.

[2] A. Bogaerts, E. Bultinck, M. Eckert, V. Georgieva, M. Mao, E. Neyts, L. Schwaederlé, Computer modeling of plasmas and plasma-surface interactions, Plasma Process. Polym. 6 (2009) 295–307. https://doi.org/10.1002/ppap.200800207.

[3] J. Vetter, 60 years of DLC coatings: Historical highlights and technical review of cathodic arc processes to synthesize various DLC types, and their evolution for industrial applications, Surf. Coatings Technol. 257 (2014) 213–240. https://doi.org/10.1016/j.surfcoat.2014.08.017.

[4] A. Michelmore, J.D. Whittle, J.W. Bradley, R.D. Short, Where physics meets chemistry: Thin film deposition from reactive plasmas, Front. Chem. Sci. Eng. 10 (2016) 441–458. https://doi.org/10.1007/s11705-016-1598-7.

[5] R. Mohan, A. Bogaerts, E. Neyts, M. Mao, M. Eckert, A. Bogaerts, M. Mao, M. Eckert, R. Mohan, A. Bogaerts, E. Neyts, M. Mao, M. Eckert, A. Bogaerts, M. Mao, M. Eckert, Plasma Processing of Nanomaterials, 2011. https://doi.org/10.1201/b11473.

[6] A. Fridman, Plasma Chemistry, 2008. https://doi.org/10.1017/CBO9780511546075.

[7] A. Hurlbatt, A.R. Gibson, S. Schröter, J. Bredin, A.P.S. Foote, P. Grondein, D. O’Connell, T. Gans, Concepts, Capabilities, and Limitations of Global Models: A Review, Plasma Process. Polym. 14 (2016) 1–21. https://doi.org/10.1002/ppap.201600138.

[8] Y. Lifshitz, S.R. Kasi, J.W. Rabalais, W. Eckstein, Subplantation model for film growth from hyperthermal species, Phys. Rev. B. 41 (1990) 10468–10480. https://doi.org/10.1103/physrevb.41.10468.

[9] E.A. Bogdanov, A.S. Chirtsov, A.A. Kudryavtsev, Fundamental nonambipolarity of electron fluxes in 2D plasmas,

Phys. Rev. Lett. 106 (2011) 195001. https://doi.org/10.1103/PhysRevLett.106.195001.

[10] J.T. Gudmundsson, D. Lundin, Introduction to magnetron sputtering, 2019. https://doi.org/10.1016/B978-0-12-812454-3.00006-1.

[11] R. Mc Cray, Hot astrophysical plasmas, Phys. Scr. 1984 (1984) 235–236. https://doi.org/10.1088/0031-8949/1984/T7/055.

[12] J.A. Eilek, Plasma physics in clusters of galaxies, Phys. Plasmas. 10 (2003) 1539–1548. https://doi.org/10.1063/1.1558991.

[13] J.F. Ziegler, M.D. Ziegler, J.P. Biersack, SRIM – The stopping and range of ions in matter (2010), Nucl. Instruments Methods Phys. Res. Sect. B Beam Interact. with Mater. Atoms. 268 (2010) 1818–1823. https://doi.org/10.1016/j.nimb.2010.02.091.

[14] K. Van Aeken, S. Mahieu, D. Depla, The metal flux from a rotating cylindrical magnetron: A Monte Carlo simulation, J. Phys. D. Appl. Phys. 41 (2008). https://doi.org/10.1088/0022-3727/41/20/205307.

[15] C. Hopf, A. von Keudell, W. Jacob, A. Von Keudell, W. Jacob, A. von Keudell, W. Jacob, Chemical sputtering of hydrocarbon films by low-energy Ar ion and H atom impact, IOP Publishing, 2002. https://doi.org/10.1088/0029-5515/42/12/101.

[16] V. Sushkov, A.-P. Herrendorf, R. Hippler, Metastable argon atom density in complex argon/acetylene plasmas determined by means of optical absorption and emission spectroscopy, J. Phys. D. Appl. Phys. 49 (2016) 425201. https://doi.org/10.1088/0022-3727/49/42/425201.

[17] D.D.L. Chung, Review: Graphite, J. Mater. Sci. 37 (2002) 1475–1489. https://doi.org/10.1023/A:1014915307738.

[18] S.S. Shams, R. Zhang, J. Zhu, Graphene synthesis: A Review, Mater. Sci. Pol. 33 (2015) 566–578. https://doi.org/10.1515/msp-2015-0079.

[19] J. Robertson, Diamond-like amorphous carbon, Mater. Sci. Eng. R Reports. 37 (2002) 129–281. https://doi.org/10.1016/S0927-796X(02)00005-0.

[20] J. Robertson, Diamond-Like Carbon Films, Properties and

Applications, Compr. Hard Mater. 3 (2014) 101–139. https://doi.org/10.1016/B978-0-08-096527-7.00043-X.
[21] K. Bewilogua, D. Hofmann, History of diamond-like carbon films - From first experiments to worldwide applications, Surf. Coatings Technol. 242 (2014) 214–225. https://doi.org/10.1016/j.surfcoat.2014.01.031.
[22] D. Sheeja, B.K. Tay, K.W. Leong, C.H. Lee, Effect of film thickness on the stress and adhesion of diamond-like carbon coatings, Diam. Relat. Mater. 11 (2002) 1643–1647. https://doi.org/10.1016/s0925-9635(02)00109-7.
[23] P. Patsalas, S. Logothetidis, P.C. Kelires, Surface and interface morphology and structure of amorphous carbon thin and multilayer films, Diam. Relat. Mater. 14 (2005) 1241–1254. https://doi.org/10.1016/J.DIAMOND.2004.12.039.
[24] D. Thiry, A. De Vreese, F. Renaux, J.L. Colaux, S. Lucas, Y. Guinet, L. Paccou, E. Bousser, R. Snyders, Toward a Better Understanding of the Influence of the Hydrocarbon Precursor on the Mechanical Properties of a-C:H Coatings Synthesized by a Hybrid PECVD/PVD Method, Plasma Process. Polym. 13 (2016) 316–323. https://doi.org/10.1002/ppap.201500050.
[25] A. Grill, B. Meyerson, V. Patel, Interface modifications for improving the adhesion of a-C:H films to metals, J. Mater. Res. 3 (1988) 214–217. https://doi.org/10.1557/JMR.1988.0214.
[26] A. Grill, B.S. Meyerson, V. Patel, Bonding, Interfacial Effects And Adhesion In DLC., Diam. Opt. 0969 (1989) 52. https://doi.org/10.1117/12.948140.
[27] A. Grill, B.S. Meyerson, V. Patel, Invited Paper Bonding, interfacial effects and adhesion in DLC, n.d. http://proceedings.spiedigitallibrary.org/ (accessed March 13, 2019).
[28] W. Mingge, L. Congda, T. Dapeng, H. Tao, C. Guohai, W. Donghui, Effects of metal buffer layer for amorphous carbon film of 304 stainless steel bipolar plate, Thin Solid Films. 616 (2016) 507–514. https://doi.org/10.1016/J.TSF.2016.07.043.
[29] X. Li, P. Ke, H. Zheng, A. Wang, Structural properties and growth evolution of diamond-like carbon films with different incident energies: A molecular dynamics study, Appl. Surf. Sci.

273 (2013) 670–675.
https://doi.org/10.1016/j.apsusc.2013.02.108.

[30] D. Zhang, P. Yi, L. Peng, X. Lai, J. Pu, Amorphous carbon films doped with silver and chromium to achieve ultra-low interfacial electrical resistance and long-term durability in the application of proton exchange membrane fuel cells, Carbon N. Y. 145 (2019) 333–344. https://doi.org/10.1016/j.carbon.2019.01.050.

[31] W. Jacob, W. Möller, On the structure of thin hydrocarbon films, Appl. Phys. Lett. (1993). https://doi.org/10.1063/1.110683.

[32] J. Benedikt, Plasma-chemical reactions: low pressure acetylene plasmas, J. Phys. D. Appl. Phys. 43 (2010) 43001. https://doi.org/10.1088/0022-3727/43/4/043001.

[33] R. Tonneau, P. Moskovkin, A. Pflug, S. Lucas, TiOx deposited by magnetron sputtering: A joint modelling and experimental study, J. Phys. D. Appl. Phys. 51 (2018) 195202. https://doi.org/10.1088/1361-6463/aabb72.

[34] M. Mao, J. Benedikt, A. Consoli, A. Bogaerts, New pathways for nanoparticle formation in acetylene dusty plasmas: a modelling investigation and comparison with experiments, J. Phys. D. Appl. Phys. 41 (2008) 225201. https://doi.org/10.1088/0022-3727/41/22/225201.

[35] V.G. Anicich, W.T. Huntress, M.J. Mcewant, CHEMICAL KINETICS Ion-Molecule Reactions of Hydrocarbon Ions in C2H2 and HCN, 1986. https://pubs.acs.org/sharingguidelines (accessed March 13, 2019).

[36] V. De Vriendt, S.M. Miladinovic, J.L. Colaux, F. Maseri, C.L. Wilkins, S. Lucas, Growth mechanisms involved in the synthesis of smooth and microtextured films by acetylene magnetron discharges, Langmuir. 27 (2011) 8913–8922. https://doi.org/10.1021/la2003035.

[37] J. Winter, J. Berndt, S.-H. Hong, E. Kovacevic, I. Stefanović, O. Stepanović, Dust formation in Ar/CH4 and Ar/C2H2 plasmas, Plasma Sources Sci. Technol. 18 (2009) 034010. https://doi.org/10.1088/0963-0252/18/3/034010.

[38] F.M.J.H.J.H. Van De Wetering, R.J.C.C. Brooimans, S.

Nijdam, J. Beckers, G.M.W.W. Kroesen, Fast and interrupted expansion in cyclic void growth in dusty plasma, J. Phys. D. Appl. Phys. 48 (2015) 035204. https://doi.org/10.1088/0022-3727/48/3/035204.

[39] V. De Vriendt, F. Maseri, A. Nonet, S. Lucas, Study of nanoparticles formation in a pulsed magnetron discharge in acetylene, Plasma Process. Polym. 6 (2009) 6–10. https://doi.org/10.1002/ppap.200930105.

[40] K. De Bleecker, A. Bogaerts, W. Goedheer, Detailed modeling of hydrocarbon nanoparticle nucleation in acetylene discharges, Phys. Rev. E - Stat. Nonlinear, Soft Matter Phys. 73 (2006) 1–16. https://doi.org/10.1103/PhysRevE.73.026405.

[41] J. Benedikt, Acetylene Chemistry in Remote Plasmas: Implications for the a-C:H Growth Mechanism, 2004. https://doi.org/10.6100/IR581182.

[42] V. De Vriendt, S.M. Miladinovic, J.L. Colaux, F. Maseri, C.L. Wilkins, S. Lucas, Growth mechanisms involved in the synthesis of smooth and microtextured films by acetylene magnetron discharges, Langmuir. 27 (2011) 8913–8922. https://doi.org/10.1021/la2003035.

[43] E. Neyts, A. Bogaerts, R. Gijbels, J. Benedikt, M.C.M.C.M. Van De Sanden, Molecular dynamics simulations for the growth of diamond-like carbon films from low kinetic energy species, Diam. Relat. Mater. 13 (2004) 1873–1881. https://doi.org/10.1016/j.diamond.2004.05.011.

[44] H.C. Thejaswini, S. Peglow, U. Martens, V. Sushkov, R. Hippler, Comparative Plasma Chemical Reaction Studies of CH4/Ar and C2Hm/Ar (m = 2,4,6) Gas Mixtures in a Dielectric Barrier Discharge, Contrib. to Plasma Phys. 54 (2014) 683–696. https://doi.org/10.1002/ctpp.201300035.

[45] M. Frenklach, J. Warnatz, Detailed Modeling of PAH Profiles in a Sooting Low-Pressure Acetylene Flame, Combust. Sci. Technol. 51 (1987) 265–283. https://doi.org/10.1080/00102208708960325.

[46] G. Xavier, Chemistry an physics of plasma polymerization probed by mass spectrometry, 2014.

[47] E. Neyts, A. Bogaerts, M. Mao, M. Eckert, Plasma Processing

of Nanomaterials, 2011. https://books.google.com/books?id=29ijh1iCxI4C&pgis=1.

[48] U. Khalilov, A. Bogaerts, S. Hussain, E. Kovacevic, P. Brault, C. Boulmer-Leborgne, E. Neyts, Nanoscale mechanisms of CNT growth and etching in plasma environment, J. Phys. D. Appl. Phys. 50 (2017). https://doi.org/10.1088/1361-6463/aa6733.

[49] M.-Y. Song, J.-S. Yoon, H. Cho, G.P. Karwasz, V. Kokoouline, Y. Nakamura, J. Tennyson, Cross Sections for Electron Collisions with Acetylene Molecules, J. Phys. Chem. Ref. Data. 37 (2017) 913–931. https://doi.org/doi: 10.1063/1.2838023.

[50] D. Reiter, R.K. Janev, Hydrocarbon collision database_Reiter-Kuper-Janev.pdf.pdf.pdf, (n.d.). http://www.hydkin.de/.

[51] T. Shirai, T. Tabata, H. Tawara, Y. Itikawa, Analytic cross sections for electron collisions with hydrocarbons: CH4, C2H6, C2H4, C2H2, C3H8, and C3H6, At. Data Nucl. Data Tables. 80 (2002) 147–153. https://doi.org/10.1006/adnd.2001.0878.

[52] R.K. Janev, D. Reiter, Collision processes of C2,3Hy and C2,3Hy+ hydrocarbons with electrons and protons, Phys. Plasmas. 11 (2004) 780–829. https://doi.org/10.1063/1.1630794.

[53] R.K. Janev, D. Reiter, Collision processes of CHy and CHy+ hydrocarbons with plasma electrons and protons, Phys. Plasmas. 9 (2002) 4071. https://doi.org/10.1063/1.1500735.

[54] M. Vinodkumar, A. Barot, B. Antony, Electron impact total cross section for acetylene over an extensive range of impact energies (1 eV–5000 eV), J. Chem. Phys. 136 (2012) 184308. https://doi.org/10.1063/1.4711922.

[55] J. Franz, F.A. Gianturco, K.L. Baluja, J. Tennyson, R. Carey, R. Montuoro, R.R. Lucchese, T. Stoecklin, P. Nicholas, T.L. Gibson, Correlation–polarization effects in electron/positron scattering from acetylene: A comparison of computational models, Nucl. Instruments Methods Phys. Res. Sect. B Beam Interact. with Mater. Atoms. 266 (2008) 425–434. https://doi.org/10.1016/J.NIMB.2007.12.019.

[56] S.T. Chourou, A.E. Orel, Dissociative electron attachment to acetylene, Phys. Rev. A. 77 (2008) 042709.

https://doi.org/10.1103/PhysRevA.77.042709.

[57] F.A. Gianturco, T. Stoecklin, Electron scattering from acetylene: elastic integral and differential cross sections at low energies, J. Phys. B At. Mol. Opt. Phys. 27 (1994) 5903–5921. https://doi.org/10.1088/0953-4075/27/24/014.

[58] Y. Nakamura, Electron swarm parameters in pure C 2 H 2 and in C 2 H 2 –Ar mixtures and electron collision cross sections for the C 2 H 2 molecule, J. Phys. D. Appl. Phys. 43 (2010) 365201. https://doi.org/10.1088/0022-3727/43/36/365201.

[59] A. Gauf, C. Navarro, G. Balch, L.R. Hargreaves, M.A. Khakoo, C. Winstead, V. McKoy, Low-energy elastic electron scattering by acetylene, Phys. Rev. A. 87 (2013) 012710. https://doi.org/10.1103/PhysRevA.87.012710.

[60] I. Iga, M.-T. Lee, P. Rawat, L.M. Brescansin, L.E. Machado, Elastic and total cross-sections for electron scattering by acetylene in the intermediate energy range, Eur. Phys. J. D. 31 (2004) 45–51. https://doi.org/10.1140/epjd/e2004-00134-y.

[61] A. Jain, Low energy (0.01-20 eV) electron scattering from acetylene, J. Phys. B At. Mol. Opt. Phys. 26 (1993) 4833–4844. https://doi.org/10.1088/0953-4075/26/24/015.

[62] L. Andric, R.I. Hall, Resonance phenomena observed in electron scattering from acetylene, J. Phys. B At. Mol. Opt. Phys. 21 (1988) 355–366. https://doi.org/10.1088/0953-4075/21/2/019.

[63] S.J. King, S.D. Price, Electron ionization of acetylene, J. Chem. Phys. 127 (2007) 174307. https://doi.org/10.1063/1.2777154.

[64] R. Tonneau, A. Pflug, S. Lucas, Magnetron sputtering: determining scaling relations towards real power discharges using 3D Particle-In-Cell Monte Carlo models, Plasma Sources Sci. Technol. (2020). https://doi.org/10.1088/1361-6595/abb3a0.

[65] F.J. Gordillo-Vazquez, J.M. Albella, A quasianalytic kinetic model for nonequilibrium C2H2(1%)/H2/Ar rf plasmas of interest in nanocrystalline diamond growth, Plasma Sources Sci. Technol. 11 (2002) 498–512. https://doi.org/10.1088/0963-0252/11/4/317.

[66] A. Baby, C.M.O. Mahony, P.D. Maguire, Acetylene–argon

plasmas measured at a biased substrate electrode for diamond-like carbon deposition: I. Mass spectrometry, Plasma Sources Sci. Technol. 20 (2011) 015003. https://doi.org/10.1088/0963-0252/20/1/015003.

[67] W. Van Gaens, A. Bogaerts, Kinetic modelling for an atmospheric pressure argon plasma jet in humid air, J. Phys. D Appl. Phys. 46 (2013). http://iopscience.iop.org/article/10.1088/0022-3727/46/27/275201/pdf (accessed April 24, 2018).

[68] B.J.L. Berry, DAVID HARVEY: SOCIAL JUSTICE AND THE CITY, Antipode. 6 (1974) 142–149. https://doi.org/10.1111/j.1467-8330.1974.tb00606.x.

[69] L. Sharma, R. Srivastava, A.D. Stauffer, Excitation of the metastable states of argon, J. Phys. Conf. Ser. 80 (2007). https://doi.org/10.1088/1742-6596/80/1/012019.

[70] I. Stefanović, N. Sadeghi, J. Winter, The influence of C 2 H 2 and dust formation on the time dependence of metastable argon density in pulsed plasmas, J. Phys. D. Appl. Phys. 43 (2010) 152003. https://doi.org/10.1088/0022-3727/43/15/152003.

[71] F.J. Gordillo-Vázquez, J.M. Albella, Distinct nonequilibrium plasma chemistry of C2 affecting the synthesis of nanodiamond thin films from C2H2(1%)/H 2/Ar-rich plasmas, J. Appl. Phys. 94 (2003) 6085–6090. https://doi.org/10.1063/1.1617362.

[72] R. Engeln, K.G.Y. Letourneur, M.G.H. Boogaarts, M.C.M. van de Sanden, D.C. Schram, Detection of CH in an expanding argon/acetylene plasma using cavity ring down absorption spectroscopy, Chem. Phys. Lett. 310 (1999) 405–410. https://doi.org/10.1016/S0009-2614(99)00810-6.

[73] D. Thirumalai, K. Onda, D. Truhlar, Elastic scattering and rotational excitation of a polyatomic molecule by electron impact: Acetylene, J. Chem. Phys. 526 (1981). https://doi.org/10.1063/1.440804.

[74] K. Ostrikov, Reactive plasmas as a versatile nanofabrication tool, Rev. Mod. Phys. (2005). https://doi.org/10.1103/RevModPhys.77.489.

[75] C. Deschenaux, Etude de l'origine et de la croissance de particules submicrometriques dans les plasmas radiofrequence

réatifs, (n.d.).
[76] M. Mao, A. Bogaerts, K. De Bleecker, A. Bogaerts, W. Goedheer, S. Stoykov, C. Eggs, U. Kortshagen, M. Eckert, M. Mao, E. Neyts, Computer modelling of the plasma chemistry and plasma-based growth mechanisms for nanostructured materials, J. Phys. D Appl. Phys. 44 (2011) 174030–16. https://doi.org/10.1088/0022-3727/44/17/174030.
[77] P.M. Mul, J.W. McGowan, Dissociative recombination of C2+, C2H+, C2H2+ and C2H3+, Astrophys. J. 237 (1980) 749. https://doi.org/10.1086/157921.
[78] A.M. Derkatch, L. Vikor, A. Neau, W. Shi, H. Danared, Branching ratios in dissociative recombination of the C 2 H 2 molecular ion, Sci. Technol. 32 (1999) 3391–3398.
[79] A.A. Viggiano, A. Ehlerding, S.T. Arnold, M. Larsson, Dissociative recombination of hydrocarbon ions, J. Phys. Conf. Ser. 4 (2005) 191–197. https://doi.org/10.1088/1742-6596/4/1/027.
[80] A. Ehlerding, F. Hellberg, R. Thomas, S. Kalhori, A.A. Viggiano, S.T. Arnold, M. Larsson, M. af Ugglas, Dissociative recombination of C2H+ and C2H4+: Absolute cross sections and product branching ratios, Phys. Chem. Chem. Phys. 6 (2004) 949. https://doi.org/10.1039/b314882c.
[81] J. Perrin, O. Leroy, M.C. Bordage, Cross-Sections, Rate Constants and Transport Coefficients in Silane Plasma Chemistry, Contrib. to Plasma Phys. 36 (1996) 3–49. https://doi.org/10.1002/ctpp.2150360102.
[82] A.P. Hickman, Approximate scaling formula for ion–ion mutual neutralization rates, J. Chem. Phys. 70 (1979) 4872–4878. https://doi.org/10.1063/1.437364.
[83] J.S. Knight, C.G. Freeman, M.J. McEwan, V.G. Anicich, W.T. Huntress, A flow tube study of ion-molecule reactions of acetylene, J. Phys. Chem. 91 (1987) 3898–3902. https://doi.org/10.1021/j100298a033.
[84] I. Szabo, P.J. Derrick, Consecutive ion—molecule reactions in acetylene investigated by charge exchange mass spectrometry, Int. J. Mass Spectrom. Ion Phys. 7 (1971) 55–69. https://doi.org/10.1016/0020-7381(71)85031-3.

[85] G.A.W. Derwish, A. Galli, A.G. Guidoni, G.G. Volpi, Ion-Molecule Reactions in Acetylene, J. Am. Chem. Soc. 87 (1965) 1159–1168. https://doi.org/10.1021/ja01084a001.

[86] S. Wexler, R. Marshall, Consecutive Ion-Molecule Reactions in Ethylene, J. Am. Chem. Soc. 86 (1964) 781–787. https://doi.org/10.1021/ja01059a007.

[87] M.R.C. McDowell, J.P. Coleman, E.W. McDaniel, Introduction to the Theory of Ion-Atom Collisions, Am. J. Phys. 39 (1971) 237–238. https://doi.org/10.1119/1.1986112.

[88] D. McElroy, C. Walsh, A.J. Markwick, M.A. Cordiner, K. Smith, T.J. Millar, The UMIST database for astrochemistry 2012, 1204 (2012) 1197–1204. https://doi.org/10.1051/0004-6361/201220465.

[89] M. Tsuji, H. Kouno, K. Matsumura, T. Funatsu, Y. Nishimura, H. Obase, H. Kugishima, K. Yoshida, Dissociative charge-transfer reactions of Ar + with simple aliphatic hydrocarbons at thermal energy, J. Chem. Phys. 98 (1993) 2011–2022. https://doi.org/10.1063/1.464234.

[90] A.H. Laufer, A. Fahr, Reactions and kinetics of unsaturated C2 hydrocarbon radicals, Chem. Rev. 104 (2004) 2813–2832. https://doi.org/10.1021/cr030039x.

[91] William E. Wallace, NIST Chemistry webBook, NIST Standard Reference Database Number 69, National Institute of Standards and Technology, Gaithersburg MD, 2020. https://doi.org/https://doi.org/10.18434/T4D303.

[92] GAPHYOR Database Database on properties of atoms, molecules and neutral or ionized gases, including chemical reactions, (n.d.). http://gaphyor.lpgp.u-psud.fr/gaphyor/index.html.

[93] F.J. Gordillo-Vázquez, J.M. Albella, Influence of the pressure and power on the non-equilibrium plasma chemistry of C2, C2H, C2H2, CH3 and CH4 affecting the synthesis of nanodiamond thin films from C2H2(1%)/H2/Ar-rich plasmas, Plasma Sources Sci. Technol. 13 (2004) 50. https://doi.org/10.1088/0963-0252/13/1/007.

[94] C. Deschenaux, A. Affolter, D. Magni, C. Hollenstein, P. Fayet, Investigations of CH4 , C2H2 and C2H4 dusty RF

plasmas by means of FTIR absorption spectroscopy and mass spectrometry, J. Phys. D. Appl. Phys. 32 (1999) 1876–1886. https://doi.org/10.1088/0022-3727/32/15/316.
[95] M.M. Turner, Uncertainty and error in complex plasma chemistry models, Plasma Sources Sci. Technol. 24 (2015) 035027. https://doi.org/10.1088/0963-0252/24/3/035027.
[96] M.M. Turner, Uncertainty and sensitivity analysis in complex plasma chemistry models, Plasma Sources Sci. Technol. 25 (2016). https://doi.org/10.1088/0963-0252/25/1/015003.
[97] R. Lehmann, An Algorithm for the Determination of All Significant Pathways in Chemical Reaction Systems, J. Atmos. Chem. 47 (2004) 45–78. https://doi.org/10.1023/B:JOCH.0000012284.28801.b1.
[98] ☆ A H Markosyan, A. Luque, F.J. Gordillo-Vázquez, U. Ebert, PumpKin: A tool to find principal pathways in plasma chemical models, Comput. Phys. Commun. 185 (2014) 2697–2702. https://doi.org/10.1016/j.cpc.2014.05.019.
[99] K. Peerenboom, A. Parente, T. Kozák, A. Bogaerts, G. Degrez, Dimension reduction of non-equilibrium plasma kinetic models using principal component analysis, Plasma Sources Sci. Technol. 24 (2015) 025004. https://doi.org/10.1088/0963-0252/24/2/025004.
[100] O. May, J. Fedor, B.C. Ibănescu, M. Allan, Absolute cross sections for dissociative electron attachment to acetylene and diacetylene, Phys. Rev. A - At. Mol. Opt. Phys. 77 (2008) 3–6. https://doi.org/10.1103/PhysRevA.77.040701.
[101] Z. Amitay, D. Zajfman, P. Forck, U. Hechtfischer, B. Seidel, M. Grieser, D. Habs, R. Repnow, D. Schwalm, A. Wolf, Dissociative recombination of CH+: Cross section and final states, Phys. Rev. A. 54 (1996) 4032–4050. https://doi.org/10.1103/PhysRevA.54.4032.
[102] D. Thirumalai, K. Onda, D.G.D. Truhlar, Elastic scattering and rotational excitation of a polyatomic molecule by electron impact: Acetylene, J. Chem. Phys. 526 (1981). https://doi.org/10.1063/1.440804.
[103] K. Toshio, I. Kazumichi, T. Noriaki, H. Kenji, Cross Sections of Charge Transfer by Slow Singly-Charged Carbon Ions, 7

(2006) 241–244.

[104] E. Neyts, P. Brault, Molecular Dynamics Simulations for Plasma-Surface Interactions, Plasma Process. Polym. 14 (2017). https://doi.org/10.1002/ppap.201600145.

[105] W. Möller, Plasma and surface modeling of the deposition of hydrogenated carbon films from low-pressure methane plasmas, Appl. Phys. A Solids Surfaces. 56 (1993) 527–546. https://doi.org/10.1007/BF00331402.

[106] E. Neyts, Mathematical Simulation of the Deposition of Diamond-like carbon (DLC) Films, Antwerpen University, 2006.

[107] D. Herrebout, A. Bogaerts, M. Yan, R. Gijbels, W. Goedheer, A. Vanhulsel, Modeling of a capacitively coupled radio-frequency methane plasma: Comparison between a one-dimensional and a two-dimensional fluid model, J. Appl. Phys. 92 (2002) 2290–2295. https://doi.org/10.1063/1.1500789.

[108] J.W. Bradley, Study of the plasma pre-sheath in magnetron discharges dominated by Bohm diffusion of electrons, Plasma Sources Sci. Technol. 7 (1998) 572–580. https://doi.org/10.1088/0963-0252/7/4/014.

[109] V. Ivanov, O. Proshina, T. Rakhimova, A. Rakhimov, D. Herrebout, A. Bogaerts, Comparison of a one-dimensional particle-in-cell-Monte Carlo model and a one-dimensional fluid model for a CH 4/H 2 capacitively coupled radio frequency discharge, J. Appl. Phys. 91 (2002) 6296–6302. https://doi.org/10.1063/1.1461895.

[110] P.W. May, N.L. Allan, M.N.R. Ashfold, A. Mesbahi, F. Silva, S. Farhat, A. Bogaerts, M. Eckert, M. Mao, C.J. Rennick, J. Ma, J.J. Gracio, Q.H. Fan, J.C. Madaleno, G. Lombardi, K. Hassouni, G.D. Stancu, J.E. Butler, Y.A. Mankelevich, A. Cheesman, Understanding the chemical vapor deposition of diamond: recent progress, J. Phys. Condens. Matter. 21 (2009). https://doi.org/10.1088/0953-8984/21/36/364201.

[111] D.A. Ariskin, I. V. Schweigert, A.L. Alexandrov, A. Bogaerts, F.M. Peeters, Modeling of chemical processes in the low pressure capacitive radio frequency discharges in a mixture of Ar/C2H2, J. Appl. Phys. 105 (2009) 1–11.

https://doi.org/10.1063/1.3095760.

[112] E. Neyts, M. Eckert, M. Mao, A. Bogaerts, Numerical simulation of hydrocarbon plasmas for nanoparticle formation and the growth of nanostructured thin films, Plasma Phys. Control. Fusion. 51 (2009) 124034. https://doi.org/10.1088/0741-3335/51/12/124034.

[113] M. Mao, A. Bogaerts, Investigating the plasma chemistry for the synthesis of carbon nanotubes/nanofibres in an inductively coupled plasma enhanced CVD system: the effect of different gas mixtures, J. Phys. D. Appl. Phys. 43 (2010) 205201. https://doi.org/10.1088/0022-3727/43/20/205201.

[114] J.R. Doyle, Chemical kinetics in low pressure acetylene radio frequency glow discharges, J. Appl. Phys. 82 (1997) 4763. https://doi.org/10.1063/1.366333.

[115] P.H. Mayrhofer, Quantum Chemistry guided Materials Design Concepts for improved Strength , Ductility , and Stability of Thin Films PVD for Tools , Components & …, (1899).

[116] Y. Miyagawa, H. Nakadate, M. Tanaka, M. Ikeyama, S. Nakao, S. Miyagawa, PIC simulation of N2 and C2H2 plasma behavior around plural objects, Surf. Coatings Technol. 201 (2007) 8414–8419. https://doi.org/10.1016/j.surfcoat.2006.03.067.

[117] S. Mathioudaki, C.R. Vandenabeele, R. Tonneau, A. Pflug, J. Tennyson, S. Lucas, Plasma polymerization of cyclopropylamine in a low-pressure cylindrical magnetron reactor: A PIC-MC study of the roles of ions and radicals, J. Vac. Sci. Technol. A. 38 (2020) 033003. https://doi.org/10.1116/1.5142913.

[118] A.L. Alexandrov, Two-dimensional PIC-MCC simulations of capacitively coupled radio-frequency discharge in methane, (2004). https://arxiv.org/pdf/physics/0406047.pdf (accessed March 20, 2018).

[119] Y. Hirata, J. Choi, Deposition of a-C:H films on inner surface of high-aspect-ratio microchannel, J. Appl. Phys. 120 (2016) 065305. https://doi.org/10.1063/1.4960694.

[120] A. Pflug, M. Siemers, T. Melzig, L. Schäfer, G. Bräuer, Simulation of linear magnetron discharges in 2D and 3D, Surf. Coatings Technol. 260 (2014) 411–416.

https://doi.org/10.1016/j.surfcoat.2014.09.042.
[121] D. Tskhakaya, K. Matyash, R. Schneider, F. Taccogna, The Particle-In-Cell method, Contrib. to Plasma Phys. (2007). https://doi.org/10.1002/ctpp.200710072.
[122] G.A. Bird, Molecular Gas Dynamics and the Direct Simulation of Gas Flows, 1994. http://ukcatalogue.oup.com/product/9780198561958.do.
[123] W.H. Press, B.P. Flannery, S.A. Teukolsky, W.T. Vetterling, Successive Overrelaxation (SOR)., in: Numer. Recipes FORTRAN Art Sci. Comput. 2nd Ed., Cambridge, Cambridge, England, 1992: pp. 866–869.
[124] J.P. Boris, Relativistic Plasma Simulation – Optimization of a Hybride Code, in: Proc. 4th Conf. Numer. Simul. Plasmas, 1970: pp. 3–67.
[125] A.B. Langdon, Effects of the spatial grid in simulation plasmas, J. Comput. Phys. (1970). https://doi.org/10.1016/0021-9991(70)90024-0.
[126] D. Thiry, S. Konstantinidis, J. Cornil, R. Snyders, Plasma diagnostics for the low-pressure plasma polymerization process: A critical review, Thin Solid Films. 606 (2016) 19–44. https://doi.org/10.1016/j.tsf.2016.02.058.
[127] I.H. Hutchinson, Principles of Plasma Diagnostics, Cambridge University Press, 2002. https://doi.org/10.1017/CBO9780511613630.
[128] L.L. Kazmerski, Analysis and characterization of thin films: A tutorial, Sol. Cells. 24 (1988) 387–418. https://doi.org/10.1016/0379-6787(88)90091-9.
[129] T. Romain, Probing the physics of magnetron sputtering for thin-film deposition by Virtual Coater :, (2021).
[130] T. Richard, I. Furno, A. Sublet, M. Taborelli, Influence of ion-induced secondary electron emission parameters in PICMC plasma simulations with experimental validation in DC cylindrical diode and magnetron discharges, Plasma Sources Sci. Technol. 29 (2020). https://doi.org/10.1088/1361-6595/aba986.
[131] R.J. D'Arcy, Dielectric impurities and surface instability in langmuir probe plasma measurements, J. Phys. D. Appl. Phys.

7 (1974) 1391–1401. https://doi.org/10.1088/0022-3727/7/10/312.
[132] A. Belkind, F. Jansen, Anode effects in magnetron sputtering, Surf. Coatings Technol. 99 (1998) 52–59. https://doi.org/10.1016/S0257-8972(97)00409-X.
[133] T. Melzig, M. Siemers, A. Pflug, R. Rank, 3D PIC-MC simulation of anode effects in dual magnetron discharges, Surf. Coatings Technol. 241 (2014) 30–32. https://doi.org/10.1016/j.surfcoat.2013.10.024.
[134] S.Z. Wu, Dependence of plasma characteristics on dc magnetron sputter parameters, J. Appl. Phys. 98 (2005). https://doi.org/10.1063/1.2112177.
[135] L.L. Alves, A. Bogaerts, V. Guerra, M.M. Turner, Foundations of modelling of nonequilibrium low-temperature plasmas, IOP Publishing, 2018. https://doi.org/10.1088/1361-6595/aaa86d.
[136] P. Sigurjonsson, J.T. Gudmundsson, Plasma parameters in a planar dc magnetron sputtering discharge of argon and krypton, J. Phys. Conf. Ser. 100 (2008) 062018. https://doi.org/10.1088/1742-6596/100/6/062018.
[137] N. Brenning, J.T. Gudmundsson, D. Lundin, T. Minea, M.A. Raadu, U. Helmersson, The role of Ohmic heating in dc magnetron sputtering, Plasma Sources Sci. Technol. 25 (2016) 65024. https://doi.org/10.1088/0963-0252/25/6/065024.
[138] F. Guimarães, J. Almeida, J. Bretagne, Modeling of the energy deposition mechanisms in an argon magnetron planar discharge, J. Vac. Sci. Technol. A Vacuum, Surfaces, Film. 9 (1991) 133–140. https://doi.org/10.1116/1.577113.
[139] A. Von Keudell, W. Möller, R. Hytry, Deposition of dense C:H films at elevated substrate temperature, Diam. Relat. Mater. 2 (1993) 251–254. https://doi.org/10.1016/0925-9635(93)90063-8.
[140] I. Solomon, M. Bhatnagar, K. Shukla, B. Sarma, M. Ranjan, A. Sarma, Correlation of structural and optical properties of PVD grown amorphous carbon thin films, Diam. Relat. Mater. 75 (2017) 69–77. https://doi.org/10.1016/j.diamond.2017.01.015.
[141] A. Grill, V. Patel, B.S. Meyerson, Optical and tribological properties of heat-treated diamond-like carbon, J. Mater. Res. 5

(1990) 2531–2537. https://doi.org/10.1557/JMR.1990.2531.
[142] D. Thiry, S. Konstantinidis, J. Cornil, R. Snyders, Plasma diagnostics for the low-pressure plasma polymerization process: A critical review, Thin Solid Films. 606 (2016) 19–44. https://doi.org/10.1016/j.tsf.2016.02.058.
[143] M. Panjan, R. Franz, A. Anders, Asymmetric particle fluxes from drifting ionization zones in sputtering magnetrons, Plasma Sources Sci. Technol. 23 (2014). https://doi.org/10.1088/0963-0252/23/2/025007.
[144] A. Pflug, M. Siemers, C. Schwanke, B. Szyszka, Simulation von Plasma-Beschichtungsprozessen, Vak. Forsch. Und Prax. 22 (2010) 31–34. https://doi.org/10.1002/vipr.201000419.
[145] C. Schwanke, A. Pflug, M. Siemers, B. Szyszka, Parallel Particle-in-Cell Monte-Carlo Algorithm for Simulation of Gas Discharges under PVM and MPI, in: Lect. Notes Comput. Sci., Springer, Berlin, Heidelberg, 2012: pp. 213–219. https://doi.org/10.1007/978-3-642-28151-8_21.
[146] A. Pflug, PICMC documentation, (n.d.). https://simulation.ist.fraunhofer.de.